



University
of Glasgow

Giovannini, Daniel (2014) *Orbital angular momentum entanglement in high dimensions*. PhD thesis.

<http://theses.gla.ac.uk/5720/>

Copyright and moral rights for this thesis are retained by the author

A copy can be downloaded for personal non-commercial research or study, without prior permission or charge

This thesis cannot be reproduced or quoted extensively from without first obtaining permission in writing from the Author

The content must not be changed in any way or sold commercially in any format or medium without the formal permission of the Author

When referring to this work, full bibliographic details including the author, title, awarding institution and date of the thesis must be given

Orbital angular momentum
entanglement in
high dimensions

Daniel Giovannini

SUBMITTED IN FULFILMENT OF
THE REQUIREMENTS FOR THE DEGREE OF
DOCTOR OF PHILOSOPHY

School of Physics and Astronomy
College of Science and Engineering
University of Glasgow

November 2014

Abstract

Orbital angular momentum (OAM) is one of the most recently discovered properties of light, and it is only in the past decade its quantum properties have been the subject of experimental investigations and have found applications. Unlike polarization, which is only bidimensional, orbital angular momentum provides, with relative ease, unprecedented access to a theoretically unbounded discrete state space.

The process of spontaneous parametric down-conversion has long been used as a source of two-photon states that can be entangled in several degrees of freedom, including OAM. In this thesis, the properties of the natural OAM spectrum associated with the entangled states produced by parametric down-conversion were investigated. Chapters 2 and 3 describe the production and detection of tunable high-dimensional OAM entanglement in a down-conversion system. By tuning the phase-matching conditions and improving the detection stage, a substantial increase in the half-width of the OAM correlation spectrum was observed.

The conjugate variable of OAM, angular position, was also considered when examining high-dimensional states entangled in OAM. In order to efficiently determine their dimension, high-dimensional entangled states were probed by implementing a technique based on phase masks composed of multiple angular sectors, as opposed to narrow single-sector analysers. Presented in chapter 4, this technique allows the measurements of tight angular correlations while maintaining high optical throughput.

The states so produced were then used for a number of applications centred around the concept of mutually unbiased bases. One can define sets of mutually

unbiased bases for arbitrary subspaces of the OAM state space. Two bases are mutually unbiased if the measurement of a state in one basis provides no information about the state as described in the other basis. Complete measurements in mutually unbiased bases of high-dimensional OAM spaces are presented in chapter 5. Measurements in sets of mutually unbiased bases are integral to quantum science and can be used in a variety of protocols that fully exploit the large size of the OAM state space; we describe their use in efficient quantum state tomography, quantum key distribution and entanglement detection.

Caution is however necessary when dealing with state spaces embedded in higher-dimensional spaces, such as that provided by OAM. Experimental tests of Bell-type inequalities allow us to rule out local hidden variable theories in the description of quantum correlations. Correlations inconsistent with the states observed, or even with quantum mechanics, known as super-quantum correlations, have however been recorded previously in experiments that fail to comply with the fair-sampling conditions. Chapter 6 describes an experiment that uses a particular choice of transverse spatial modes for which super-quantum correlations persist even if the detection is made perfectly efficient.

The sets of modes carrying OAM allow a complete description of the transverse field. The ability to control and combine additional degrees of freedom provides the possibility for richer varieties of entanglement and can make quantum protocols more powerful and versatile. One such property of light, associated with transverse modes possessing radial nodes in the field distribution, can be accessed within the same type of experimental apparatus used for OAM. In chapter 7, the radial degree of freedom is explored, together with OAM, in the context of Hong-Ou-Mandel interference.

Contents

List of tables	IX
List of figures	XII
Acknowledgements	XIII
Author's declaration	XV
Publications	XVII
1 Introduction	1
1.1 The quantum nature of light	1
1.2 Quantum entanglement	3
1.3 The angular momentum of light	5
1.3.1 Spin and orbital angular momentum	6
1.3.2 Measuring spin and orbital angular momentum	8
1.3.3 The paraxial approximation	10
1.3.4 Duality relation between orbital angular momentum and angular position	13
1.4 The angular momentum of light as a quantum resource	15
2 Production and measurement of OAM-entangled two-photon states	19
2.1 Spontaneous parametric down-conversion	19
2.1.1 Phase-matching	20
2.1.2 The Klyshko advanced wave model	25
2.2 Entanglement of orbital angular momentum	28

2.3	Experimental methods	32
2.3.1	Collinear parametric down-conversion with BBO crystals .	32
2.3.2	Phase-flattening measurements with spatial light modulators	34
2.3.3	Coincidence detection	37
3	Generation of high-dimensional OAM-entangled states	39
3.1	Spiral bandwidth	41
3.1.1	Analytical treatment of spiral bandwidth	44
3.1.2	Geometrical argument	46
3.1.3	Optimization of orbital angular momentum bandwidths .	50
3.1.4	Optical étendue and dimensionality	52
3.2	Increasing the spiral bandwidth in parametric down-conversion .	53
3.2.1	Experimental results	54
3.2.2	Angular two-photon interference and entanglement mea- sures	57
3.3	Pump shaping	59
3.3.1	SPDC with a phase-flipped Gaussian mode as pump	61
3.3.2	Experiment and results	63
4	Efficient determination of the dimensionality of bipartite OAM entan- glement	67
4.1	Angular slits and phase masks	69
4.2	Shannon dimensionality	70
4.3	Experimental determination of the effective dimensionality of bi- partite OAM entanglement	72
4.3.1	Experimental set-up	72
4.3.2	Experimental results and discussion	75
5	Mutually unbiased bases in high-dimensional subspaces of OAM: mea- surement and applications	79
5.1	Measuring high-dimensional orbital angular momentum states in MUB	81
5.1.1	Mutually unbiased bases	81
5.1.2	Mutually unbiased bases for OAM subspaces	84

5.1.3	Experimental methods	85
5.2	Efficient high-dimensional quantum state reconstruction with mutually unbiased bases	89
5.2.1	Mutually unbiased bases in quantum state tomography	89
5.2.2	State reconstruction methods	92
5.2.3	Results	94
5.3	Quantum key distribution with high-dimensional OAM mutually unbiased bases	98
5.3.1	Average error rate	100
5.3.2	Secret key rate	102
5.3.3	Experiment and result	104
5.4	Entanglement detection with mutually unbiased bases	106
6	Fair sampling in high-dimensional state spaces	109
6.1	Fair sampling in Bell-type experiments	111
6.2	Synthesizing super-quantum correlations with spatial modes	113
6.3	Sampling high-dimensional state spaces	117
7	Extending the Hilbert space of transverse modes using the radial degree of freedom	123
7.1	The radial degree of freedom	124
7.2	Interference of probability amplitudes in the Hong-Ou-Mandel effect	126
7.3	Exploring the quantum nature of the radial degree of freedom	133
8	Conclusions	141
A	Mutually unbiased vectors	145
A.1	Coefficients for $d = 2$	145
A.2	Coefficients for $d = 3$	145
A.3	Coefficients for $d = 4$	146
A.4	Coefficients for $d = 5$	147
B	List of abbreviations	149

List of Tables

3.1	Phase-flipped Gaussian mode decomposition	62
5.1	Results of tomographic reconstructions with mutually unbiased measurements	97
7.1	Expansion coefficients for the transverse modes used in radial Hong-Ou-Mandel interference	137

List of Figures

1.1 Spin and orbital angular momentum of light	5
1.2 Propagation of the Poynting vector associated with a Laguerre-Gaussian mode	8
1.3 Transfer of spin and orbital angular momentum	9
2.1 Parametric down-conversion configuration	21
2.2 Pump, signal and idler wave vectors in SPDC	22
2.3 Collinear and noncollinear phase matching SPDC intensity distributions.	26
2.4 Klyshko model of down-conversion	27
2.5 Experimental parametric down-conversion set-up	33
2.6 Computer generated-holograms	35
3.1 Schmidt number and full width at half maximum of an OAM spectrum, and Schmidt number as a function of crystal length and pump beam size	47
3.2 Spiral bandwidth and angular position correlations	54
3.3 Concurrence measurements for different phase-matching conditions	58
3.4 OAM and angular position correlations for a phase-flipped Gaussian pump	64
4.1 Typical best Gaussian fits of coincidence probability distributions for multi-sector phase masks	73
4.2 Detected spiral bandwidths with forked holograms	74

4.3	Detection capabilities of multi-sector phase masks and experimental results	75
5.1	State spaces of a bipartite system	83
5.2	Mutually unbiased modes for a two-dimensional OAM subspace .	84
5.3	Mutually unbiased modes for a three-dimensional OAM subspace	87
5.4	Mutually unbiased modes for a five-dimensional OAM subspace .	88
5.5	Overcomplete and complete quantum state tomography with MUB	89
5.6	Single-photon measurements in OAM subspaces of entangled two-photon states	93
5.7	Results of tomographic reconstructions using complete sets of single-photon mutually unbiased bases measurements	95
5.9	Quantum key distribution parameters for full sets of MUB	101
5.10	Mutual correlation for entanglement detection with MUB	105
6.1	Two- and four-channel Bell-type experiments	110
6.2	Fourier synthesis of a square wave	114
6.3	Coincidence curves for an OAM Bell-type experiment with orientation-dependent post-selection and recorded values of Bell parameter S as a function of the relative analyser orientation	116
6.4	Theoretical coincidence probabilities and Bell parameters for Bell-type experiments with polarization and OAM sector states, without renormalization	118
7.2	Hong-Ou-Mandel coincidence dips for different placements of narrow-band filters	130
7.3	Hong-Ou-Mandel dips for filters with different bandwidths placed before and after the beam splitter	131
7.4	Experimental set-up for the observation of Hong-Ou-Mandel interference in the radial degree of freedom	134
7.5	Experimental data of the Hong-Ou-Mandel interference in the radial degree of freedom	136

Acknowledgements

This thesis would not have been possible if not for the passion and enthusiasm of my supervisor, Miles, who has provided guidance and support throughout my entire PhD. I would also like to thank Sonja, who has been a valuable second supervisor.

My gratitude also goes to EPSRC, for providing the funds that supported my PhD.

I would like to thank Jacqui, for her irreplaceable help on both experimental and theoretical matters. Also, thank you Filippo, Andrew, Melanie, Angela and all who I have had the pleasure to work with at different times.

Thanks to all current and past members of the Optics group at the University of Glasgow for being excellent human beings first, for the variety of their expertise and the willingness with which they share it, and for the copious amounts of cake, countless pints, many barbecues and the occasional wacky cycling/unicycling/climbing adventure that we have enjoyed together.

I would like to thank Robert Boyd for welcoming me to his research group at the University of Ottawa during my 2013 research exchange, which was supported by the College of Science and Engineering at the University of Glasgow.

Thank you, Valerio and David, for the 24/7 transnational banter and for being constant reminders of what it is actually like to be good physicists at our age.

My thanks also go to the Quantum Optics group at Sapienza University of Rome: without your lectures and mentoring I may have never become interested in experimental physics and quantum optics during my undergraduate studies.

Author's declaration

I hereby declare that this thesis is the result of my own work, except where explicit reference is made to the work of others, and has not been presented in any previous application for a degree at this or any other institution.

Daniel Giovannini

Publications

This thesis is the culmination of the work carried out during my PhD in the Optics group at the University of Glasgow, under the supervision of Prof. Miles Padgett and Dr. Sonja Franke-Arnold. A list of the peer-reviewed papers co-authored in the three and a half years of the PhD programme is given below.

1. F. M. Miatto, D. Giovannini, J. Romero, S. Franke-Arnold, S. M. Barnett and M. J. Padgett, “Bounds and optimisation of orbital angular momentum bandwidths within parametric down-conversion systems”, *European Physical Journal D* **66**(7), 178 (2012)
2. D. Giovannini, F. M. Miatto, J. Romero, S. M. Barnett, J. P. Woerdman and M. J. Padgett, “Determining the dimensionality of bipartite orbital-angular-momentum entanglement using multi-sector phase masks”, *New Journal of Physics* **14**(7), 073046 (2012)
3. J. Romero, D. Giovannini, S. Franke-Arnold, S. M. Barnett and M. J. Padgett, “Increasing the dimension in high-dimensional two-photon orbital angular momentum entanglement”, *Physical Review A* **86**(1), 012334 (2012)
4. J. Romero, D. Giovannini, M. G. McLaren, E. Galvez, A. Forbes and M. J. Padgett, “Orbital angular momentum correlations with a phase-flipped Gaussian mode as pump beam”, *Journal of Optics* **14**(8), 085401 (2012)
5. D. Giovannini, J. Romero, J. Leach, A. Dudley, A. Forbes and M. J. Padgett, “Characterization of high-dimensional entangled systems via mutually unbiased measurements”, *Physical Review Letters* **110**(14), 143601 (2013)

6. J. Romero, D. Giovannini, S. M. Barnett and M. J. Padgett, “Tailored two-photon correlation and fair-sampling: a cautionary tale”, *New Journal of Physics* **15**(8), 083047 (2013)
7. M. Mafu, A. Dudley, S. Goyal, D. Giovannini, M. McLaren, M. J. Padgett, T. Konrad, F. Petruccione, N. Lütkenhaus and A. Forbes, “Higher-dimensional orbital angular momentum based quantum key distribution with mutually unbiased bases”, *Physical Review A* **88**(3), 032305 (2013)
8. E. Karimi, D. Giovannini, E. Bolduc, N. Bent, F. M. Miatto, M. J. Padgett and R. W. Boyd, “Exploring the quantum nature of the radial degree of freedom of a photon via Hong-Ou-Mandel interference”, *Physical Review A* **89**, 013829 (2014)
9. D. Giovannini, J. Romero and M. Padgett, “Interference of probability amplitudes: a simple demonstration within the Hong-Ou-Mandel experiment”, *Journal of Optics* **16**(3), 032002 (2014)

“Quantum information [...] is fragile and private, more like the information in a dream. Many people can read a book and get the same message, but trying to tell people about your dream changes your memory of it, so that eventually you forget the dream and remember only what you said about it.”

— Charles H. Bennett, *Publicity, Privacy, and Permanence of Information*

“[W]ith each change, the old machines were forgotten and new ones took their place. Very slowly, over thousands of years, the ideal of the perfect machine was approached – that ideal which had once been a dream, then a distant prospect, and at last reality.”

— Arthur C. Clarke, *The City and the Stars*

CHAPTER 1

Introduction

1.1 The quantum nature of light

Since its outset, quantum mechanics has been intimately intertwined with the properties of electromagnetic radiation. Quantum theory originated in the early 20th century with Max Planck's attempts to treat and describe black-body radiation [210]. In order to explain the spectral distribution of energy radiated by a thermal source, Planck postulated that energy is exchanged in multiples of the fundamental constant \hbar , multiplied by the angular frequency ω of the radiation that mediates the exchange. The concept of *photon* was thus introduced, although the term itself¹ was coined only later, in 1926, by Gilbert Lewis [164]. The shift from Planck's original definition of a *quantum of light* as the smallest discrete wave packet to the definition of the photon as a particle-like entity, and back, is at the heart of quantum mechanics. While the concepts of particle and wave are borrowed from classical mechanics, the theoretical and experimental advances that brought about the paradigm shift of particle-wave duality highlight the intrinsic complementarity of these two ideas in the quantum world. Either of the two manifestations of the photon can be observed, based on the formalism and measurement device employed [48]. This duality is one of the facets of the complementarity principle, one

¹Arthur Compton is also sometimes credited with introducing the term in 1923 [153].

of the foundational notions of quantum mechanics, at least in the traditional Copenhagen interpretation.

Farther still from the ideas of classical physics is the introduction of probability amplitudes in the description of wave packets. The use of probabilities to describe the relationship between the interpretation of physical phenomena and the manifestations of their inherent reality rendered quantum mechanics as a whole a fundamentally statistical theory, and whose physical significance is still debated [219]. However, it also finally allowed the descriptions of effects such as single-particle interference – effects often demonstrated, since the early days of quantum mechanics, by passing non-overlapping pulses of attenuated light first, and later on individual photons, through a double slit or a Mach-Zender interferometer.

Over the decades, light has therefore been instrumental in the experimental studies that spurred the development of quantum theory, as well as the further countless experimental tests of the very same theories. As a resource in quantum science, light possesses several drawbacks: the interactions of photons with most physical systems is negligible, and the efficient production of single photons (though probabilistic) remains challenging. Since the inception of the laser in the 1960s, however, many desirable properties of light have also emerged or have become more easily accessible. In the theory of electromagnetic radiation in an optical cavity, fields can only be excited in discrete spatial modes; calculations and results obtained in this simplified framework can readily be extended to more general unconfined systems that include laser cavities, linear and nonlinear optical elements [170]. Developments in nonlinear and quantum optics, and the introduction in experimental practice over the past half century of technological advances, have made many photonic quantum experiment possible. This, as well as the convenience and high degree of coherence and monochromaticity of laser sources, have provided full control of the vast range of quantum properties of light — some of which, like orbital angular momentum, have started being explored only as recently as twenty years ago [9].

1.2 Quantum entanglement

Entanglement is one of the defining features of quantum mechanics with no classical equivalent. The concept of entanglement, which represents a departure from pre-existing notions of local relativistic causality and counterfactual realism in classical mechanics, was made necessary by the impossibility to reproduce some predictions of quantum mechanics by means of local theories. In their seminal 1935 paper, Albert Einstein, Boris Podolsky and Nathan Rosen (EPR) presented a thought experiment whose goal was to point out the apparent incompleteness of quantum mechanics in the then current formulation [95]. EPR described two subsystems which have been made to interact in such a way that their properties (such as position and momentum) remain correlated even after the subsystems have been spatially separated. The predictions for an EPR state cannot be reproduced by classical theories, like hidden-variable models; in the assumption that quantum mechanics were indeed a locally causal theory, Einstein, Podolsky and Rosen thus concluded that it must either fulfil local realism or be considered incomplete — in the sense that the state wavefunction is not a complete quantum-mechanical description of reality.

It was Erwin Schrödinger who, shortly afterwards, introduces the term *entanglement*, first in a letter to Einstein, then in an influential paper in which he tackled the apparent paradoxical nature of the EPR experiment and described the newly christened term “*the characteristic trait of quantum mechanics*” [240]. It wasn't until 1964 however that John Bell overturned one of the underlying assumptions of the EPR argument, the principle of locality [34, 35]. Bell proposed an inequality to test for the existence of local hidden variables, which would allow correlations between two system that would otherwise require Einstein's “spooky action at a distance”. The outcomes of appropriate sets of measurements define an upper bound for systems exhibiting locality. Nonlocal systems, which include quantum states, violate Bell's inequality and its alternative formulations, thus ruling out the possibility of hidden variable theories [105]. Beginning only in the early 1980s due to the challenging nature of experimental tests of local realism, this has been shown in a vast number of experiments, pioneered by Aspect, Grangier and Roger [17, 18, 16] and also aided by the reformulation of

Bell's bound in terms of the CHSH inequality² [76, 75].

The main possible experimental loopholes affecting Bell-type tests, which could mask the presence of hidden variables by introducing a statistical bias, have by now been closed for different types of quantum systems [273, 232, 114]. While a completely loophole-free Bell test has still to be performed, the current insight into the nature of entanglement seems to favour a nonlocal view [65]. It has also been shown how shared randomness (that is, the presence of classical communication between the parties prior to the measurement or established at the source), while introducing a form of nonlocal correlations, is not enough for the correlations to violate Bell-type inequalities [107].

It is important to highlight how nonlocality does not play any role in the definition of entanglement. Entanglement is indeed a nonlocal phenomenon, where separated systems share properties in a way that goes beyond classical mechanics. It can however be defined simply in terms of tensor products of states belonging to different Hilbert spaces. If the state of a physical system can be in one of many configurations, then according to the superposition principle the most general state is in fact expressed by a linear combination of all the different possibilities. As an example, let us take a pure state $|\psi\rangle$ in the Hilbert space \mathcal{H} associated with the composite system described by $\mathcal{H}_1 \otimes \mathcal{H}_2$. By taking as a basis for the system the tensor products of the d -dimensional basis vectors in the subsystem spaces \mathcal{H}_1 and \mathcal{H}_2 respectively, we may write

$$|\psi\rangle = \sum_{i,j=1}^d c_{ij} |i\rangle_1 \otimes |j\rangle_2. \quad (1.1)$$

The overall state $|\psi\rangle$ is said to be *entangled* if it cannot be expressed as a product state of states describing the two subsystems. Conversely, it is said to be separable if it can be expressed in the form

$$|\psi\rangle = |\zeta\rangle_1 \otimes |\theta\rangle_2 \quad (1.2)$$

in an appropriate basis. These ideas can of course be applied in theory to multi-

²CHSH stands for John Clauser, Michael Horne, Abner Shimony and Richard Holt, who described the inequality in 1969.

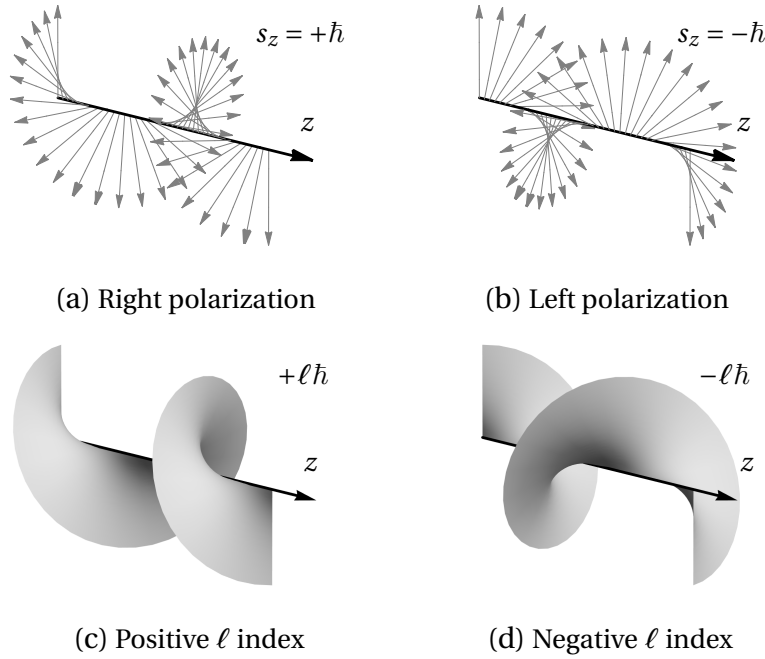


Figure 1.1: For circularly polarized light the electric and magnetic fields rotate around the beam axis during propagation. Light is said to be (a) right- or (b) left-circularly polarized based on the rotation direction of the fields, with spin in the propagation direction $s_z = \pm\hbar$ respectively. Orbital angular momentum (OAM) is associated instead with helical phase fronts, which lead respectively to values of OAM (c) $+\ell\hbar$ and (d) $-\ell\hbar$, with ℓ the winding number of the propagating mode.

partite, multidimensional systems. As the dimension of the state describing the composite system increases, however, analysing and characterizing entanglement becomes increasingly more complex.

Producing physical systems entangled in large state spaces still presents considerable experimental challenges. The use of high-dimensional systems, however, reveals stronger nonlocality [79, 165], and can be used to boost channel capacity and security in quantum communication systems [68, 92, 28].

1.3 The angular momentum of light

In this thesis, we will concern ourselves with the entanglement of single-photon states. The resilience of photonic entanglement [258, 110], the versatility of

quantum light and the wide range of physical properties experimentally accessible today make photonic entanglement an ideal testing ground for experiments exploring the foundations of quantum mechanics as well as developing novel applications and technologies.

In order to conduct experimental investigations of entanglement several properties of light have been used in the past. One can exploit frequency [193], position [131], and the temporal [84, 250] and spatial [172, 185, 198, 282, 81] features of optical fields to produce states entangled in any such properties. By combining the spaces provided by two or more of such degrees of freedom, it is also possible to introduce entanglement between different properties of light, known as *hyperentanglement* [154, 27], even within the same photon.

Each property of the photon gives access to a different state space with its own defining features. Polarization, for instance, provides a complex linear vector space which has been used in countless applications. Since the electric and magnetic fields \vec{E} and \vec{H} are mutually orthogonal, the direction of polarization is traditionally taken to correspond with that of the electric field in the transverse plane. This thus provides a convenient two-dimensional space that can act as the simplest model space to carry out quantum experiments, as polarization states can easily be manipulated and measured with combinations of conventional linear optical elements. The binary outcomes of such measurements have been used since the very early days of optical investigations of entanglement to perform Bell-type tests and implement quantum protocols [53].

1.3.1 Spin and orbital angular momentum

The angular momentum of light can be regarded as a property arising from the circulating flow of energy in the electric field [192, 119]. As is well understood, the macroscopic polarization is a feature emerging from the angular momentum of the photon. Spin is however only one component of the total angular momentum of light. Beyond polarization, the correspondence principle suggests that other properties of classical light should have a quantum analogue [50]. A richer and more promising property of light that can be used to realize

high-dimensional entanglement with as few as two entangled photons is orbital angular momentum (OAM). Unlike polarization, which as a physical quantity is limited to values between $-\hbar$ and \hbar , the orbital angular momentum of light offers a theoretically unbounded state space spanned by an infinite number of mutually orthogonal, distinguishable OAM eigenmodes characterized by the winding number ℓ of the beam helicity. The OAM content of a single photon is given by $\ell\hbar$, with the winding number ℓ describing the spiralling of the phase structure along the optical axis during propagation (fig. 1.1).

From both a classical and quantum standpoint, light possesses mechanical properties. John Henry Poynting showed that an electromagnetic wave has linear momentum and a well-defined energy flow in the transverse plane, the latter equal to $\vec{E} \times \vec{H}$ and with dimensions of a linear momentum per unit of volume [217, 201]. In a quantum framework, every photon associated with a plane-wave field carries a linear momentum equal to $\hbar\vec{k}$, with \hbar being the reduced Planck constant di Planck and \vec{k} the wave vector of the photon. The angular momentum density in the radial direction \vec{r} with respect to the direction of propagation is then given by $\epsilon_0\vec{r} \times (\vec{E} \times \vec{B})$ or, for quantum light, by $\vec{r} \times \hbar\vec{k}$. Poynting also showed that circularly polarized light has a flow of angular momentum equal to $\lambda w/2\pi$, where λ is the wavelength and w the average energy density, that is $w = n\hbar\omega$ (with n the number of photons per unit of volume). The angular momentum per photon is therefore $\pm\hbar$, depending on the sign of the circular polarization. It can be shown that the rotation of the Poynting vector in a beam carrying orbital angular momentum is proportional to the difference in the on-axis Gouy phase

$$\zeta(z) = \arctan(z/z_R), \quad (1.3)$$

from that at the beam waist $z = z_0$ [201], where z_R is the Rayleigh range

$$z_R = \pi w_0^2 / \lambda, \quad (1.4)$$

and w_0 is the $1/e^2$ beam size at $z = 0$ (fig. 1.2).

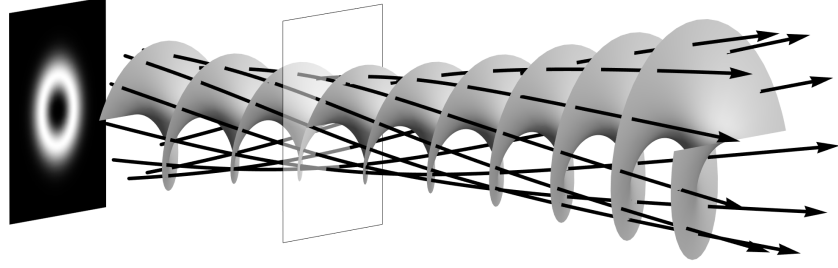


Figure 1.2: Propagation of the Poynting vector associated with a Laguerre-Gaussian mode with $\ell = 2$, $p = 0$. For a fixed position z along the propagation direction of the beam, the Poynting vector follows a spiralling path.

1.3.2 Measuring spin and orbital angular momentum

The motion of a revolving shaft was studied by Poynting in 1909 [218], when he used mechanical analogies to establish that, for circularly polarized light, the ratio of the optical energy to angular momentum corresponds to the angular frequency. He proposed a possible experiment where one may be able to detect the small torque exerted by circularly polarized light passing through a stack of quarter-wave plates, as its polarization is converted into linear.

The measurement of torque induced on a birefringent plate by the angular momentum of light was performed for the first time in 1936 by Beth [45], using a variant of the experiment suggested by Poynting that involved a tungsten bulb and an arrangement of quarter-wave plates. A small transverse component of linear momentum, such as that found in Hermite-Gaussian (HG) and Laguerre-Gaussian (LG) modes, can in fact introduce a second angular momentum components \vec{L} in the direction of propagation, in addition to spin \vec{S} :

$$S_i = \frac{1}{2\mu_0\omega} \sum_{j,k} \int E_j^* (-i\epsilon_{ijk}) E_k d\vec{r} \quad (1.5)$$

$$L_i = \frac{1}{2\mu_0\omega} \sum_j \int E_j^* (-i\vec{r} \times \nabla)_i E_j d\vec{r}, \quad (1.6)$$

with indices i, j, k taking values $\{x, y, z\}$ for each of the three components of vectors \vec{S} and \vec{L} [132, 80, 12]. The first component is called *spin angular momentum*, independent from the frame of reference, while the second, dependent on the

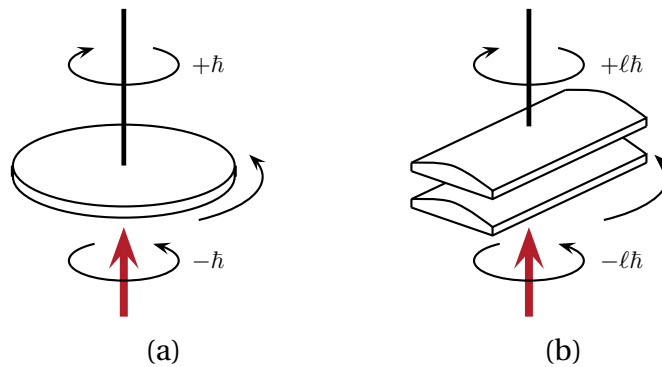


Figure 1.3: (a) A suspended birefringent half-wave plate undergoes a rotation when transforming right-handed circularly polarized light into left-handed polarized light. (b) A system of cylindrical lenses undergoes a rotation when converting a mode with angular momentum $-\ell\hbar$ per photon into one with $+\ell\hbar$ per photon.

choice of frame of reference, from an analogy with quantum mechanics is the *orbital angular momentum*.

The measurement of torque due to orbital angular momentum, presented by Allen and co-workers in 1992, is analogous to that of spin angular momentum [9]. A pair of astigmatic optical elements, such as cylindrical lenses, allow to produce classical light with precise values of orbital angular momentum. The torsion of the fibre sustaining the lenses can be predicted in terms of the intensity of the light and the orbital angular momentum ℓ .

The quantum state of a photon can be described by a multipole expansion of electromagnetic waves with a well-defined energy value of $\hbar\omega$, total angular momentum (made up of spin and orbital angular momentum components) and a fixed projection of the angular momentum along a chosen axis (for instance, the propagation direction z). Such decomposition is analogue to that of light, either classical or quantum, in terms of a set of plane waves. In general, the spin and orbital contributions cannot be examined separately; however, in the limit of small beam divergence, called paraxial approximation, it is possible to show that the two components can be measured and manipulated independently [261, 260].

1.3.3 The paraxial approximation

In the paraxial case, the spin and orbital components along the direction of propagation can for instance be measured by observing the variation of angular momentum in a medium that interacted with appropriate modes of the radiation field. Beth's experiment, in which a birefringent plate converts light with right-handed circular polarization into left-handed polarized light, can be interpreted as a measurement of the component of the spin angular momentum in the direction of the wave vector [45]. In the experiment, the amplitude and phase spatial distribution of the light was unchanged. An experiment like the one performed by Allen et al. [9], however, or one where a Hermite-Gaussian mode with zero orbital angular momentum is converted in the paraxial approximation into a Laguerre-Gaussian mode by means of a system of two astigmatic lenses [32], allows to measure the orbital angular momentum component along the direction of propagation (fig. 1.3).

In the paraxial approximation for the wave equation, in the case of unpolarized fields of the form $A(r, \phi, z) = u_0(r, z) e^{i\ell\phi}$, it is possible to show that the ratio between density of angular momentum j_z along the propagation direction and energy density w takes the form

$$\frac{j_z}{w} = \frac{\ell}{\omega}, \quad (1.7)$$

with angular frequency ω . The ratio between angular momentum and linear momentum can be shown to be equal to $\omega\ell/\omega k = \ell\lambda/2\pi$, which highlights how the field has orbital angular momentum $\ell\hbar$ per photon [9]. Such result can be extended to polarized light, even beyond the paraxial approximation. The ratio ℓ/ω is the equivalent, in the case of the orbital angular momentum component, of the known ratio between spin orbital angular momentum and energy for circularly polarized light, $\pm\hbar/\hbar\omega = \pm 1/\omega$ [45].

For the Laguerre-Gaussian mode used in the experiment by Allen et al., the azimuthal relation $\exp(i\ell\phi)$ implies therefore a ratio between orbital angular momentum and energy equal to ℓ/ω . Since the angular momentum along the propagation direction L_z is conserved, and since the polarization (and therefore

the S_z component of spin) remains unchanged, the system of lenses should undergo a torque due to the change in total momentum. It is then possible to measure separately in the two experiments mentioned L_z and S_z , with results that can be described in a classical framework.

The paraxial approximation appears to be the most convenient context in which the orbital angular momentum can be studied. In this approximation, the OAM of light provides a useful description of the degree of freedom associated with the transverse modes of photons, whose continuous nature defines a Hilbert space inherently infinite-dimensional. Some aspects of the paraxial approximation may be familiar, being the wave equation that emerges from such treatment formally analogous to the Schrödinger equation, where time t replaces the direction of propagation z . The term $u\nabla u^* - u^*\nabla u$ that appears after the application of the approximation to the Helmholtz equation resembles the expression of the probability current of a wavefunction u ; in the paraxial form, the field is treated as if it were an eigenstate of the angular momentum operator $L_z u = -i\hbar\partial u/\partial\phi = \ell\hbar u$. It should be underlined that u is not the wavefunction of a particle, but rather the classical distribution function of the amplitude and phase of the field. It is however possible to use the analogy between quantum mechanics and geometric optics to investigate the properties of the orbital angular momentum of light [261, 260]. In this formal scheme, the expectation value for the orbital angular momentum for paraxial light can be expressed in terms of contributions analogous to those of the angular momentum of an oscillator, plus contributions related to the astigmatism of the beam considered.

The modes of a laser are stationary electromagnetic waves, with properties defined by the geometry of the resonant cavity. Resonant optical cavities impose two main conditions to the fields produced. The first requires the phase to be periodic within the cavity, thus defining the longitudinal structure of the field; for instance, one has $n\lambda/2 = L$ in a cavity with length L , with n integer. The second imposes that the intensity of the electromagnetic field goes to zero away from the axis of the cavity, with the field being a solution of Maxwell's equations in the paraxial approximation. By studying a cross-section of a beam perpendicular to the direction of propagation it is possible to observe amplitude distributions called TEM (transverse electromagnetic modes, where the fields \vec{E}

and \vec{B} have no components along the direction of propagation) and identified by generic indices n , m and q for solutions of the Helmholtz equation in rectangular coordinated, or ℓ , p and q for cylindrical solutions. The last of the three indices is usually associated with the longitudinal modes oscillating in an optical cavity, and it will be omitted from now on.

Amongst the families of modes that are solutions of the Helmholtz equation for the description of light propagation in the paraxial approximation, some represent eigenstates of the quantum operator of orbital angular momentum along the propagation direction. Such modes, called Laguerre-Gaussian, are denoted by the azimuthal phase structure $\exp(i\ell\phi)$ that characterizes the presence of well-defined values of OAM per photon. Laguerre-Gaussian modes form a complete Hilbert basis, just like Hermite-Gaussian modes (solutions in cartesian coordinates of the wave equation) and hypergeometric-Gaussian modes [235, 145]. The LG set of modes is defined as:

$$u_{\ell p}(r, \phi, z) = \sqrt{\frac{2p!}{w(z)\pi(|\ell| + p)!}} \left(\frac{\sqrt{2}r}{w(z)}\right)^{|\ell|} \exp\left(-\frac{r^2}{w^2(z)}\right) L_p^{|\ell|}\left(\frac{2r^2}{w^2(z)}\right) \exp\left(-ik\frac{r^2 z}{2(z^2 + z_R^2)}\right) \exp(i\ell\phi) \exp[-i(|\ell| + 2p + 1)\zeta(z)] \quad (1.8)$$

expressed in polar coordinates r and ϕ , where ℓ is the azimuthal mode index (corresponding to the winding number) and p is the radial mode index (corresponding to the number of radial nodes in the field distribution). The beam waist as a function of the propagation distance z is given by

$$w(z) = w_o \sqrt{1 + (z/z_R)^2}, \quad (1.9)$$

$L_p^{|\ell|}$ indicates a generalized Laguerre polynomial and $\zeta(z)$ is the Gouy phase. The Gouy phase $\zeta(z)$ introduces an effective extra phase term proportional to the mode order $|\ell| + 2p + 1$.

Each family of solutions provides a complete representation of transverse spatial modes, as they are comprised of complete sets of orthonormal two-dimensional complex functions. In addition, each basis can be expressed in terms of the others, which allows for instance to obtain Laguerre-Gaussian

modes, eigenstates of OAM, by linearly combining Hermite-Gaussian modes [147]. It should be noted, however, that helical phase fronts also characterize other families of modes that can be used to fully describe the transverse field, such as Ince-Gaussian beams [21] and high-order Bessel beams [13], which therefore also carry orbital angular momentum.

1.3.4 Duality relation between orbital angular momentum and angular position

One of the offshoots of the Englert-Greenberger duality relation in the context of quantum mechanics is the concept of complementarity [137, 98]. Niels Bohr disagreed with Einstein, Podolsky and Rosen's definition of locality [95, 49]. In Bohr's point of view, some types of predictions are possible while others are not, as they depend upon mutually incompatible tests. He defined this notion as *complementarity*, and he proposed it as a means to clarify the apparent paradox arising from the EPR experiment.

It is well known that momentum and position, or time and frequency, are conjugate variables placed in relation to each other by Fourier transforms. Much like position and momentum, angular position and orbital angular momentum are Fourier-related [206].

A phase-shift operator that evolves a state $|\psi\rangle$ with well-defined azimuthal angle and rotates its probability distribution can be introduced:

$$|\psi'\rangle = \exp(-i\hat{L}_z\Delta\phi)|\psi\rangle, \quad (1.10)$$

where \hat{L}_z induces a rotation of magnitude $\Delta\phi$ in the phase probability distribution about the z axis [207]. A phase shift of exactly 2π does not alter the state, which implies the rotational periodicity of the probability distribution and leads to \hat{L}_z having integer eigenvalues. In the phase representation:

$$\exp(-i\hat{L}_z\Delta\phi)\psi(\phi) = \psi(\phi + \Delta\phi). \quad (1.11)$$

Expanding this into a Taylor series, the effect of \hat{L}_z can be rewritten as:

$$\exp\left(\Delta\phi\frac{\partial}{\partial\phi}\right)\psi(\phi) = \psi(\phi + \Delta\phi) \quad (1.12)$$

from which

$$\hat{L}_z = -i\frac{\partial}{\partial\phi}, \quad (1.13)$$

which shows how the generator or rotations \hat{L}_z and the angular position ϕ are conjugate variables [207].

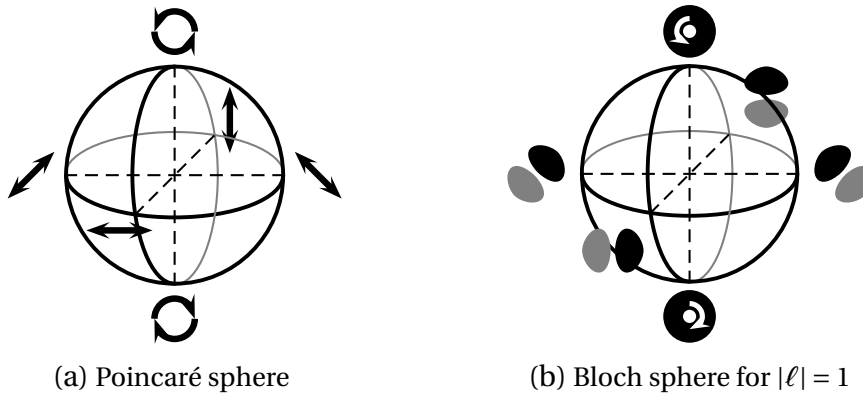
It must be pointed out how the position-momentum Fourier relation fundamentally differs from its angular equivalent. While the former case involves continuous variables, for angular position and orbital angular momentum only the position is continuous. In addition, angular position is cyclic with 2π period, which has raised questions on its being a quantum-mechanical observable and makes its standard deviation ill-defined [25]. By bounding the region of interest within $\pm\pi$, however, we can disregard most of these issues. Owing to the Fourier relation between OAM and angular position, the amplitude of an OAM state can then be expressed in terms of azimuthal angular states:

$$\tilde{\psi}(\ell) = \frac{1}{\sqrt{2\pi}} \int_{-\pi}^{\pi} \psi(\phi) e^{-i\ell\phi} d\phi. \quad (1.14)$$

Correspondingly, states in the angular basis can be expressed in terms of those with well-defined values of OAM:

$$\psi(\phi) = \frac{1}{\sqrt{2\pi}} \sum_{\ell=-\infty}^{+\infty} \tilde{\psi}(\ell) e^{i\ell\phi}. \quad (1.15)$$

Although light can have a fractional net OAM content, it can always be expressed as a series of integer OAM eigenstates [191, 117].



(a) Poincaré sphere

(b) Bloch sphere for $|\ell| = 1$

Figure 1.4: (a) Poincaré sphere and (b) Bloch sphere of first-order Hermite-Gaussian modes expressed as superpositions of Laguerre-Gaussian modes with $|\ell| = 1$. Some polarization and OAM states are indicated. In particular, the modes HG_{10} , HG_{01} , $LG_{0,\pm 1}$ and the diagonal first-order HG modes are shown in (b).

1.4 The angular momentum of light as a quantum resource

One of the most important properties of the orbital angular momentum of light is that the Hilbert space associated with a general OAM quantum state is theoretically unbounded. For any d -dimensional orbital angular momentum subspace with arbitrary d , a complete orthonormal basis set can be defined and the corresponding modes used as the elements of a high-dimensional quantum information alphabet. Just as the two-dimensional state space of polarization can be used to implement qubits (that is, two-level quantum bits), orbital angular momentum has been recognized as a convenient degree of freedom for the physical realization of qudits (higher-dimensional qubits) in quantum information applications.

The mathematical analogy between polarization and OAM subspaces was recognized by Allen, Woerdman and co-workers in their seminal studies in the early 1990s [9, 32]. Their mode converters based on cylindrical lenses, which transform Hermite-Gaussian modes into Laguerre-Gaussian modes, are for OAM the equivalent optical components to waveplates for polarization states. This analogy was highlighted by Padgett and Courtial [202, 10], who represented a two-dimensional OAM mode space with an analogy to the Poincaré sphere. The

Poincaré sphere represents the complex superpositions of any two orthogonal polarization states. Fig. 1.4a shows such a sphere with right- and left-circularly polarized states located at the north and south poles of the sphere, respectively. Their coherent superpositions that result in linear polarization states are placed around the equator, with the longitude corresponding to the orientation of the linear polarization, i.e. the relative phase between the right and left circular components. Intermediate latitudes correspond to elliptical polarization states, with the longitude denoting the orientation of the major axis.

While polarization provides a two-dimensional space, completely described by the Poincaré sphere, the general OAM space is more complex. Transverse modes can be grouped into subsets containing modes of the same mode order, characterized by the same change in Gouy phase upon propagation [146]. For Laguerre-Gaussian modes, the mode order is given by $m = |\ell| + 2p + 1$; for order m , there are $m + 1$ distinct orthogonal modes. It follows that the Laguerre-Gaussian modes with $p = 0$ and $|\ell| = 1$ constitute all the transverse modes of order one, a two-dimensional subspace that can be fully represented on the surface of a sphere analogous to the Poincaré sphere for polarization (fig. 1.4b). For the Bloch sphere of this OAM subspace, the north and south poles are associated with Laguerre-Gaussian modes with $p = 0$ and $\ell = \pm 1$ respectively. Coherent superpositions of these two modes produce first-order Hermite-Gaussian modes, with an orientation that depends on the relative phase between the $\ell = \pm 1$ components.

For Laguerre-Gaussian modes with $|\ell| > 1$, the situation is more complicated since the number of modes of the same order is greater than two. However, it is still possible to consider any subspace of just two modes and their superpositions, whichever their structure [229], and represent them on an appropriate Bloch sphere. For modes with $p = 0$ and opposite values of ℓ , for instance, the states along the equator have intensity cross-sections consisting of a single ring of 2ℓ lobes, with orientation depending on the longitude. The Poincaré sphere equivalent for two-dimensional OAM subspaces has also been used to analyse the frequency shift introduced by a rotation of beams carrying OAM around the propagation axis, where the dynamic phase shift is seen as a geometric or Berry phase [202]. The clear analogy with polarization also lends itself to replicate

experiments on quantum entanglement originally devised for or performed with the polarization of entangled photons.

Photons in transverse modes carrying orbital angular momentum (e.g. sets of Laguerre-Gaussian modes and their superpositions), as well as photons in other degrees of freedom such as time-energy, path and continuous variables [224, 231, 283], have attracted interest for the realization of multi-level quantum systems. The implementation and manipulation of high-dimensional qubits play an important role in several quantum information processes and protocols, including quantum computing [270], quantum key distribution [97, 68, 186], dense coding and teleportation [41, 38].

CHAPTER 2

Production and measurement of OAM-entangled two-photon states

Entangled photon pairs used in quantum optics experiments typically come from the process of spontaneous parametric-down-conversion (SPDC) in a non-linear crystal. High-dimensional entanglement between these photon pairs can broadly be classified into two groups. The first exploits the spectral [19] and temporal [84] degrees of freedom; an experimental system with at least 11 dimensions has been achieved for the latter [84]. The second exploits the spatial degrees of freedom, such as transverse spatial profile [269] and transverse position and linear momentum [285, 131]; an experimental system with a notable channel capacity of 7 bits/photon, corresponding to roughly 128 dimensions, has been reported for the latter [90]. Most relevant to our work are studies exploiting the angular position and the orbital angular momentum (OAM), which relate to the modes with a spiral phase structure defined by the azimuthal index ℓ [161].

2.1 Spontaneous parametric down-conversion

Spontaneous parametric down-conversion (SPDC) is a quantum optical process widely used in quantum optics for the preparation of entangled photons and the implementation of probabilistic heralded single-photon sources. It is based

on the use of nonlinear crystals, whose dielectric polarization does not vary linearly with the electric field of the incident light. The process of parametric down-conversion is related to the second-order dielectric susceptibility tensor $\chi^{(2)}$ that appears in the expansion of polarization

$$P(z, t)/\epsilon_0 \propto \chi^{(1)}E(t) + \chi^{(2)}E^2(t) + \chi^{(3)}E^3(t) + \dots. \quad (2.1)$$

Parametric down-conversion was first described by Kleinman in 1968 as optical parametric noise, in the context of low-gain optical parametric amplifiers and frequency converters [149]. It is often treated in terms of a quantum-mechanical decay process, in which the photons entering an optically nonlinear crystal give rise to the probabilistic production of pairs of lower-energy photons. The three interacting fields are commonly called *pump* (continuous or pulsed), *signal* and *idler*. Since signal and idler are generated in pairs, detecting the idler implies the presence of the signal (and vice versa).

2.1.1 Phase-matching

SPDC, being it a parametric process, therefore leaves the quantum state of the medium unchanged. Energy conservation holds among the incoming photons and the photon pairs produced:

$$\omega_p = \omega_1 + \omega_2. \quad (2.2)$$

In addition, for an undepleted input beam, the efficiency of the emission is highest when the following condition between the three wave vectors is satisfied and the fields are coherent over the full length of the crystal:

$$\vec{k}_p = \vec{k}_s + \vec{k}_i. \quad (2.3)$$

Here $k_j = 2\pi n_j/\lambda_j$, with $j = \{p, s, i\}$, λ_j is the wavelength and n_j the wavelength-dependent refractive index of the nonlinear medium.

Signal and idler photons are emitted within two different cones tangent

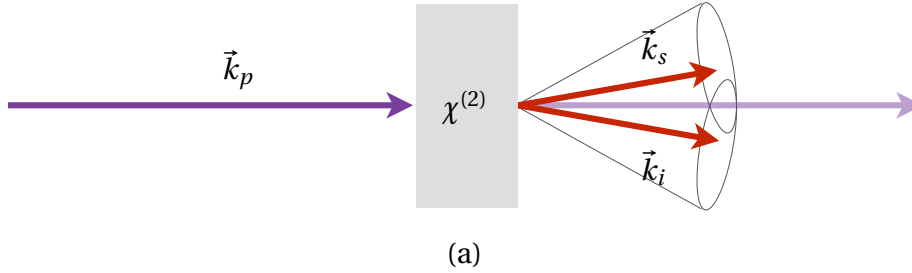


Figure 2.1: In the process of parametric down-conversion, a pump photon probabilistically induces the production of pairs of photons phase-matched in the frequency domain and with correlated polarizations.

or partially overlapping, whose vertices correspond to the active spot in the crystal (fig. 2.1). The importance of spatial correlations in two-photon sources was pointed out as early as 1974 by Clauser and Horne, who highlighted the relevance of direction correlations in addition to polarization correlations in experimentally attainable tests of local hidden variables [75]. The frequencies of the three fields, and the physical and geometrical properties of the crystal, are such that at least condition (2.2) is always satisfied. When both relations (2.2) and (2.3), known collectively as the *phase-matching* conditions, are met, we are in what is called perfect phase-matching, i.e. $\Delta\vec{k} = 0$ (fig. 2.2). The process thus produces pairs of photons phase-matched in the frequency domain and with correlated polarizations. It is thanks to the phase-matching conditions that SPDC provides such spatial correlations for photons emitted within very narrow cones.

In order to achieve phase matching in birefringent crystals, the highest-frequency wave is polarized in the direction that encounters the lower refractive index in the medium. Phase matching in SPDC can take place in two different configurations. If the signal and idler photons are produced with the same polarization, the SPDC process is said to be type I. In type-II down-conversion, on the other hand, signal and idler are produced with orthogonal linear polarizations, causing them to experience different refractive indices within the birefringent crystal.

An experiment using SPDC for the production of polarization-entangled photons was first implemented in 1988 by Shih and Alley, using a monopotassium

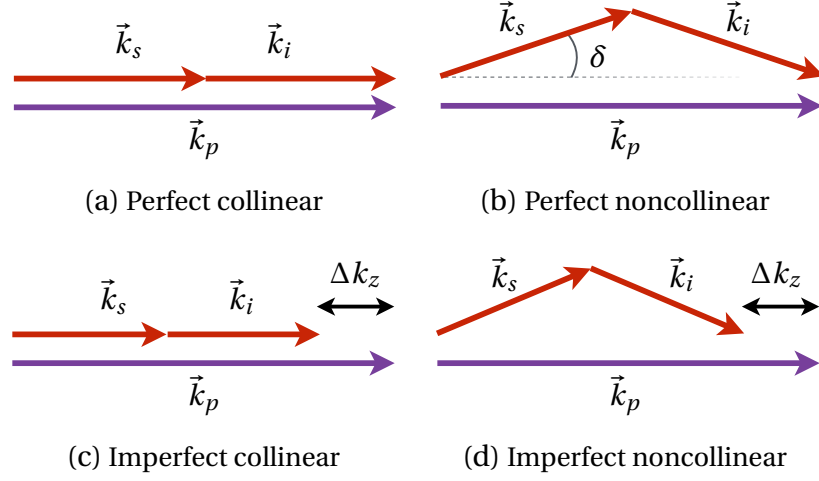


Figure 2.2: Pump, signal and idler wave vectors in SPDC. (b) The phase-matching conditions can be tuned such that the wave vectors of the signal and idler photons, \vec{k}_s and \vec{k}_i , point away from the direction of the pump vector. (d) The mismatch in the longitudinal component z is denoted as Δk_z . The transverse momentum is however conserved.

phosphate crystal [243]. Once the frequency and direction of the pump beam have been chosen, and the geometrical properties of the crystal appropriately tuned, the emission angles of the photons emitted by the crystal are well-defined. The plane containing their propagation axes, however, remains undefined. By imposing appropriate phase-matching conditions, the two emission cones can be made to intersect. By selecting light from the intersection of the two rings, this configuration has been used as a source of polarization-entangled photons [155]. Only the entangled state of the photons produced in spatial modes A and B , determined by the intersections of the cones symmetrical with respect to \vec{k}_p , is therefore considered:

$$|\psi\rangle = \frac{1}{\sqrt{2}} \left(|H_A, V_B\rangle + e^{i\phi} |V_A, H_B\rangle \right), \quad (2.4)$$

where H and V represent two orthogonal linear polarizations. The relative phase between the two terms can be altered by inserting a waveplate in one of the two paths, or changing the crystal orientation.

For the purposes of the experimental work presented in this thesis, we chose

to use a type-I β -barium borate (BBO) crystal. In this down-conversion configuration, the signal and idler photons, which have the same polarization, are emitted in a single narrow cone coaxial with the pump beam axis. As previously mentioned, the efficiency of the down-conversion process strongly depends on the wave vector mismatch $\Delta\vec{k} = \vec{k}_p - \vec{k}_s - \vec{k}_i$ between the three interacting fields. In up-conversion processes, such as sum-frequency and second-harmonic generation, the concept of phase matching directly affects the intensity of the up-converted beam. If the longitudinal length L_z of the nonlinear crystal is greater than $1/\Delta k$, the output wave can become out of phase with the driving polarization and the power can flow back into the two input waves. The phase-matching conditions of down-conversion processes are less stringent.

A summary of the first-order perturbative approach of [127] is presented here. Following the treatment given in [181], one can express the state produced by SPDC in terms of the three wave vectors:

$$|\psi\rangle = |0\rangle + A \int d\vec{k}_s \int d\vec{k}_i \operatorname{sinc} \left[\frac{1}{2} (\omega_p - \omega_s - \omega_i) t \right] \Phi(\vec{k}_s, \vec{k}_i) |1, \vec{k}_s\rangle |1, \vec{k}_i\rangle \quad (2.5)$$

where A is an arbitrary constant, $|n, \vec{k}_s\rangle$ and $|n, \vec{k}_i\rangle$ are Fock states for the signal and idler modes,

$$\begin{aligned} \Phi(\vec{k}_s, \vec{k}_i) = & \int d\vec{q}_p v(\vec{q}_p) \left[\frac{\omega_s \omega_i \omega_p}{n^2(\vec{k}_s) n^2(\vec{k}_i) n^2(\vec{k}_p)} \right]^{1/2} \\ & \times \prod_{j=\{x,y,z\}} \operatorname{sinc} \left[\frac{1}{2} (\vec{k}_p - \vec{k}_s - \vec{k}_i) L_j \right] \end{aligned} \quad (2.6)$$

and \vec{q}_p is the transverse component of the pump wave vector, $v(\vec{q}_p)$ is the angular spectrum of the pump beam, n is the wave vector-dependent refractive index of the nonlinear medium, and L_j the three spatial dimensions of the crystal. If we place appropriate narrow-band interference filters in front of the detectors, as is usually the case in SPDC experiments, we only select the degenerate frequencies of interest ω_s and ω_i . By considering this monochromatic case, corresponding to (2.2), the time dependence in (2.5) disappears.

The transverse profile of the pump is usually smaller than the cross-section

area $L_x L_y$ of the nonlinear crystal. If one can effectively neglect boundary effects and take the transverse dimensions to approach infinity, the process is invariant with respect to transverse translation and the conservation of transverse linear momentum $\vec{q}_p = \vec{q}_s + \vec{q}_i$ holds unconditionally. If however the crystal has finite length (i.e. comparable to the beam size), the process is not invariant to translation along the longitudinal direction z . The pump is also taken to have narrow angular spectrum and the modes are examined for what will be referred to as collinear or near-collinear phase matching conditions, that is, $q \ll k$. In the experimental context, the collinear case is taken to represent the maximum experimentally achievable collinearity conditions for a pump of finite size¹. Under these assumption, we can take the refractive indices encountered by the three waves as constants in (2.6). Hence:

$$\Phi(\vec{k}_s, \vec{k}_i) = \nu(\vec{k}_s + \vec{k}_i) \operatorname{sinc} \left[\frac{1}{2} (k_{p,z} - k_{s,z} - k_{i,z}) L_z \right]. \quad (2.7)$$

The effect of phase matching on the two-photon state $|\psi\rangle$ can be readily observed in the far-field distribution of the down-converted light. The profile of the down-conversion emission can be described as a function of the phase-matching term in (2.6):

$$E \propto \operatorname{sinc} \left[\frac{1}{2} \Delta k_z L_z \right]. \quad (2.8)$$

If close to collinearity, we find that $\omega_s \simeq \omega_i \simeq 2\omega_p$ and the phase mismatch can be approximated by

$$\Delta k_z \simeq k_p - k_s - k_i + \frac{1}{2} (k_i + k_s) \delta \quad (2.9)$$

where δ is the angle between k_p and either k_i or k_s within the crystal. In case of perfect phase-matching (exact degeneracy) and collinearity, only the δ -dependent term survives. The far-field intensity I can therefore be expressed

¹The observable spiral bandwidth (sec. 3.1) associated with our experimental conditions is therefore always non-zero, as opposed to theoretical collinear SPDC.

in the form:

$$I \propto |E|^2 \simeq \text{sinc}^2(\alpha + c\theta^2) \quad (2.10)$$

where $\theta = n\delta$ is the external emission angle in air, $c = (k_s + k_i)L_z/(2n)^2$ is a constant depending on the experimental parameters and the refractive index n for the signal and idler wavelengths, and $\alpha = (k_p - k_s - k_i)L/2$ determines the degree of noncollinearity of the process [213].

One can image the far field of the crystal using a lens with focal length f placed at distance f from the active spot of the nonlinear crystal. When looking at the focal plane of the lens with a camera, for convenience of notation the intensity profile (2.10) can be alternatively expressed as

$$I(r) \propto \text{sinc}^2\left[\alpha + c\left(\frac{r}{f}\right)^2\right], \quad (2.11)$$

where r indicates the radial coordinate in the focal plane of the lens. The intensity profile so captured can be fitted using the mismatch parameter α as a free parameter (fig. 2.3). Careful tuning of the temperature of the crystal (for lithium niobate or potassium titanyl phosphate, for instance) or its angular orientation with respect to the propagation direction of the incident light (for β -barium borate) allows to control the phase-matching conditions to achieve the desired wave vector mismatch and corresponding opening angle of the SPDC emission.

2.1.2 The Klyshko advanced wave model

In parametric down-conversion, a field is periodically transformed from a vacuum state to an excited state $|\psi\rangle$ that corresponds to the propagation of two correlated photons. Earlier on, SPDC was not exploited as a source of entanglement, a potential application that was only recognized in the late 1980s [243]. Using SPDC from an ammonium dihydrogen phosphate crystal as a source of correlated photon pairs, in 1970 Burnham and Weinberg verified the underlying physical interpretation of the parametric fluorescence process as two-photon quantum decay by simultaneous detection of the signal and idler photons [64].

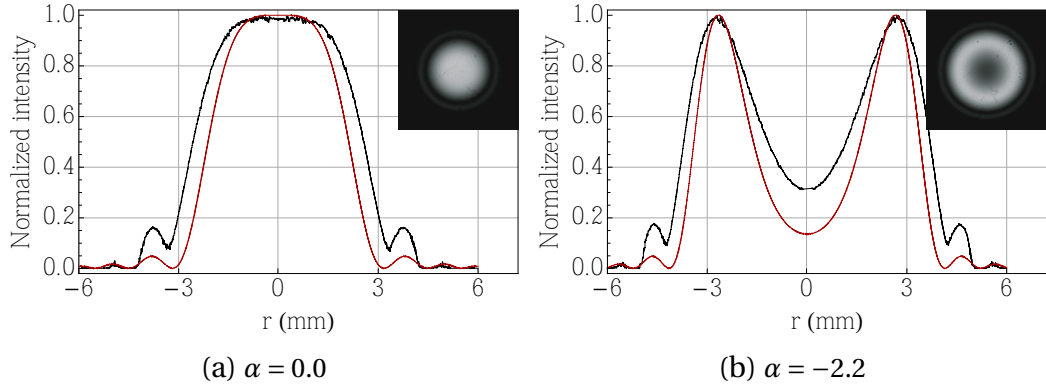


Figure 2.3: (a) For collinear phase matching, the cross-section of the azimuthally averaged intensity profile (inset) takes the form of a bright spot, with side lobes due to the sinc phase-matching term. The detected intensity is shown in black, the theoretical profile from eq. (2.11) in red. (b) In noncollinear SPDC, where signal and photons are emitted with opposite transverse momenta, the light forms a bright ring, surrounded by rings of decreasing brightness.

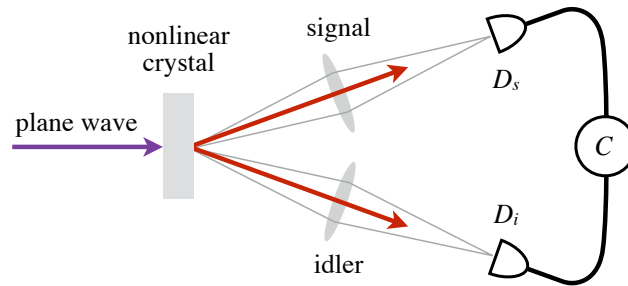
This simultaneous detection, possible if the detectors are arranged to satisfy energy and momentum conservation and to have equal time delays, is commonly referred to as coincidence detection.

By setting the detectors to measure signal and idler in states $|\psi_s\rangle$ and $|\psi_i\rangle$ respectively, the coincidence rate is proportional to the joint probability of detection, which can be expressed as

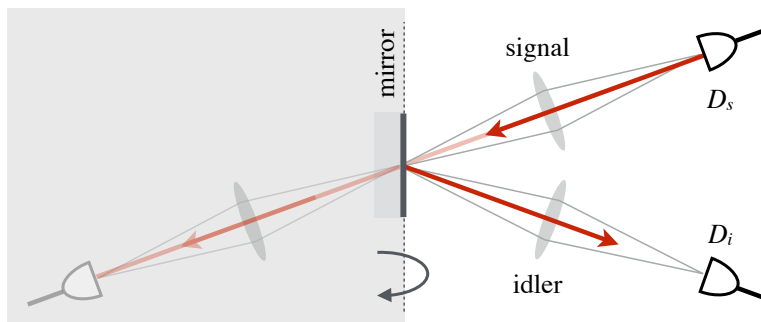
$$P(\psi_s, \psi_i) = |\langle \psi_i | \langle \psi_s | \psi \rangle|^2. \quad (2.12)$$

In 1988, David Klyshko introduced an advanced-wave retrodiction model to predict the outcome of coincidence experiments [150]. In a retrodictive model, a quantum system at any point in time previous to the measurement is described in terms of its measured state, evolved backwards in time [5, 6, 248]. Following the treatment of retrodiction presented by Barnett et al. [26], one can view an SPDC system in classical terms where one treats the signal detector as a light source, the crystal as a mirror and the idler detector reading as a predictor for coincidences (fig. 2.4).

Any measurement settings for the detection arms of the signal and idler photons will be collectively described in terms of detectors D_s and D_i respectively.



(a) Generic SPDC detection scheme



(b) Back-projection model

Figure 2.4: A generic experiment where photons are produced in parametric down-conversion is shown in (a). In (b), the intensity detected by D_i after the mode emitted by D_s is propagated through the system is proportional to the coincidence count C observed in (a).

In order to predict the coincidences in the Klyshko picture, the photons are ‘back-propagated’ from detector D_s in the mode corresponding to the pure state $|\psi_s\rangle$, through the components along the path of the signal arm (such as lenses and mirrors). The nonlinear crystal is replaced by a mirror, in the assumption of a plane-wave pump and perfect phase matching. After the reflection, the mode propagates forward through the components in the idler arm and is detected by D_i .

In this classical model, which considers an advanced wave rather than a two-photon wavefunction, one can numerically predict the expected coincidence rates from the Born rule. The coincidence probability is proportional to the overlap integral of the three modes at the crystal plane, with $\tilde{\psi}_s$ the back-propagated

mode in the signal arm [102]:

$$P(\psi_s, \psi_i) \propto \frac{|\int_{-\infty}^{\infty} dr \tilde{\psi}_s^* \psi_i^* \psi_p|^2}{\sqrt{\int_{-\infty}^{\infty} dr |\tilde{\psi}_s^* \psi_p|^2 \int_{-\infty}^{\infty} dr |\psi_i^* \psi_p|^2}}. \quad (2.13)$$

Predictions based on this retrodiction model were used in classical simulations (both numerical and experimental, using coherent light) of all the experiments presented in this thesis, and allowed accurate alignment and optimization of our detection system.

A more complete ‘double-Klyshko’ treatment able to account for any phase-matching conditions, finite crystal length and the position of the foci of the detection modes inside the bulk crystal, should include a volume integral over the entire crystal of both back-propagated modes $\tilde{\psi}_s$ and $\tilde{\psi}_i$, the pump ψ_p and the phase-matching function W [88]:

$$P(\psi_s, \psi_i) \propto \int_{-L/2}^{L/2} dz \int_{-\infty}^{\infty} dr \tilde{\psi}_s^*(r, z) \tilde{\psi}_i^*(r, z) \psi_p(r, z) W(z). \quad (2.14)$$

2.2 Entanglement of orbital angular momentum

Since the first experiment that employed parametric down-conversion to produce polarization-entangled photons for which Einstein-Podolsky-Rosen-Bohm correlations were observed [243, 95, 46], SPDC has been used as a source of entangled photons in a wide range of experiments. The entanglement of down-converted photon pairs has been investigated in several degrees of freedom – including time-energy, linear momentum and spatial modes, such as those carrying orbital angular momentum [131, 221, 252, 268].

The first experimental demonstration of the conservation of orbital angular momentum for down-converted photon and OAM entanglement in the SPDC process was carried out by Zeilinger and co-workers in 2001 [172]. In order to verify the conservation of OAM, the photons were detected using a combination of computer-generated holograms and single-mode fibres (see section 2.3.2 for details). In order to justify the conservation of OAM it could be enough

to suppose the existence of classical correlations between the photon pairs generated, without any need for quantum correlations. To confirm the presence of entanglement between the photons in each pair it must be shown that they are not just a mixture of the permutations allowed by conservation of angular momentum but rather a coherent superposition.

Zeilinger and co-workers confirmed that, for a Gaussian pump beam, the signal and idler photons can take on a range of OAM values. However, once the signal OAM was determined, the idler photon from the same pair always had the opposite value. These results are in agreement with previous research by Monken and co-workers, who showed that the angular spectrum of the pump is transferred to the properties of the transverse correlation of the signal and idler photons [181]. Since then, their group has investigated the conservation of OAM in SPDC in more detail, showing that in fact it is the transfer of the pump angular spectrum that leads to the conservation of OAM [268].

By considering a pump beam carrying no orbital angular momentum, $\ell_p = 0$, the entangled state that describes the generated pairs takes the general form

$$\begin{aligned}
 |\psi\rangle = & c_{0,0} |0\rangle |0\rangle \\
 & + c_{1,-1} |1\rangle |-1\rangle + c_{-1,1} |-1\rangle |1\rangle \\
 & + c_{2,-2} |2\rangle |-2\rangle + c_{-2,2} |-2\rangle |2\rangle + \dots
 \end{aligned} \tag{2.15}$$

where $|\ell\rangle |-\ell\rangle = |\ell_s\rangle \otimes |\ell_i\rangle$ for brevity, in the general case of an arbitrary number of OAM eigenstates for signal and idler, where coefficients c_{ℓ_s, ℓ_i} indicate the probability amplitude associated with state $|\ell_s\rangle |\ell_i\rangle$.

While showing that OAM is conserved in down-conversion indicates correlations between ℓ_s and ℓ_i , it does not constitute in itself a proof of OAM entanglement. Unlike classical correlations, quantum correlations contain a phase dependence that can be tested by showing correlations for both OAM eigenstates and their superpositions. In the analogy with polarization, any linear polarization state can be regarded as a superposition of right and left circularly polarized states; the phase between the left and right components sets the orientation of the resulting linear polarization. The strength of the polarization correlations between signal and idler photons depends upon the relative orien-

tation of the linear polarizers used in the measurements. This is equivalent to a dependence on the relative phase between the circular state components of each individual beam. For OAM, superposition states can be created by deliberately moving the hologram so that the fork dislocation is no longer centred within the beam. The relative phase of the modes in the superposition so produced is set by the direction and magnitude of the transverse displacement.

Zeilinger and co-workers displaced the hologram in the signal arm and, with the idler hologram removed, scanned the transverse position of the detector in the idler arm. This resulted in a coincidence curve in which the position of the minimum corresponding to the phase singularity was also displaced by the same amount [172]. Had the correlation instead been classical, one would have expected the coincidence minimum to remain at the centre, albeit washed out. The shift in the minimum confirmed that the observed nonlocal correlations in the measurement of the OAM content of the two photons are phase-dependent and therefore quantum in nature: the state of the photon pair generated by SPDC, expressed in the OAM basis, is an entangled state.

Determining the distribution of the orbital angular momentum modes over which down-converted photons are entangled, that is, the experimentally accessible subset of the terms of (2.15), is crucial in quantum information applications based on the availability of specific quantum states. Experimentally, only a small angular section of the SPDC emission cones is usually considered. The wave vectors of signal and idler photons belong to small cones coaxial with the corresponding central wave vector, making it possible to neglect conditions of the overall system that may lead to violations of the conservation rule [255, 102]. The condition $\ell_p = \ell_s + \ell_i$ is only valid for certain emission angles and Poynting vector walk-off [257, 195]. The latter effect can be reduced by using a sufficiently wide pump beam [172, 268]. In the opposite case, that is, using geometries based on highly focussed pump beams, nonlinear effects can be accentuated. Noncollinear SPDC configurations introduce ellipticity in the spatial modes of the down-converted modes, which may lead to the observation of pairs for which the selection rule on OAM is violated.

A complete characterization of the state of an entangled system can be carried out using the Schmidt decomposition [96]. Expressing the state in the

Schmidt basis highlights the type of correlation as well as the number of modes involved. In the SPDC case, expressing the transverse components of the signal and idler wave vectors as \vec{q}_s and \vec{q}_i , the two-photon state produced by SPDC can be rewritten in the form

$$|\psi\rangle = \int d\vec{q}_s \int d\vec{q}_i C(\vec{q}_s, \vec{q}_i) |\vec{q}_s, \vec{q}_i\rangle \quad (2.16)$$

where $C(\vec{q}_s, \vec{q}_i)$ is the amplitude of the two-photon state $|\vec{q}_s, \vec{q}_i\rangle$ [267]. The Schmidt decomposition of $C(\vec{q}_s, \vec{q}_i)$ can be shown to correspond to the expansion

$$C(\vec{q}_s, \vec{q}_i) = \sum_{n=0}^{\infty} \sqrt{e_n} u_n(\vec{q}_s) v_n(\vec{q}_i), \quad (2.17)$$

where $u_n(\vec{q}_s)$ and $v_n(\vec{q}_i)$ are Schmidt modes given by the eigenvectors of the reduced density matrices for signal and idler, and e_n the corresponding eigenvalues [159]. Because density matrices always have finite trace, the Schmidt decomposition is always discrete, even when the original is intrinsically continuous or, such as in this case, doubly continuous.

The functions u_n and v_n form a complete and orthonormal basis. With the exception of Gaussian states, however, u_n and v_n do not directly correspond in general to states carrying well-defined orbital angular momentum that are experimentally accessible in the detection for SPDC implementations. The direct implementation-independent manipulation of Schmidt modes, which in general are not associated with any physical property but represent fundamental entities in quantum information and characterize the structure of the entanglement, remains an open problem.

2.3 Experimental methods

2.3.1 Collinear parametric down-conversion with BBO crystals

Parametric down-conversion is used as a source of entangled photon pairs. We employed a set of β -barium borate (BBO) crystals with different lengths, each of which could be mounted onto a goniometric stage that allowed precise repeatable rotations around the horizontal axis (orthogonal to the pump direction) with accuracy of around 0.1° , in order to tune the phase-matching conditions.

Down-converted light was produced by optically pumping the crystal with a 2W mode-locked solid-state Coherent Paladin laser source at 355 nm, with 120 MHz repetition rate and a beam waist diameter at $1/e^2$ of 1 mm. The pumping power could be reduced to 1 W using a system of ultraviolet broadband plate beam splitters arranged at the output of the laser. The low beam divergence was further improved by the use of a $4f$ imaging system placed between the laser output and the input face of the crystal. The high stability of the laser output power and its low noise made the laser source employed ideal for measurements in low-light conditions, which, in order to collect significant photon counts, can take place over extended periods of time.

The BBO crystals were cut for type-I SPDC, for which the down-converted photon pairs leave the crystal with an angle with respect to the pump propagation direction determined by the orientation of the crystal, i.e. the phase-matching conditions. The pump beam residue after the crystal was blocked by a longpass reflective interference filter. The signal and idler fields at the output of the crystal were imaged and magnified by a $4f$ afocal imaging system composed of lenses with focal lengths $f_1 = 200$ mm and $f_2 = 400$ mm (fig. 2.5).

In this configuration, the co-propagating signal and idler photons were separated by a balanced non-polarizing beam splitter. In both conditions considered, the aperture of the down-conversion cone was small enough to be effectively negligible at the SLM plane. We used a pellicle beam splitter to suppress multiple internal reflections and ghosting when operating the system in back-projection. Using type-I down-conversion and a non-polarizing beam splitter reduces the

2.3.2 Phase-flattening measurements with spatial light modulators

In order to carry out measurements of OAM modes, we need to introduce a component equivalent to a polarizer able to operate in the larger state space of OAM. An OAM ‘polarizer’ should be able to perfectly discriminate between any number of orthogonal OAM states, and let any light through only if the measurement setting matches the OAM content of the incident transverse mode. In the early 1990s, Soskin and co-workers [29] and Heckenberg and co-workers [125] pioneered the use of diffractive optical elements for the generation of beams with helical wavefronts. Their teams showed that, when a diffraction grating containing an ℓ -fold edge dislocation was illuminated with a Gaussian beam, the first-order diffracted beam had an annular intensity cross-section consistent with helical phase fronts described by a phase cross-section of the form $\exp(i\ell\phi)$ (eq. (1.8)). Beams carrying any amount $\ell\hbar$ of OAM can be generated through diffraction off a suitable hologram. When operated in reverse, these holograms can also be used to detect the OAM of an incident mode.

In general, a grating hologram is obtained by adding a blazed linear grating (modulo 2π) to a given phase distribution. These holograms operate by shifting the desired phase information into the first diffraction order. By adding a blazed grating modulo 2π to a phase distribution corresponding to a spiral phase with topological charge ℓ [29], one obtains a ‘forked’ hologram where the fork dislocation induces the phase singularity and the number of prongs correspond to the charge ℓ of the hologram.

When a beam with an ℓ helical phase structure is diffracted by a forked hologram with topological charge $-\ell$, it is converted in the first diffraction order into a fundamental Gaussian beam, which can in turn be coupled into a single-mode fibre (SMF). Varying the order ℓ of the singularity of the hologram pattern until light is detected in the single-mode fibre allows the determination of the charge ℓ of the incident light (fig. 2.6). If the detector is sensitive to low-intensity signals in the single-photon limit, the combination of holographic diffraction grating and single-mode fibre acts as a device that allows projective measurements of the OAM eigenstates of single photons.

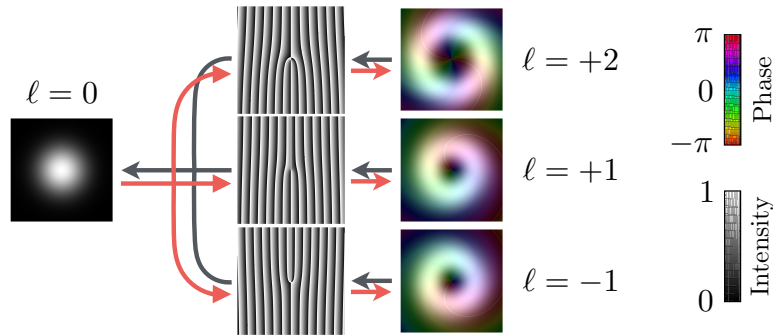


Figure 2.6: Spatial light modulators (SLMs) are diffractive optical devices that can be programmed with phase and amplitude holograms to transform a Gaussian mode into any spatial mode of choice (red arrows). When operated in reverse, the same holograms can efficiently couple the same complicated mode distribution back into a single-mode fibre (grey arrows).

Using appropriate forked holograms, in 2001 Zeilinger and co-workers measured the OAM content of single photons produced by SPDC and investigated quantum correlations in OAM [172]. They showed that OAM is conserved in the parametric down-conversion process: as previously described, for a Gaussian pump beam (carrying no angular momentum) they found highest coincidence rates when the OAM of the signal photon (ℓ_i) was opposite to that of the idler photon (ℓ_s). More generally, they showed that the OAM was conserved, $\ell_s + \ell_i = \ell_p$, for pump beams with $\ell_p = -1, 0$ and $+1$. The conservation of OAM can be understood as a direct consequence of phase matching in SPDC [102]. It is important to point out that the signal and idler beams have independently low spatial coherence, and both are a mixture of many different OAM eigenstates. Correlations only emerge at the level of the individual photon pairs and are averaged out when the measurements consider many photon pairs. As a consequence, the detection of quantum correlations has to rely on single-photon detection.

Although computer-generated holograms printed on standard photographic film proved efficient and versatile [14], they are also difficult to replace and align. Spatial light modulators (SLMs) represent an alternative and an improvement on the concept. SLMs are adaptive optical devices in which a matrix of liquid crystals is enclosed within glass on one side and overlaid on top of a silicon chip

on the other. The orientation of the liquid crystals can be controlled by changing the voltage applied, thus inducing a spatially variable phase delay to the incident light. The phase modulation ranges from 0 to 2π in 256 discrete voltage steps per pixel. Even though the Hamamatsu LCOS-SLMs used only act on the phase of the incoming transverse mode, they can also be used to modulate the intensity of the light. In order to detect a spatial mode with phase $\Phi(x, y)$ and normalized amplitude $A(x, y)$, the phase structure $\Phi_h(x, y)$ to be encoded on the hologram that produces a Gaussian mode in the first diffraction order for the given input can be calculated as:

$$\Phi_h(x, y) = [\Phi(x, y) + \Phi_g(x, y)]_{\text{mod } 2\pi} \times \text{sinc}[(1 - A(x, y))\pi], \quad (2.18)$$

where $\Phi_g(x, y)$ corresponds to the phase distribution of the diffraction grating, and the second term introduces an amplitude-dependent distortion [83, 15, 51]. The power redirected into the first order can be adjusted by changing the greyscale contrast of the diffraction grating blazing function. The phase response of the SLMs is not uniformly linear over the full 2π range. A greyscale calibration curve was then produced by considering the measured count rates in the first order as a function of the greyscale contrast, in order to modulate the pixel value to obtain the desired phase.

By re-programming the holograms displayed on the computer-controlled SLMs, any arbitrary phase structure can be produced or, if used with single-mode fibres, measured. This makes the use of SLMs particularly convenient in systems where a large number of different holograms are used for phase-flattening measurements. Once the pitch and the centre of the hologram have been set to correctly couple the first-order output into the detection fibre, the encoded phase distribution can be changed without introducing any misalignment. The optimization of the grating angles and centre positioning can be entirely automated, making it possible to acquire data over long periods of time without any manual adjustment or drift compensation [134]. As shown, SLMs can also be employed to measure not just the phase modulation of spatial modes, but also their amplitude; this process however will naturally incur additional loss, as the diffraction efficiency of portions of the hologram has to be artificially

suppressed and part of the incoming light redirected into the zero diffraction order. This is on top of the significant loss already introduced by SLMs, of the order of 40%, which represents the main drawback to their flexibility.

The efficiency of SLMs depends on the transverse structure of the incident light, namely on its OAM content and the presence of higher-order radial modes [179, 234]. In phase-flattening measurements, the diffracted field does in fact retain a ringed intensity pattern due to its being a non-trivial superposition of radial modes. Only the fundamental mode with no radial discontinuities couples into a SMF. For the measurement holograms presented, one can choose appropriate beam waist sizes and radial indices such that most of the light is diffracted into the first order [220].

To avoid pixellation and a reduction of diffraction efficiency, it is important that a large enough number of pixels of the SLM are illuminated. This is the reason the down-conversion output is expanded to fill more of the liquid crystal layer of each of the two SLMs. Completely filling the diffractive window, however, would introduce the need for aberration correction, as the liquid crystal layer is not completely flat over the entire 1.9 cm^2 , 800×600 -pixel area. In addition, the polarization of the incoming light is rotated in each arm using half-wave plates to maximize to the first-order efficiency of the SLMs.

2.3.3 Coincidence detection

The first-order output of the SLMs were collected by single-mode fibres, onto which the SLMs outputs were imaged by a combination of a lens with $f_3 = 600 \text{ mm}$ and an objective with $f_4 = 3.2 \text{ mm}$. Bandpass filters of width 2 nm and centred at 710 nm were placed in front of the fibres to ensure signal and idler photons were measured near degeneracy. Each SMF was connected to a Perkin Elmer silicon avalanche photodiode (APD), the output of which was fed to a coincidence circuit with a timing window of 10 ns . The APDs operated at 710 nm with a quantum efficiency of 60% , with a nominal dark count rate of 20 s^{-1} and an effective rate of about 200 s^{-1} in our laboratory conditions.

Aligning the optical system in the single-photon regime can be a significant

challenge. Back-propagation provides a method to simplify this process, leaving the fine-tuning to be performed with down-converted light. When operating the system in reverse, in the Klyshko model, a laser diode at approximately 710 nm was shone from both single-mode fibres of the coincidence detection set-up back towards the SLMs. The light propagating through both arms of the system could be observed at a plane located at the same distance f_1 from the crystal plane, by placing a removable mirror in the beam path that redirects the light to a CCD camera (fig. 2.5). This allowed us to check the overlap of the signal and idler beams as they propagated through the respective correct optical paths, determined by apertures placed in the system. Observing the beam overlap and the interference fringes at the crystal plane facilitated the alignment of the optical system and to achieve the conditions that lead to coincidence counts.

The curvatures of the signal and idler beams can be mismatched, but must complement each other (i.e., if the signal is concave, the idler must be convex). This is because, in the back-projection model, the curvature of the back-projected beams at the crystal plane must match the pump curvature (which is flat). The set of lenses between the crystal and the SLMs imaged one onto the other afocally, and made it unnecessary to encode field lenses on the SLMs to adjust the curvature of signal and idler (sec. 3.1.4).

CHAPTER 3

Generation of high-dimensional OAM-entangled states

Much attention has been directed to the two-dimensional state space of photon polarization, which provides both a conceptually and experimentally accessible test bed [17, 113, 130, 107]. An even more fertile test bed, however, is d -dimensional two-photon entanglement, wherein each photon is a d -level qudit taking on any of d possible values. From a fundamental standpoint, higher-dimensional entanglement implies stronger violations of locality [79, 81] and is especially useful in the study of mutually unbiased bases in higher dimensions [274]. More relevant to practical applications, higher-dimensional entanglement provides increased security and robustness [30, 31, 285] and a higher information capacity [31, 269, 90].

The entanglement of orbital angular momentum (OAM) in photons gener-

This chapter includes material previously published in the following papers:

- F. M. Miatto, D. Giovannini, J. Romero, S. Franke-Arnold, S. M. Barnett and M. J. Padgett, “Bounds and optimisation of orbital angular momentum bandwidths within parametric down-conversion systems”, *Eur. Phys. J. D* 66(7), 178 (2012)
- J. Romero, D. Giovannini, S. Franke-Arnold, S. M. Barnett and M. J. Padgett, “Increasing the dimension in high-dimensional two-photon orbital angular momentum entanglement”, *Phys. Rev. A* 86(1), 012334 (2012)
- J. Romero, D. Giovannini, M. G. McLaren, E. Galvez, A. Forbes and M. J. Padgett, “Orbital angular momentum correlations with a phase-flipped Gaussian mode as pump beam”, *J. Opt.* 14(8), 085401 (2012)

ated via spontaneous parametric down-conversion (SPDC) is firmly established theoretically and experimentally [102, 172]. The interest in OAM stems from its discrete and theoretically unbounded Hilbert space: since at least in principle ℓ could be any integer, the OAM state space offers a vast choice of d -dimensional subspaces. Since the pioneering experiment of Mair et al. [172], OAM as well as its conjugate variable, angular position, have been steadily gaining ground as a mainstream variable in which to observe quantum correlations. Bell-type and Leggett inequalities have both been violated in two-dimensional OAM subspaces analogous to experiments previously carried out for polarization [162, 228].

The number of OAM spatial modes of the two-photon entangled state generated in SPDC is generally referred to as the *spiral bandwidth* [255]. Any practical experiment utilizing the innate d -dimensional entanglement of the orbital angular momentum of photons is constrained by both the generation capacity of the entangled photon source and the modal capacity of the detection system. The *generation spiral bandwidth* is the number of OAM modes that are produced by SPDC. The generation spiral spectrum of SPDC (i.e., the range of d entangled OAM states and their respective generation probability amplitudes) has previously been calculated analytically from the coincidence fringe obtained from a clever angular equivalent of the Hong-Ou-Mandel interferometer using bucket detectors [87]. On the other hand, the *measurement spiral bandwidth* is the number of OAM modes that can be effectively detected, and it depends on the generation spiral bandwidth and detection capability of the system.

Pors et al. [216] have calculated the size d of the measured spiral bandwidth from coincidence fringes as angular phase plate analysers are rotated: d is the inverse of the area under the peak-normalized coincidence fringe. Using this technique, a dimensionality of $d = 6$ has been measured for a SPDC system with a Schmidt number of 31. Another technique is to measure the OAM states of the signal and idler photons directly by forked diffraction holograms and build up a measurement spiral spectrum, as was done by Dada et al. [81], where they have proved 11-dimensional OAM entanglement via generalized Bell inequalities. Using angular slits and forked diffraction holograms, Leach et al. successfully demonstrated the Einstein-Podolsky-Rosen paradox by measuring angular position and 15 different OAM states, although they did not obtain

the dimensionality of the measured OAM entanglement [161].

By tuning the phase matching, it is possible to demonstrate an increase of the half-width of the OAM-correlation spectrum of a factor of two and above. Additionally, we measured correlations in the conjugate variable, angular position, and obtained high values of the entanglement measure known as concurrence. The good entanglement measures in both OAM and angular position bases indicate bipartite, d -dimensional entanglement where d is tunable. We quantified the dimensionality of OAM entanglement via the quantum mutual information capacity, the information that is shared by the entangled photons. This is an especially meaningful quantity for quantum key distribution [90, 61, 163] and has not been measured for OAM previously. An experimental quantum mutual information capacity as high as 4.94 bits/photon, corresponding to a dimensionality of around 30, was achieved (sec. 3.2).

3.1 Spiral bandwidth

Any projective measurement of OAM, wherein the OAM of the signal and idler photons are directly measured using a mode transformer (with a hologram or phase plate) and a single-mode fibre coupled to a photon detector, is inherently sensitive to the radial field distribution [87, 262, 229]. Measuring the OAM spectrum in this manner will inevitably result in a spiral bandwidth that is different from the generation bandwidth [87].

To increase the number of measurable OAM modes, one can either optimize the detection system or widen the OAM spectrum of the generated two-photon state. These two are equally important, but optimizing detection is fruitless if the OAM states are not being generated in the first place. The detection geometry is more often fixed but can be designed optimally. The generation bandwidth can be modified by changing the characteristics of the pump beam [255, 178] or by tuning the phase-matching conditions as shown previously, for example, by temperature tuning a periodically poled potassium titanyl phosphate crystal [87].

When it comes to the generation bandwidth of spontaneous parametric-

down-conversion, the frequencies of the pump, signal and idler photons involved in the nonlinear interaction are related as $\omega_p = \omega_s + \omega_i$. There is a range of wave vectors that will satisfy this energy conservation relation, and we can define an on-axis phase mismatch Δk_z from the z components of the wave vectors as $\Delta k_z = k_{p,z} - k_{s,z} - k_{i,z}$ [149]. The significance of phase matching was first realized in a seminal paper by Kleinman [149]. In any three-wave-mixing process, $2/\Delta k_z$ is the coherence length over which the three interacting fields remain in phase. In SPDC, Δk_z has implications for efficiency (SPDC is brightest when $\Delta k_z \approx 0$), but more importantly it determines the spectral distribution of the down-converted photons [54, 263]. Theoretical treatment of phase matching is complicated and several approximations have been made [178, 159, 152], but it is easy to do in practice by tuning either the temperature or angular orientation of the crystal [54].

In the case of our bulk β -barium borate (BBO) crystal, changing the angular orientation affects the index of refraction encountered by the pump beam and hence Δk_z and the far-field intensity profile of the down-converted fields. The intensity profile I we obtain mirrors the sinc-phase-matching term in SPDC and is fitted with eq. (2.11)

$$I(r) = \text{sinc}^2\left(\frac{ar^2}{f^2} + \alpha\right) \quad (3.1)$$

where r is the radial coordinate in the focal plane of a lens with focal length f and α is a phase-matching parameter that determines the opening angle of the SPDC emission [213]. In the case where the transverse momentum of the photons is conserved, α is dominated by Δk_z ; we take this as a measure of our on-axis phase mismatch. For the collinear case, $\alpha = 0$.

It can be found that, for any given set of generation parameters (pump waist w_p , wavelength λ , crystal length L) the detection apparatus can be prepared in a way that maximizes the measured number of entangled modes. Two important parameters are γ , the ratio of the width of the pump beam to the width of the detection modes, and L_R , the length of the crystal normalised to the Rayleigh

range of the pump beam:

$$\gamma_{s,i} = \frac{w_p}{w_{s,i}} \quad \text{and} \quad L_R = \frac{L}{z_R}, \quad (3.2)$$

where the Rayleigh range is given by $z_R = \pi w_p^2 / \lambda$. Here we assume that the signal and idler modes have the same width, so that $w_s = w_i$ and $\gamma_s = \gamma_i = \gamma$.

The precise calculation of $w_{s,i}$ depends on the details of the detection system. Our analysis can be applied if the back-projected detection mode size, $w_{s,i}$, is approximately ℓ -independent over the range of OAM of interest, and if the modes with $p \neq 0$ couple only weakly with the fundamental mode of the fibre that carries the signal to the coincidence counter.

We investigate the L_R dependence of the OAM bandwidth, while recognizing that many experiments operate in a regime where $L_R \ll 1$ [172, 27, 136, 191, 81]. In the short crystal limit and near to collinearity, the familiar sinc phase can be dropped [235]. One can then obtain an analytical form for the down-converted state [179, 42] and its extension to non-Gaussian pump beams [279]. Our aim was to go beyond this type of analysis and explore regimes in which the sinc phase matching term becomes significant, which leads to an exact analytical expression and to the characterization of the detection parameters.

For a distribution of probabilities, in our case for the OAM of the signal or idler photon in SPDC, we can define a number of statistical measures. For high-dimensional entanglement we require as many modes as possible to contribute to the state and, moreover, for these to contribute strongly, that is to have a significant probability. A simple and convenient measure of this quantity is the Schmidt number [160, 159, 216]:

$$K(\{p_i\}) = \frac{1}{\sum_i p_i^2}, \quad (3.3)$$

where the probabilities $\{p_i\}$ are, in our case, those for each of the OAM modes. The measure K gives the effective number of contributing modes and hence the effective dimensionality of the system. In experiments, it is typical to quote the full-width at half maximum as the measure of the bandwidth (FWHM) so as to include only modes that are well above the noise floor. FWHM should

not be confused with K (fig. 3.1a). For simple, symmetrical and single-peaked probability distributions, the Schmidt number provides a convenient measure of the bandwidth. The precise relationship between the Schmidt number and the FWHM depends upon the detailed shape of the distribution but typical of our systems is that the K exceeds the FWHM. For a distribution like this we can define an effective range of modes contributing to the state ranging from ℓ_{\max} to $\ell_{\min} = -\ell_{\max}$ such that $K = 1 + 2|\ell_{\max}|$.

The generation bandwidth is the effective number of entangled modes generated in the SPDC process. As it does not depend on the detection apparatus, it is a function only of the crystal length and of the size of the pump beam, combined into the quantity L_R , defined in (3.2). This bandwidth can be thought of as the dimensionality of the entanglement in OAM and can be calculated through the Schmidt decomposition of the SPDC state [177].

The measurement bandwidth represents the number of modes that a detector will measure in an experiment and depends on both the generated modes and on the overlap of these with the detection modes. In doing so, we need to consider the optics used to image the light onto the detectors and any restriction arising from this, such as a restriction to $p = 0$ Laguerre-Gaussian (LG) modes. The overlap between the generated modes and the back-projected detection modes needs to be maintained both in the image plane and in the far field plane of the crystal: a set-up with high overlap in the image plane may still suffer from low overlap in the far field or vice versa, and this would translate into a decreased modal sensitivity. This overlap requirement plays a central role further on in the derivation of eq. (3.10), which is based on the argument that the angular spread of a generated mode cannot exceed the natural spread of the down-conversion cone.

3.1.1 Analytical treatment of spiral bandwidth

A direct calculation of the measurement bandwidth needs to consider the overlap between the SPDC state and a pair of joint detection modes [255, 179]. This yields a series of complex measurement amplitudes $\{C_\ell\}$, where ℓ labels each

value of the OAM that was measured. The measured Schmidt number (or the measurement bandwidth) is therefore given by the measure K applied to the set of projection probabilities $K(\{p_\ell\})$, where $p_\ell = |C_\ell|^2$. We seek to evaluate this quantity for a Gaussian pump laser, taking full account of the sinc phase-matching term and thus extending the regime of validity of earlier calculations.

We consider the measurement modes for the signal and idler fields to be a pair of LG modes. The LG modes are characterized by two integers ℓ and p and a real positive number w , which represent the OAM quantum number, the radial quantum number and the Gaussian modal width, respectively. For simplicity, we set $p = 0$, which limits our analysis to modes with a single bright ring in the transverse plane. Many of our experiments are designed to detect $p = 0$ modes with a higher efficiency than higher-order modes. We note however, that modes with non-zero p are produced in the SPDC process and, indeed, it is these that make it possible to observe entanglement of three-dimensional vortex knots in SPDC [229].

The SPDC wave function $\psi(\vec{q}_s, \vec{q}_i)$ in momentum space is written as follows, where the subscripts s and i refer to signal and idler modes [255]:

$$\psi(\vec{q}_s, \vec{q}_i) \propto \exp\left(-\frac{w_p^2}{4} |\vec{q}_s + \vec{q}_i|^2\right) \text{sinc}\left(\frac{L}{4k_p} |\vec{q}_i - \vec{q}_s|^2\right). \quad (3.4)$$

Here \vec{q} is the transverse component of the momentum vector \vec{k} , w_p is the pump width, L is the crystal thickness, k_p is the wave vector of the pump. The first term corresponds to the transverse wave vector components of the pump, while the second term represents the phase-matching imposed on the down-conversion process by the nonlinear crystal.

We consider each detection mode to be an LG mode with radial quantum number $p = 0$. In polar coordinates (ρ, ϕ) in momentum space it has the form

$$\text{LG}_\ell(\rho, \phi) = \sqrt{\frac{w^2}{2\pi |\ell|!}} \left(\frac{\rho w}{\sqrt{2}}\right)^{|\ell|} \exp\left(-\frac{\rho^2 w^2}{4}\right) \exp(i\ell\phi). \quad (3.5)$$

The projection amplitude is therefore calculated by evaluating the overlap integral of ψ with two LG modes of opposite OAM (because of angular momentum

conservation) [172, 102, 255]. For given L_R and γ , the result is found to be

$$C_\ell \propto \frac{1}{L_R} \left(\frac{2\gamma^2}{1+2\gamma^2} \right)^{|\ell|} \left[\xi^{|\ell|+1} \Phi_\ell^{L_R, \gamma} - \Phi_\ell^{0, \gamma} \right]. \quad (3.6)$$

We note that the first term in brackets corresponds to that obtained previously [179], specialized to equal signal and idler widths and $p = 0$ modes. Here the function $\Phi_\ell^{L_R, \gamma}$ is the Lerch transcendent function of order $(1, |\ell| + 1)$ and argument $-2\gamma^2 \xi$ [271]:

$$\Phi_\ell^{L_R, \gamma} = \Phi(-2\gamma^2 \xi, 1, |\ell| + 1), \quad (3.7a)$$

$$\xi = \frac{i + L_R}{i - 2\gamma^2 L_R}. \quad (3.7b)$$

Note that $\xi = 1$ for $L_R = 0$. Once L_R and γ are specified, the amplitudes C_ℓ are to be used in the definition of $K(\{P_\ell\})$, in order to calculate the measurement bandwidth. The dependence of the projection amplitudes on a transcendent function makes further analytical calculation difficult, and a numerical approach has to be employed. However, as the tails of the distribution of projection probabilities have a slow decay and therefore an effect on the width even at high $|\ell|$, the numerical approach is slow, if an accurate result is sought.

3.1.2 Geometrical argument

In this section we find upper and lower bounds for the generated and measured OAM values. The measurement bandwidth that we calculate from such bounds matches the analytic result of the previous section, and therefore allows us to avoid a numerical calculation of the distribution of projection probabilities.

The phase-matching efficiency of the down-conversion process depends upon the axial mismatch Δk_z in wave vectors of the pump, signal and idler fields, and it is given by $\text{sinc}^2(L\Delta k_z/2)$. When optimized for degenerate, near-collinear phase-matching, the signal and idler output is obtained over a narrow range of

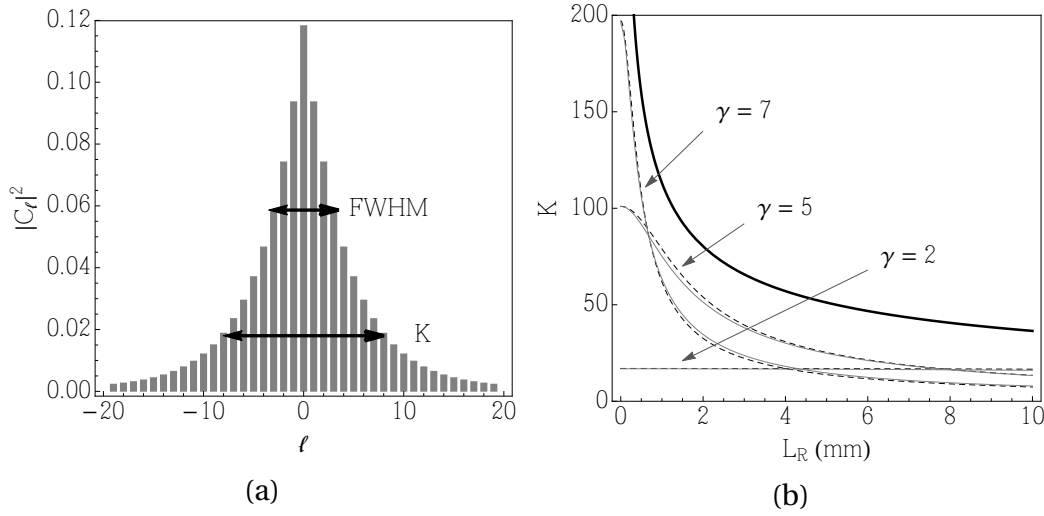


Figure 3.1: (a) An example of a distribution of $|C_\ell|^2$ for $L_R = 1$ mm and $\gamma = 2$, obtained by calculating numerically the projection amplitudes between $\ell = -20$ and $\ell = 20$. The FWHM and the measurement bandwidth K are shown. Note that K exceeds the FWHM by about 2.3 times, giving an effective mode number of about 16 in this case. (b) The thick line (uppermost) is the generation bandwidth defined in eq. (3.12), the solid grey curves are calculated from our analytical treatment (considering the interval from $\ell = -100$ to $\ell = 100$), and the dashed grey curves are the result of our geometrical argument, eq. (3.20).

opening angles, α , for which $L\Delta k_z \lesssim \pi$. With reference to fig. 2.2b, for small δ (which corresponds to being near to collinearity) we can write

$$\Delta k_z \simeq \frac{\delta^2 k_p}{2}. \quad (3.8)$$

It follows, therefore, that the allowed values of α are bounded from above:

$$\delta^2 \lesssim \frac{2\pi}{k_p L}. \quad (3.9)$$

For Laguerre-Gaussian modes in the paraxial regime, we can define an effective local wave vector associated with the gradient of the phase. The helical form of the wavefronts gives rise to an angular spreading of these such that at a distance r from the mode axis, the angular spread is $\beta = \ell / kr$, which can be interpreted as the local spreading angle from the optical axis [201]. The natural restriction on α imposed by the phase matching therefore sets a limit $\beta \lesssim \delta$ on the efficiency of

production of the OAM-carrying beams, imposing a restriction on the generated OAM bandwidth. Such restriction is a natural consequence of the fact that a generated mode cannot be more divergent than the down-conversion cone. The relation $\beta \lesssim \delta$, using the definitions and bounds given above for β and δ , can be rewritten as

$$\ell \lesssim r \sqrt{\frac{\pi k_p}{2L}}, \quad (3.10)$$

where we have made the approximation that $k_{s,i} \simeq k_p/2$. This relation is the starting point to calculate the generation bandwidth and for the analysis in the far field of the image plane of the crystal.

Generation bandwidth The beam size can be no larger than that of the pump beam, i.e. $r \lesssim w_p$. Applying this bound to (3.10), we obtain an upper bound for the generated OAM value:

$$\ell_g \lesssim w_p \sqrt{\frac{\pi k_p}{2L}} = \sqrt{\frac{\pi}{L_R}}. \quad (3.11)$$

It follows that the generation bandwidth is:

$$K_g = 1 + 2\sqrt{\frac{\pi}{L_R}}. \quad (3.12)$$

This number represents the effective number of entangled OAM modes generated by the source obtained by removing the $p = 0$ restriction (as we are applying such restriction only to the measurement bandwidth). Equivalently, it can be thought of as the bandwidth obtained by removing the restriction on γ , i.e. if one does detect $p = 0$, but with any γ . This way of thinking about K_g can be helpful, as it relates to a measurement scheme. The relation between K_g and the overall Schmidt number K or its azimuthal part K_{az} is not straightforward, because K_g can be thought of in terms of a measurement with any value of γ [262].

Image-plane bandwidth To calculate the measurement bandwidth we need to consider the overlap of the generated field with the detection modes in the image

plane of the crystal and in its far field. Intuitively, a detection system which has a good overlap in the image plane, but that detects light that only comes from a narrow spread of directions, would restrict the measured bandwidth. A similar restriction would also occur for one that has a good overlap with the typical incoming angles of LG beams, but that has a poor overlap with the intensity in the image plane. It is clear that, in order to optimize a detection system, both these quantities have to be taken into account.

To calculate the overlap in the image plane it suffices to note that a $p = 0$ Laguerre-Gaussian mode with OAM number ℓ and width w has its maximum intensity at a radius

$$r = w\sqrt{\frac{\ell}{2}}. \quad (3.13)$$

For efficient conversion of pump to signal and idler we require that the pump, signal and idler beams should all overlap, giving a restriction on the maximum size of the down-converted beams ($r_{s,i} \lesssim w_p$) and hence an upper bound to the value of OAM in the plane of the crystal corresponding to

$$r_{s,i} = w_{s,i}\sqrt{\frac{\ell}{2}} \lesssim w_p. \quad (3.14)$$

In terms of γ , this gives an upper bound on the value of the OAM in the plane of the crystal:

$$\ell_{\text{IP}} \lesssim 2\gamma^2 \quad (3.15)$$

and hence an image-plane bandwidth

$$K_{\text{IP}} = 1 + 4\gamma^2. \quad (3.16)$$

Far-field bandwidth It is clear that in the far field of the plane of the crystal, instead of a real space argument, we need to use the angular relationship $\beta \lesssim \delta$, expressed in eq. (3.10), where we apply the restriction for the maximum width

of the detection modes given in (3.14):

$$\ell \lesssim w_{s,i} \sqrt{\frac{\ell}{2}} \sqrt{\frac{\pi k_p}{2L}}. \quad (3.17)$$

From which, replacing $w_{s,i}$ with w_p/γ , we obtain an upper bound of the value of the OAM in the far field of the plane of the crystal:

$$\ell_{\text{FF}} \lesssim \frac{\pi}{2\gamma^2 L_R} \quad (3.18)$$

and therefore a far-field bandwidth

$$K_{\text{FF}} = 1 + \frac{\pi}{\gamma^2 L_R}. \quad (3.19)$$

Measurement bandwidth If K_{IP} and K_{FF} are very different from each other, the resulting measurement bandwidth is given by the smaller of the two. For cases where the bandwidths are similar it is sensible to combine them. The convolution of two normal distributions of widths σ and σ' gives a normal distribution of width $(\sigma^{-2} + (\sigma')^{-2})^{-1/2}$. Similarly, we can get an estimate of the total measurement bandwidth by considering the convolution of two normal distributions of widths K_{IP} and K_{FF} . The bandwidth of the resulting distribution is then

$$K = (K_{\text{IP}}^{-2} + K_{\text{FF}}^{-2})^{-1/2} = \left((1 + 4\gamma^2)^{-2} + \left(1 + \frac{\pi}{\gamma^2 L_2} \right)^{-2} \right)^{-1/2}. \quad (3.20)$$

3.1.3 Optimization of orbital angular momentum bandwidths

For a comparison between the analytic and geometrical arguments, we calculated the width of the distribution given by the modulus squared of the coefficients in (3.6) and compared it to (3.20). Fig. 3.1b shows the two bandwidths as functions of L_R for $\gamma = 2$, $\gamma = 5$ and $\gamma = 7$. Note that, in order to achieve high-dimensional entanglement, the crystal length should be a small fraction of the Rayleigh range.

We see that the geometrical argument is in excellent agreement with the numerical evaluation of the analytical result. The effect of increasing γ yields a higher measurement bandwidth for very small values of L_R . For large enough values of γ and for fixed L_R , however, the measurement bandwidth eventually drops, reaching a maximum value for a particular crystal length. Under all conditions the measurement bandwidth never reaches the generation bandwidth, because we are restricting the measurement to modes with $p = 0$. Note, however, that the full generation bandwidth does not arise explicitly from additional values of the OAM but rather from entanglement in the radial quantum number p .

Differentiation of eq. (3.20) with respect to the crystal length gives an estimate of the value of γ corresponding to the highest measurement bandwidth for a given L_R . From this we find:

$$\gamma_{\text{opt}} \simeq \sqrt[4]{\frac{\pi}{4L_R}}. \quad (3.21)$$

It is worth noting that, for such value of γ , we have that $K_{\text{IP}} = K_{\text{FF}} = K_g$. Therefore, in the optimal case we have $K = K_g/\sqrt{2}$.

We define short crystal lengths as $L_R \ll \pi/4\gamma^4$, for which the generation bandwidth is large, meaning that the measurement bandwidth is dominated by the image plane overlap of the detection modes with the pump. This gives a measurement bandwidth of

$$K \simeq K_{\text{IP}} = 1 + 4\gamma^2. \quad (3.22)$$

Note that this short crystal limit is characterized by K being independent from the crystal length. In fact, it can be seen in fig. 3.1b that the leftmost part of the measurement bandwidth curves is flat¹, and that the range of values of L_R over which they remain flat is inversely proportional to γ^4 . For much longer crystals, $L_R \gg \pi/4\gamma^4$, the measurement bandwidth, as modified by the limiting

¹This is not immediately apparent in the plot for $\gamma = 7$, but the slope of eq. (3.20) near the origin is zero for any γ .

overlap in the far field, becomes dominant, giving

$$K \simeq K_{\text{FF}} = 1 + \frac{\pi}{L_R \gamma^2}. \quad (3.23)$$

For each choice of L_R there is always an optimal value of γ that maximizes K , and it corresponds to the optimal value given in (3.21). It is not an easy matter to determine the requisite parameters for existing experiments. The experiments here presented, however, correspond to values of γ in the range 1.5 up to about 4. In order to achieve higher degrees of entanglement in OAM, corresponding to larger Schmidt numbers, it appears to be desirable to increase the value of γ .

3.1.4 Optical étendue and dimensionality

A simple geometrical argument can elucidate why the spiral spectrum widens as we tune the phase matching. This involves the concept of the optical étendue $E = A\Omega$, where A is the near-field beam area and Ω is the solid angle subtended by the beam in the far field [262, 174]. In the treatment of noise in laser amplifiers, the étendue normalized with respect to the wavelength λ , E/λ^2 , is the number of transverse modes that can be supported by the system. The étendue E acts as a measure of the number of quantum states in a beam [174, 281]. It is more often invoked in the discussion of light collection, but it is equally applicable in the case of SPDC where light is instead being emitted. Regardless of the phase matching, A is the same in our experiment: the SLMs are in the near field of a particular plane in the crystal and minute changes to crystal orientation (typically $1/20$ of a degree) do not change the image on the SLMs. However, this changes the far-field opening angle: as Ω increases for $\alpha = -2.2$, the number of transverse (both azimuthal and radial) modes emitted increases correspondingly.

In setting up a SPDC experiment, this has important practical implications. One should ensure that the detection étendue is greater than the generation étendue to maximize the overlap between the pump and detection modes. Using the Klyshko picture as a guide, where the detected signal (or idler) mode is back-propagated to the crystal, reflected off the crystal, and propagated to the other

detector [150], the overlap is maximized by keeping all corresponding far-field solid angles and near-field beam diameters in the signal and idler arms the same. The reason we use two lenses to image the crystal onto the SLMs instead of one is to match the far-field angles in both arms, thus acting as an effective detection system.

3.2 Increasing the spiral bandwidth in parametric down-conversion

We measured both OAM and angle correlations for two different phase-matching conditions. To measure OAM, we encoded forked diffraction gratings of topological charge ℓ_s on one SLM and ℓ_i on the other. These holograms transform the incoming field to a fundamental mode, which is the only mode that can be coupled to the fibres [172]. Since we were working in the collinear to near-collinear regime, OAM was conserved in our SPDC system, hence we expected the OAM of the signal and idler photon to be anticorrelated, i.e. the coincidence count was high only when $\ell_s = -\ell_i$ [196]. Ideally, to measure correlations in angular position, we encoded angular slits of width $\delta\phi$ centred at angle ϕ in both SLMs and rotated one with respect to the other, expecting high coincidence counts when the two slits were aligned [161].

Because the angle and OAM are Fourier related [139], a wide spiral bandwidth means a correspondingly narrow angular correlation that should be measured with a narrow angular slit. This presents a limitation in practice because a narrow angular slit means fewer counts, which are difficult to discern against the background. We solved this problem by using not one, but four narrow slits (7° wide, almost twice as narrow as what was used previously [161]), thereby enabling us to still measure tight angular correlations without sacrificing counts. With one four-slit pattern oriented at ϕ_s and another oriented at ϕ_i , we measured the coincidences as a function of $\Delta\phi = \phi_s - \phi_i$. As a result of having four slits, our angular position coincidence curves have more than one maximum (insets of fig. 3.2c and 3.2d), from which the width of the angular correlation

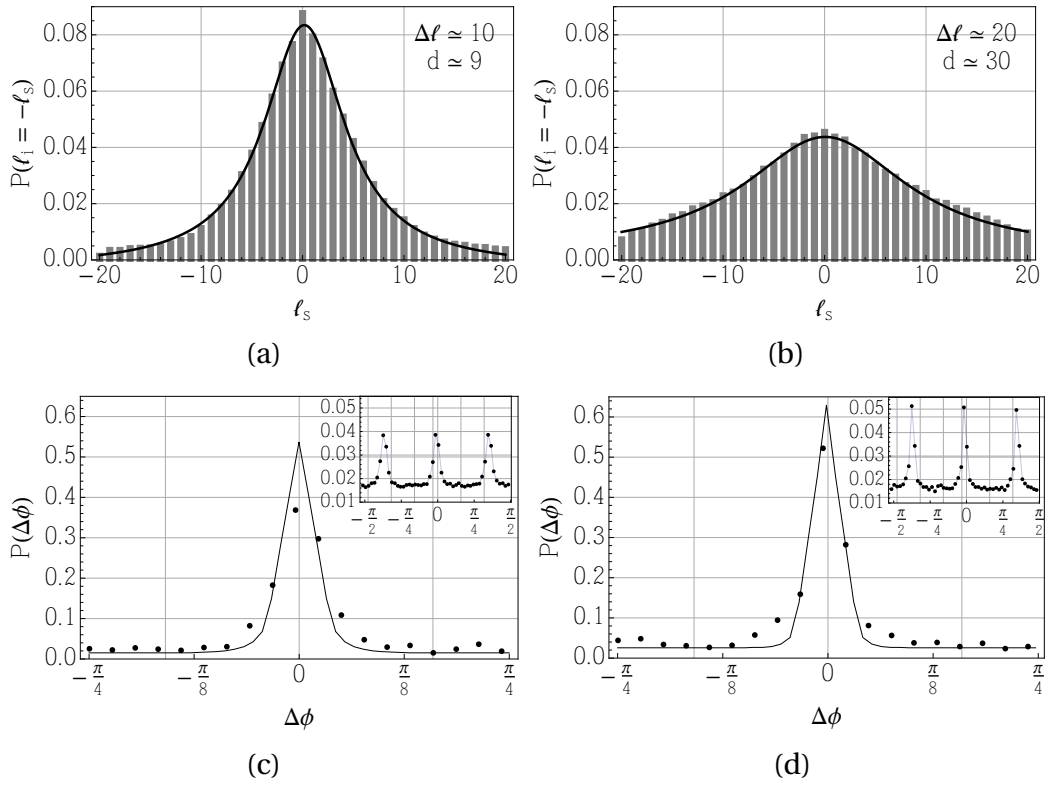


Figure 3.2: OAM and angular position measurements. (a) For collinear phase-matching, with $\alpha = 0$, the measured spiral spectrum has a half-width of $\Delta\ell \approx 10$, with $d = 9$. (c) The central maximum (renormalized and background-subtracted) of the angular position correlation measurement when the signal and idler slits have a relative orientation of $\Delta\phi$, has a half-width of 12° . The inset shows the other maxima from the four-slit pattern. (b) For noncollinear phase-matching conditions, $\alpha = -2.2$, the measurement spiral bandwidth is wider, with $\Delta\ell \approx 20$, $d \approx 30$. (d) The angular position correlation is narrower, with a half-width of 8° . Dots and bars are experimental results, solid black lines are fits that demonstrate consistency with a Fourier relation between OAM and angle.

could be derived.

3.2.1 Experimental results

Orbital angular momentum and angular position measurements for two different phase-matching conditions are shown in fig. 3.2. We subtracted the

accidental counts, estimated as

$$A = S \times I \times \Delta t, \quad (3.24)$$

where S and I are the single channel counts of the signal and idler arms, respectively, and $\Delta t = 10\text{ns}$ is the coincidence timing window. We defined the measurement spiral bandwidth $\Delta\ell$ as the full width at half maximum of the measured spiral spectrum. For collinear phase matching $\alpha = 0$ in eq. (3.1) (fig. 2.3a), we found $\Delta\ell \simeq 10$ (fig. 3.2a) and the corresponding half-width of the central peak in the angular position coincidence curve was 12° (fig. 3.2c).

With the addition of an on-axis phase mismatch $\alpha = -2.2$ in eq. (3.1), the opening angle of the spot was then slightly increased (to $\simeq 1.1^\circ$ from the propagation axis to the first minimum, compared to 0.9° for $\alpha = 0$). There is a central dip in the corresponding intensity distribution (fig. 2.3b). We found $\Delta\ell \simeq 20$ (fig. 3.2b). The half-width of the corresponding angular position correlation was narrower, as expected from the Fourier relationship [139, 135], and it was found equal to 8° . The solid black lines in fig. 3.2a and 3.2b are Lorentzian and are empirical fits to our data. Using these fits, we were able to calculate the expected angular correlation from the Fourier relation, with the added consideration that our angular masks have a finite slit width (solid line in fig. 3.2c and 3.2d). Angular position measurements are very sensitive to alignment, and we attribute the imperfect fits in fig. 3.2c and 3.2d to this.

We focussed on the OAM measurements and derived the mutual information H . This can be calculated from the probabilities

$$H = -\sum_{\ell_s} p(\ell_s) \log_2 p(\ell_s) - \sum_{\ell_i} p(\ell_i) \log_2 p(\ell_i) + \sum_{\ell_s, \ell_i} p(\ell_s, \ell_i) \log_2 p(\ell_s, \ell_i) \quad (3.25)$$

where $p(\ell_s, \ell_i)$ is the probability of measuring ℓ_s and ℓ_i . We define

$$p(\ell_s) = \sum_{\ell_i} p(\ell_s, \ell_i) \quad (3.26)$$

as the probability of measuring ℓ_s , and

$$p(\ell_i) = \sum_{\ell_s} p(\ell_s, \ell_i) \quad (3.27)$$

is the probability of measuring ℓ_i . For $\phi = 0$, the mutual information was 3.17 ± 0.60 bits/photon, corresponding to a dimensionality $d = 2^H \simeq 9$. Adjusting the phase matching to $\alpha = -2.2$ results in a mutual information of 4.94 ± 1.03 bits/photon, corresponding to $d \simeq 30$, twice the measurement range of results attained in previous papers [161].

We remark that, apart from being detection limited, we have also defined our dimensionality stringently by calculating it from the mutual information. In this way we are sensitive to the level of noise and crosstalk even for measurements where $\ell_s \neq \ell_i$, which becomes more apparent with higher-valued OAM states. As such, we expect our dimensionality to be less than the Schmidt number K for our system. We have independently measured K for our system via sector phase plates and found these greater than our measured d (chap. 4). We obtained $K = 35 \pm 2$ for $\phi = 0$ and $K = 49 \pm 2$ for $\phi = -2.2$ [109]. The values of K can also be estimated from [159], which gives 35 for $\phi = 0$ and 43 for $\phi = -2.2$ with our experimental parameters.

We also remark that K , being defined in terms of just probabilities, does not provide any information about the shape of the spiral spectrum. A full decomposition in terms of OAM modes has been treated elsewhere, although not for the noncollinear case [179, 279]. The OAM spectrum, although not Lorentzian, is Lorentzian-like in shape and this has motivated us to use a Lorentzian fit [81, 279]. Theoretical fits for our results and hence estimates for $\Delta\ell$ can only be obtained from a full model of our experiment, such as one based on the Klyshko back-propagation picture [150].

3.2.2 Angular two-photon interference and entanglement measures

Measuring entanglement in d dimensions is not as straightforward as measuring the entanglement of two-dimensional systems. We can violate a Bell inequality for higher dimensions, as implemented in [81], but this is difficult for $d \simeq 30$ because the intensity masking reduces the count rates considerably. Instead, we employ the entanglement measure

$$E = \sum_{\ell_s, \ell_i} p(\ell_s, \ell_i) - p(\ell_s)p(\ell_i) \quad (3.28)$$

proposed in [72], with , similar to the I -concurrence [126, 275, 276] or Rényi-2 entropy [223, 129], apart from numerical factors. Here E is zero for separable states, based on the underlying assumption that the correlations considered are non-classical. For our results, we calculated values of 0.8101 ± 0.01 and 0.8097 ± 0.02 for $\phi = 0$ and -2.2 , respectively, indicating that our two-photon OAM states are non-factorable and therefore entangled. The presence of crosstalk in the higher OAM modes prevents us from getting a significantly higher entanglement measure for $\phi = -2.2$, as one might expect.

Furthermore, we exploited the Fourier relationship, or complementarity between OAM and angle [139, 24], to quantify the entanglement in the angular position basis. When a photon passes through an angular aperture we can observe interference in the OAM distribution of the signal (or idler) field, the modulation of which depends on the spiral spectrum of the photons [140]. We can encode angular two-slit patterns on the SLMs and measure the resulting OAM interference when SLM₁ (idler) is set to measure $\ell_i = 0$ and the value of ℓ_s on SLM₂ is scanned from $-\ell_{\max} = -20$ to ℓ_{\max} . It has been shown that the visibility of the resulting interference pattern is the same as the concurrence (ranging from 0 to 1, 1 being the maximally entangled case) of the two-qubit density matrix written in the angular position basis [140, 275]. We verified strong angular position correlations, as shown in fig. 3.3a and 3.3b, where we measured the coincidences when encoding only one slit (of width 18°) on each SLM for each set of phase-matching conditions. As expected, we recorded appreciable

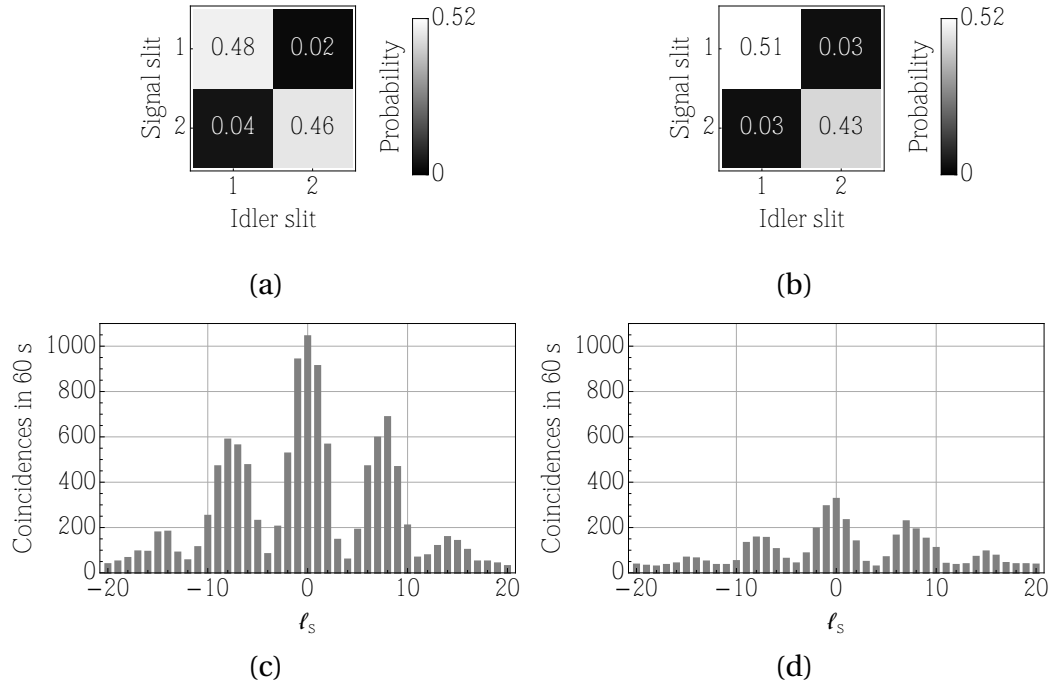


Figure 3.3: We encoded two-slit patterns (width 18° , separated by 45°) on top of the forked holograms of SLM_1 and SLM_2 . With only one slit in each SLM (1 or 2), we verified the strong angular position correlation. (a) For $\alpha = 0$ we observed high coincidence rates only when both SLMs had slits with the same angular position. (c) The measured concurrence is 0.96. In (b) similar angular position correlations for $\alpha = -2.2$ are shown and, in 3.3d, fringes for a concurrence of 0.90.

coincidences only when we encoded the same slit positions for both SLMs. Ideally, the diagonals should be 0.5, but, due to imperfect alignment, we still got small off-diagonal probabilities.

The interference of the two-slit patterns with their corresponding OAM values leads to a modulation in the coincidences that can be measured in the OAM basis. Fig. 3.3c and 3.3d show the coincidences for $\alpha = 0$ and $\alpha = -2.2$. The measured concurrence is 0.96 ± 0.07 for $\alpha = 0$ and 0.90 ± 0.12 for $\alpha = -2.2$, demonstrating that we indeed have entangled angular qubit states for both phase-matching conditions. We remark that the decrease in the concurrence value is counterintuitive considering that the latter case corresponds to a greater number of OAM modes. This may be due to imperfect alignment, as measurements in the angular position basis are more sensitive to this. We also emphasize

that the measurements presented in fig. 3.3a and 3.3b (strong angular position correlation) and fig. 3.3c and 3.3d (interference in the OAM basis) can be produced simultaneously only by OAM-angular position entangled sources. The good correlation quantifiers in both OAM and angular position for both phase-matching conditions are a signature of genuine two-photon d -dimensional entanglement, where d is tunable.

In conclusion, we have demonstrated a system where we can generate and detect high-dimensional two-photon entanglement. We have characterized the entanglement in terms of the mutual information shared by the entangled photon pairs. Minute changes to the angular orientation of a bulk BBO crystal ($\approx 1/20$ of a degree) widens the OAM measurement spiral spectrum and narrows the angular position correlation, as a consequence of phase matching in SPDC. We have designed our detection system guided by the concept of the optical étendue and we have achieved as much as 4.94 bits/photon, implying 30-dimensional OAM entanglement. We can obtain a relatively flat spectrum for a few OAM modes, which could allow future protocols to forego entanglement concentration. We note that our measurements, although in a high-dimensional space, are still dichotomous, in contrast to a polarization beam splitter that sorts the two possible polarization states into two possible outcomes. However, a mode sorter that separates all of the d orthogonal OAM states has been recently developed [43]. Coupled with the generation and detection geometry that we have characterized in this work, this points to the possibility of new experiments such as detection loophole-free Bell test experiments [266], superdense coding [203, 28] and multivalued quantum walks [239] where a higher-dimensional space is desirable.

3.3 Pump shaping

Besides the choice of crystal and the geometry of the SPDC system, other methods allow partial control of the orbital angular momentum spectrum or, in a similar manner, the degree of entanglement of the OAM-correlated photon pairs. One strategy is based on the manipulation of the spatial profile of the pump

beam impinging on the nonlinear crystal. More complicated spatial profiles that include, for instance, a superposition of several OAM eigenmodes other than the fundamental Gaussian mode affect the quantum state of the photon pairs generated in the down-conversion process [256]. An alternative method involves an appropriate preparation of the down-conversion crystal, adopting precise transverse quasi-phase-matching conditions [254]. The manipulation of the amplitudes of the different OAM components of the down-converted state can also be in part achieved after the crystal, using appropriate filtering methods [264].

For some applications and protocols that rely on maximally entangled states, generating OAM-entangled states and controlled superpositions of OAM states can be of critical importance. The SPDC process, however, does not naturally produce maximally entangled states in arbitrary subspaces of OAM. To overcome this problem, it is possible to take advantage of some of the properties of the nonlinear process. The conservation of OAM in SPDC guarantees that, for each photon measured in a given autostate of OAM with $+\ell$, a second photon exists with $-\ell$. The probability of producing a pair of photons in a given OAM state depends on the superposition of the down-converted modes with the pump beam. If the pump beam is Gaussian, photons with lower OAM content $|\ell|$ will be detected more frequently than those in higher-order modes (fig. 3.1a).

Exploring the higher dimensions afforded by OAM then generally involves the design of holograms able to measure superpositions of different OAM states [157, 265, 265, 229]. However, since SPDC is very much dependent on the pump beam [279, 181], as mentioned one can also explore the high-dimensional OAM state space by engineering the pump. Shaping the pump to prepare high-dimensional entangled OAM states with more complex modes has been proposed [180, 256], although these have not previously been implemented experimentally. For this purpose, we employed a non-Gaussian pump beam for SPDC and analysed how the OAM and angle correlations changed as a result.

Within SPDC, a pump beam is usually approximated as a plane wave incident on a nonlinear crystal, which results in the emission of two correlated photons in definite directions. The bulk of the studies in SPDC has concentrated on manipulating these two outgoing photons by letting them pass through polar-

izers, slits, holograms, and other optical components, to observe various desired quantum effects [172, 162, 136, 16, 17, 246]. Manipulating the pump field is also an interesting enterprise, as the fields generated in SPDC are strongly related to the pump field; this has been investigated theoretically and experimentally [172, 279, 181]. Phase matching allows the amplitude and phase structure of the pump to be transferred to the two-photon field, and fourth-order images related to the aperture in front of the pump can be formed by the down-converted beams [181]. Focusing the pump beam in front of the crystal leads to two-photon geometric-optics effects wherein the crystal acts like a spherical mirror in the formation of the fourth-order images [208].

The shape of the pump is of consequence to correlations in the OAM and the conjugate variable, angular position, in both the signal and idler fields. The transfer of the plane-wave spectrum of the pump to the two-photon field leads to conservation of OAM in both stimulated and spontaneous parametric down-conversion [66, 175, 91, 268]. Thus, for near-collinear SPDC [268], the selection rule $\ell_p = \ell_s + \ell_i$ holds, where $\ell_p \hbar$ is the OAM per photon of the pump beam and $\ell_s \hbar$ and $\ell_i \hbar$ are the OAM contents of the modes into which the signal and idler photons are projected [268, 196, 197]. This has been supported by coincidence measurements in SPDC, wherein the crystal is pumped with Laguerre-Gaussian beams of varying OAM [172, 268]. The entangled two-photon state generated in this case is

$$|\psi\rangle = \sum_{\ell=-\infty}^{\infty} c_{\ell} |\ell_p - \ell\rangle |\ell\rangle. \quad (3.29)$$

3.3.1 SPDC with a phase-flipped Gaussian mode as pump

It is possible to generate other states, such as maximally entangled states with only four modes (in contrast to the infinite OAM spectrum of eq. (3.29)), by pumping the crystal with a suitable superposition of OAM modes [256], containing a number of phase singularities. This entails the modulation of both the phase and intensity of the pump, and has yet to be achieved experimen-

ℓ	$\langle \text{LG}_{\ell,0} u_{f,0} \rangle$
± 5	$\frac{1}{8} \sqrt{\frac{3}{10\pi}} = 0.0386$
± 3	$\frac{-1}{2} \sqrt{\frac{1}{6\pi}} = -0.1151$
± 1	$\sqrt{\frac{1}{\pi}} = 0.5642$
0	0

Table 3.1: Decomposition of the phase-flipped pump mode in terms of $\text{LG}_{\ell p}$ (with $p = 0$).

tally. The first step towards the implementation of such schemes is to have an element which will efficiently convert the fundamental mode of a pump laser to the desired mode for SPDC. Several experiments [172, 268] have performed this mode conversion with cylindrical lenses, holograms or with a cover slip [187, 115]. Holograms, when encoded in a spatial light modulators (SLM) are flexible and make possible complicated pump shapes, but they are less efficient than other converters, with an efficiency of about 40%–50% [78].

Simple pump shapes could instead be implemented with simple mode converters. For instance, HG modes can be created by placing one to two wires inside a laser cavity [244]. Not having access to the laser cavity of our pump laser, we instead used a cover slip placed in the pump beam path to introduce a π -phase shift in half of the area of the Gaussian output of the pump beam before this reaches the crystal. This imprints a phase flip to one half of the beam, hence the name ‘flipped mode’ [85]. Following [85], the flipped mode $u_{f,0}$ is the fundamental Gaussian mode with a phase flip at $x = 0$. This can be expressed as an infinite sum of odd Hermite–Gaussian (HG) modes $u_{2n+1}(x)$

$$u_{f,0} = \sum_{n=0}^{\infty} c_{2n+1} u_{2n+1}(x) \quad (3.30)$$

where

$$c_{2n+1} = \frac{(-1)^n (2n)!}{n! \sqrt{\pi 2^{2n-1} (2n+1)!}} \quad (3.31)$$

giving $\sqrt{2/\pi} \approx 0.80$ as the contribution of the first-order HG_{10} mode. Since the

LG modes form a convenient basis for OAM-carrying beams, it is instructive to express $u_{f,0}$ in terms of Laguerre polynomials L_k^j [147, 1]

$$u_{f,0} = \sum_{n=0}^{\infty} \sum_{p=0}^n a_{np} \exp \left[-\left(\frac{r}{\omega}\right)^2 \right] \left(\frac{\sqrt{2}r}{\omega}\right)^{|2(n-p)+1|} L_p^{2(n-p)+1} \left(2\frac{r}{\omega}\right) \quad (3.32)$$

$$\times \exp [i(2(n-p)+1)] + \exp [-i(2(n-p)+1)]$$

where $a_{n,p}$ is

$$a_{n,p} = (-1)^{n+p} \sqrt{\frac{8}{\pi}} \frac{(2n)!}{(2n+1)!} \frac{(n+1/2)!}{2p!} \frac{2p!}{\pi(p+(2(n-p)+1))!}. \quad (3.33)$$

Hence, only the odd LG modes contribute. The decomposition in terms of the $LG_{\ell p}$ modes for $p=0$ is given in tab. 3.1.

The flipped mode has been used in SPDC to produce singlet states [187], to demonstrate multimode Hong–Ou–Mandel interference and to generalize genuine non-Gaussian entanglement [267, 115]. Since the combination of OAM states $|1\rangle$ and $|-1\rangle$ makes the most significant contribution to the flipped mode, in contrast to the usual Gaussian pump which is in the OAM state $|0\rangle$, we expect different OAM and angle correlations from that in [161]. Specifically, we expect coincidences when $\ell_s + \ell_i$ is odd with the strongest correlations occurring when $\ell_s + \ell_i = \pm 1$.

Just as there is a Fourier relationship between position and linear momentum, there also exists a Fourier relationship between OAM and angle [139]. This allows us to determine the correlations in the angular position basis given that we have knowledge of the OAM components of the entangled photons.

3.3.2 Experiment and results

Our SPDC set-up (fig. 2.5) consisted of a mode-locked ultraviolet (UV) pump source at 355 nm with 120 MHz repetition rate. A cover slip was attached to a tip-tilt mount to control the phase introduced into the pump, and placed on a translation stage positioned such that it covered half of the UV beam. The output of the laser was collimated by a telescope and directed onto a 5 mm long

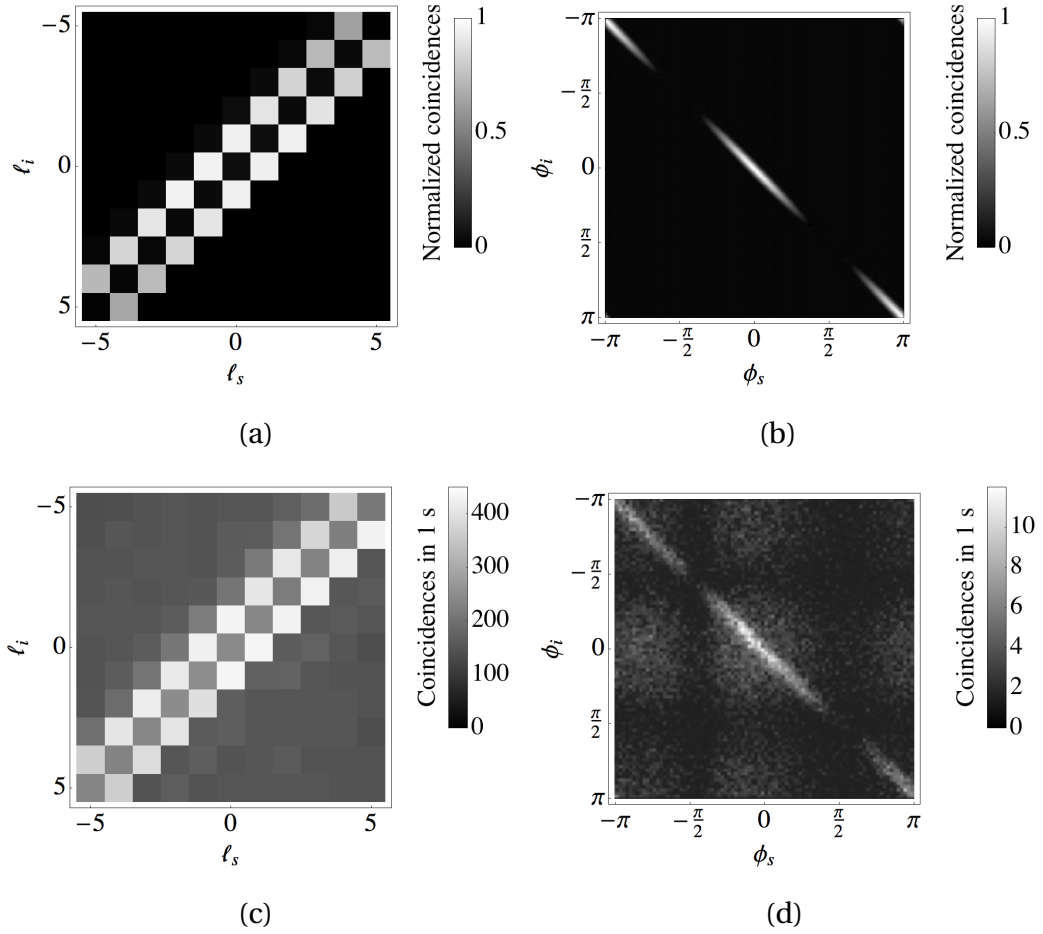


Figure 3.4: OAM (ℓ_s, ℓ_i) and angular position (ϕ_s, ϕ_i) correlations for a phase-flipped Gaussian pump. (a) Since the $\ell = \pm 1$ components make the largest contribution to the pump mode, we expect to see coincidence maxima for $\ell_s + \ell_i = \pm 1$. (b) The angular position correlations also reflect the shape of the pump, and can be obtained via the Fourier relationship between OAM and angular position. The coincidence rate is high along the diagonal, when $\phi_s = \phi_i$, with minima corresponding to the angular position of the phase discontinuity in the pump. The experimental results shown in (c) and (d) do not include any background subtraction.

BBO crystal, cut for degenerate type-I, collinear SPDC. As in the previous experiment, the front plane of the crystal was imaged onto two separate SLMs, which determined the state into which the photon was to be projected. Both SLMs were re-imaged, through 10 nm wide interference filters, onto the input facets of single mode optical fibres coupled to single-photon avalanche photodiodes.

The coincidence rate was monitored from the output of the photodiodes by a coincidence counting card with a gate time of 10 ns.

To measure OAM, each SLM displayed a hologram with a fork dislocation of order ℓ_s and ℓ_i corresponding to the OAM states $|\ell_s\rangle$ and $|\ell_i\rangle$. The pump beam consisted of superpositions of odd-valued OAM states, with $|1\rangle$ and $|-1\rangle$ making the largest contribution. Hence following the selection rule for the conservation of OAM in SPDC, we expect high coincidences when the sum of ℓ_s and ℓ_i is ± 1 , as shown in fig. 3.4a. We expect two diagonals symmetric about the main diagonal, in contrast to SPDC with a fundamental Gaussian pump, wherein only one main diagonal is present [161]. Fig. 3.4c shows the coincidences, as a function of ℓ_s and ℓ_i , obtained from the experiment. Apart from a uniform background (we did not perform any background subtraction in our results), and residual on-axis coincidences (due to the imperfect conversion of the pump laser output to a ‘flipped mode’) there is good qualitative agreement between the values in 3.4a and 3.4c, showing the transfer of the pump OAM spectrum to the entangled photons.

To measure angular position, we employed angular slits of width $\Delta\theta$, which were oriented at positions ϕ_s and ϕ_i in the signal and idler SLMs respectively (see fig. 3.4b). We can derive the expected angular position correlations from the Fourier relationship, by performing a Fourier transform on fig. 3.4a we obtain fig. 3.4b. Because the SLMs were at the image plane of the crystal, we expect the coincidences to be high for $\phi_s = \phi_i$. In addition, due to the shape of the pump, we see a modulation where coincidence minima correspond to an alignment of the slit with the phase discontinuity in the pump. Fig. 3.4d shows the experimental coincidence count as a function of the angular positions ϕ_s and ϕ_i . There is good qualitative agreement between figures 3.4b and 3.4d, apart from an almost uniform background.

We have shown the effect of the pump shape on OAM and angle correlations exhibited by photon pairs from spontaneous parametric down-conversion. We focussed on a particularly simple OAM superposition state, but more complicated modes are also possible with combinations of cover slips (for HG pump modes), specially fabricated components or programmable spatial light modulators. More complicated pump shapes such as the vortex pancakes suggested in

[256] can also be used for tailored entangled states. The correlations that arise result from the transfer of the OAM spectrum of the pump to the down-converted photon pairs, as manifested in the OAM correlation matrix. We showed a modulation in the angular position correlation that is consistent with the Fourier relationship between OAM and angle. The spatial structure of down-converted light is a rich playground to observe correlations in a variety of spatial modes, not just OAM. If efficiency is not a priority, the flexibility afforded by spatial light modulators can be introduced not just in the measurement, but also in the generation of entangled photons.

CHAPTER 4

Efficient determination of the dimensionality of bipartite OAM entanglement

The photon pairs generated by spontaneous parametric down-conversion (SPDC) in a nonlinear crystal are correlated in their various properties, some of which can exhibit high-dimensional entanglement. The orbital angular momentum (OAM) of light is one such property, associated with phase structures of the form $e^{i\ell\phi}$, where $\ell\hbar$ is the OAM carried by each photon [9]. As ℓ is an integer and is theoretically unbounded, OAM offers a natural discrete space for exploring high-dimensional entanglement [280]. In SPDC with a Gaussian pump (with $\ell = 0$), the spectrum of OAM correlations between the signal and idler photons is peaked at $\ell = 0$, with tails towards high $|\ell|$ values. As described in the previous chapters, the width and shape of the spectrum, and therefore the number of OAM modes that constitute the two-photon entangled state, can be engineered directly by manipulating the structure of the beam pumping the crystal [256, 279, 179] or by tuning the phase-matching conditions in SPDC [87].

It is necessary to distinguish between the entanglement of the high-dimen-

This chapter includes material previously published in the following paper:

- D. Giovannini, F. M. Miatto, J. Romero, S. M. Barnett, J. P. Woerdman and M. J. Padgett, “Determining the dimensionality of bipartite orbital-angular-momentum entanglement using multi-sector phase masks”, *New J. Phys.* 14(7), 073046 (2012)

sional OAM state generated by the SPDC process, whose dimensionality is described by the Schmidt number K [159], and that detected by the measurement stage of the system [215], with Shannon dimensionality M [216]. M is in fact dependent upon both the generated down-conversion OAM spectrum and the finite detection capability of our analysers. The latter is expressed in terms of the number of modes D that an analyser has access to. By knowing the relation between these three quantities, we can infer K after measuring M with an analyser characterized by a known D .

Determining the measured dimensionality M of tailored high-dimensional entangled states can be carried out by performing appropriate selective projective measurements [40]. One such set of measurements is based on pairs of binary multi-sector phase plates placed in the two arms of a down-conversion system, a method first proposed by Woerdman and co-workers [215]. Each plate has N azimuthal angular sectors, each of which introduces a π phase shift. The number and angular width of the sectors of the phase analysers placed in each of the signal and idler arms define the superposition of OAM eigenmodes in which the two-photon state produced by down-conversion is projected. By optimizing the binary phase profile of the phase analysers, it is possible to maximize the Shannon dimensionality D of the measurement apparatus, for any number of sectors N of the two plates.

By using angular phase analysers we infer the Schmidt number K , characterizing the effective number of azimuthal entangled OAM modes. In contrast to previous works, which used micromachined phase plates [214], we implement N -sector angular phase analysers using spatial light modulators (SLMs) [162]. Computer-controlled SLMs provide a fast, convenient and reliable way of producing holographic phase masks with arbitrary orientations and numbers of sectors, to be used in the measurement of the Shannon dimensionality of OAM entanglement. The use of multi-sector phase masks to probe high-dimensional states, as opposed to narrow single-sector analysers [161, 81], allows the measurements of tight angular correlations whilst maintaining high optical throughput.

4.1 Angular slits and phase masks

The angular measurement of a light field can be achieved by employing an angular slit. The idea behind this approach is the angular analog of a linear slit: a linear slit measures a field at one linear coordinate, with an uncertainty that depends on the width of the slit. An angular slit, on the other hand, measures a field at one angular coordinate with an uncertainty that depends on the angular width of the slit. As the angular position and orbital angular momentum form a pair of conjugate observables, the tighter the angular correlations, the larger the spread in the OAM observable [24, 103]. If one seeks high measurement accuracy, the angular slit has to be very narrow and, in turn, this means that much of the light is blocked, yielding the problem of a lower number of counts as the measurement uncertainty decreases.

A practiced solution to this problem is to employ phase-only masks, instead of amplitude masks. The design of the phase mask consists of an angular step plate, which is characterized by a number of sectors N and by a set of angles that describe the position and width of each sector [214]. Each alternate sector applies a π phase shift. The overall action of a phase plate of this kind is therefore to imprint an azimuth-dependent phase retardation and flip the phase of a light field in each π -phase sector, leaving the phase unchanged everywhere else. Note that the action of a phase plate does not affect the radial degree of freedom, as the design is radially invariant. This means that there is no coupling between different eigenmodes of the radial degree of freedom, which allows us to restrict ourselves to the azimuthal content of the measured state.

This effect can be described in terms of OAM. A plane wave is turned into a superposition of different OAM eigenstates. The range of OAM eigenstates of which the superposition consists depends on the number of sectors and on their relative positions and widths [214]. Such effect is analogous to the introduction of an amplitude mask, without the drawback of letting less and less light through as the angular uncertainty is decreased. We consider an angular state analyser composed of a multi-sector phase-only mask, a single-mode fibre and a detector. The projection state of this analyser is in general an extended superposition of OAM eigenmodes, that depends on the exact

number and distribution of the sectors, as well as the orientation of the phase mask. By rotating the phase mask about its centre, the analyser probes a larger-dimensional mode space [190, 215]. By producing phase masks with arbitrary numbers of sectors N with the use of SLMs, we are not constrained by limitations of the fabrication techniques, and can therefore probe the high-dimensional OAM state produced by an appropriately tuned SPDC source with analysers that have access to a comparable or larger number of modes.

4.2 Shannon dimensionality

We probe the two-photon state produced by down-conversion

$$|\psi\rangle = \sum_{\ell=-\infty}^{\infty} c_{\ell} |\ell\rangle_s |-\ell\rangle_i \quad (4.1)$$

described in the OAM basis, where $|\ell\rangle_s$ and $|\ell\rangle_i$ correspond to the states of the signal and idler photons respectively. By expressing the projection state associated with a phase-mask analyser oriented at an angle θ as the superposition

$$|A(\theta)\rangle = \sum_{\ell} \lambda_{\ell} |\ell\rangle e^{i\ell\theta}, \quad (4.2)$$

the coincidence probability for a pair of analysers A and B , oriented at θ and θ' respectively, is given by

$$P(\theta, \theta') = |\langle A(\theta), B(\theta') | \psi \rangle|^2, \quad (4.3)$$

where $\langle A(\theta), B(\theta') | = \langle A(\theta) | \otimes \langle B(\theta') |$. The coefficients $\gamma_{\ell} = |\langle \ell | A(0) \rangle|^2 = |\lambda_{\ell}|^2$ (with $\sum_{\ell} \gamma_{\ell} = 1$), defined by the profile of the N -sector phase masks, determine the respective OAM spectrum.

For an angular phase mask with phase profile $f(\phi - \theta)$, rotated by angle θ and with azimuthal coordinate ϕ , the projection mode corresponding to eq. (4.2)

is given by

$$A(\phi, \theta) = \frac{1}{\sqrt{2\pi}} e^{if(\phi-\theta)}. \quad (4.4)$$

From this form, the coefficients $\{\lambda_\ell\}$ of the OAM expansion in eq. (4.2) can be rewritten as Fourier coefficients of the phase mask profile:

$$\lambda_\ell = \frac{1}{\sqrt{2\pi}} \int_0^{2\pi} A(\phi, 0) e^{-i\ell\phi} d\phi. \quad (4.5)$$

The coupling strength $\gamma_\ell = |\lambda_\ell|^2$ can thus be obtained from the mode overlap between the corresponding mode and the projection mode $A(\phi, 0)$ [214].

The maximum number of modes D that can in principle be measured by each of such optimal N -sector masks can then be inferred from the theoretical distribution of eigenvalues γ_ℓ as

$$D = \frac{1}{\sum_{\ell=-\infty}^{\infty} \gamma_\ell^2}. \quad (4.6)$$

It is possible to design the distribution of $2N$ binary arc sectors of each N -sector phase mask in a way that maximizes the Shannon dimensionality D of the measured entanglement. Based on the numerical optimization results from [214], for each N we used the optimal arrangement of sectors that yields the largest D and, therefore, makes the largest number of modes accessible to the angular analyser.

In contrast, the Shannon dimensionality D of each N -sector mask used here was derived through a numerical model. The numerical model considered the distribution of the overlap between two identical N -sector masks within a two-dimensional region with a Gaussian profile, as the orientation θ' of one of the masks was rotated with respect to the other, θ . The maximum measurable dimensionality D for each optimal N -sector mask is shown in fig. 4.3. It was found that, for N at least up to 14, D increases approximately linearly with N . Given the expected peak-normalized correlation distribution $P(\theta - \theta')$ obtained from the numerical model, the Shannon dimensionality [215] can be directly

calculated as

$$D = \frac{2\pi}{\int_0^{2\pi} P(\theta - \theta') d(\theta - \theta')}, \quad (4.7)$$

where angle θ' is measured with respect to θ . We implemented multi-sector masks with a number N of sectors between 1 and 16, choosing one optimal arrangement of sectors, defined by $2N$ numerically obtained angles, for each N . The dimensionalities D obtained from both the numerical model previously described and the theoretical model, the latter obtained from the decomposition of each N -sector mask into eigenmodes γ_ℓ and the sum over the first thousand terms of each corresponding infinite series expansion [214], were found to differ by less than 2.5%.

4.3 Experimental determination of the effective dimensionality of bipartite OAM entanglement

4.3.1 Experimental set-up

Implementing phase-mask analysers using computer-controlled spatial light modulators allows for quick and effective measurement of the Schmidt number K of the entangled state produced by SPDC. No optical elements need to be fabricated, physically rotated or replaced when using a different multi-sector mask, as the measurement process simply involves displaying one of a set of different rotated N -sector holograms on the SLMs and performing coincidence detection.

A 5 mm-thick β -barium borate (BBO) nonlinear crystal cut for type-I collinear SPDC acted as our source of entangled photon pairs. The crystal was pumped by a 1 W UV laser to produce frequency-degenerate entangled photon pairs at 710 nm. The co-propagating signal and idler photons were separated by a non-polarizing beam splitter, and redirected to SLMs. The SLMs, onto which the crystal output face was imaged by a $2\times$ telescope, were encoded with N -

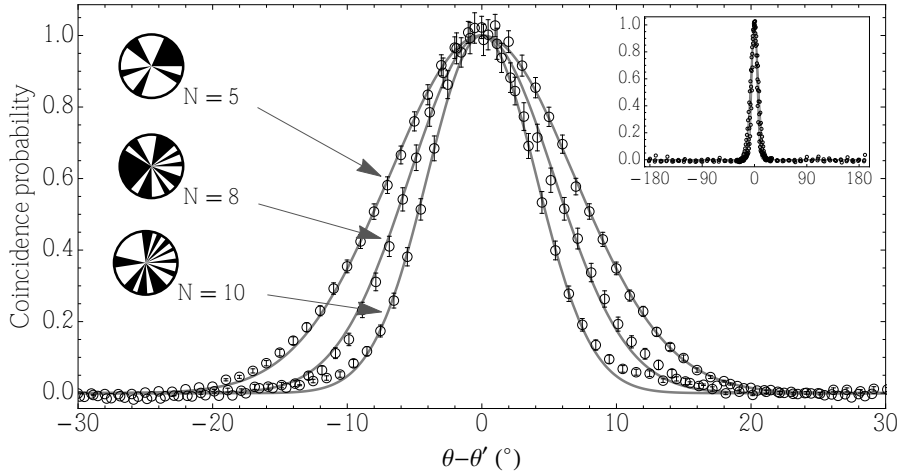


Figure 4.1: Typical best Gaussian fits of coincidence probability distributions $P(\theta - \theta')$ are shown for $N = 5, 8, 10$ and phase-matching parameter $\alpha = 0$. The inset shows the full $-180^\circ < \theta - \theta' < 180^\circ$ range used in the measurements, for the aforementioned values of N . White sectors correspond to a π phase shift, black sectors correspond to no phase shift. Background subtraction was performed by assessing the experimental accidental coincidences.

sector phase holograms. The SLMs were then imaged onto single-mode fibres (SMFs), which coupled the SLM output to single-photon photo-diode detectors whose output was routed to coincidence-counting electronics. The coincidence counting had a timing window of 10 ns. Narrow-band, 2 nm interference filters were placed in front of the detectors to ensure that the frequency spread of the detected down-converted fields was small compared to the central frequencies. SLMs introduce great flexibility in our measurements, but this comes at the price of an overall lower detection efficiency, as their diffraction efficiency is around 50%.

This detection configuration is insensitive to any overall phase factors. Therefore, while the conservation of OAM in the SPDC process would require placing mutually phase-conjugate N -sector phase masks in the detection arms (i.e., the 0 and π phase-shifted sectors are inverted between the two masks), two identical phase masks can be used instead. These phase masks are self-conjugate in case of a π phase shift. The finite pixel size of the SLMs places a restriction on the width of the sectors that can be displayed on the holograms. We show that we can implement optimal multi-sector phase masks with $N = 1, \dots, 16$. Suppressing

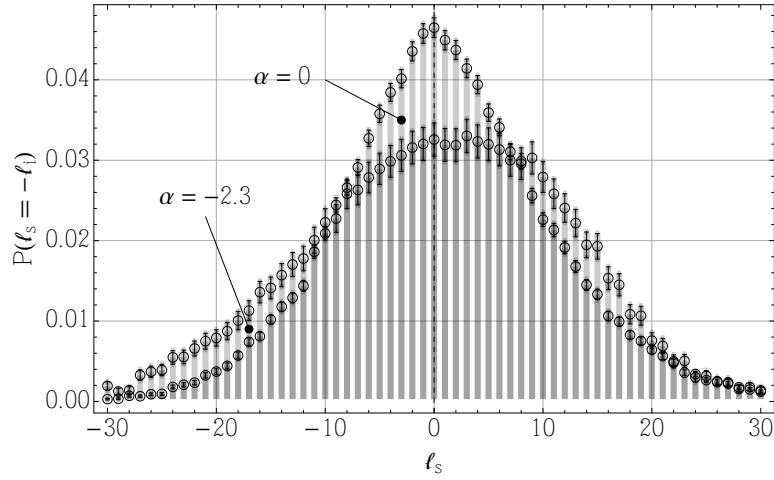


Figure 4.2: Detected orbital angular momentum spectra with projective measurements using traditional forked holograms. Shown is the coincidence probability $P(\ell_i, \ell_i = -\ell_s)$ for $\ell_s \in (-30, 30)$, for collinear ($\alpha = 0$) and near-collinear ($\alpha = -2.3$) phase-matching conditions.

the centres of the holograms, where the N angular sectors meet in a very limited spatial region of the SLM displays, did not turn out to be necessary.

The phase-matching conditions of the down-conversion process for the BBO crystal were adjusted by slightly changing the orientation of the crystal with respect to the propagation direction of the pump beam [230]. This allowed us to increase the width of the orbital angular momentum spectrum, and thus decrease the width of the angular correlations distribution. Measurements were performed for collinear ($\alpha = 0$) and near-collinear ($\alpha = -2.3$) phase-matching conditions.

The coincidence probability distribution $P(\theta - \theta')$ was obtained by changing the orientation θ' of the second phase mask over the range $\theta \pm 180^\circ$, where θ is the orientation of the first. We found that, for the purposes of the experiment, a Gaussian distribution is an excellent empirical fit for the coincidence probability distributions (fig. 4.1). The detected number of modes M , dependent on both the source and the detectors' properties, was obtained by substituting the Gaussian fit of the measured coincidences to $P(\theta - \theta')$ in eq. (4.7).

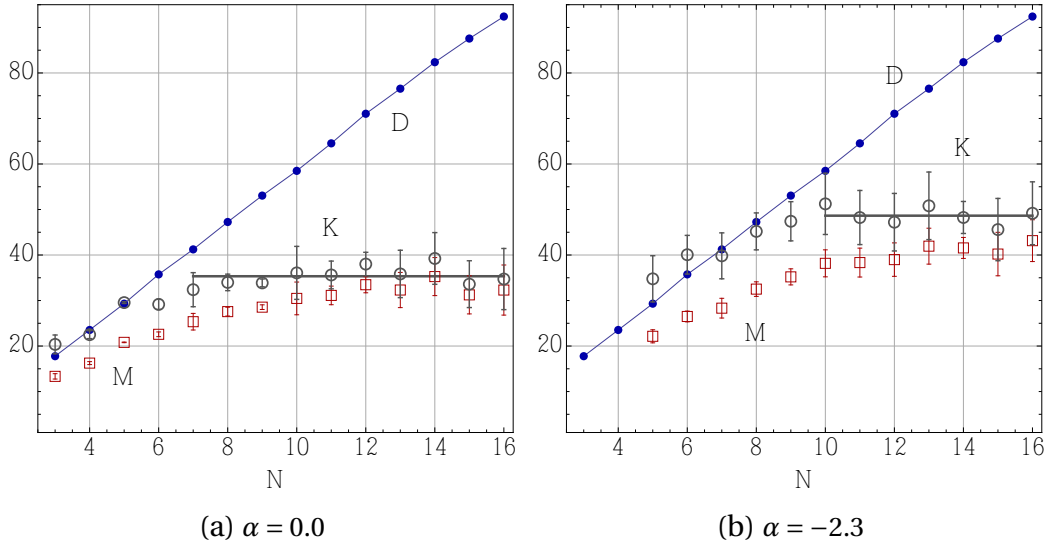


Figure 4.3: (a) Collinear phase-matching conditions. Phase mask dimensionality D from numerical model (blue points), measured M (red squares), and calculated dimensionality K (grey circles). We observe that $D < K$ for $N < 7$; therefore, the calculated M saturates to D for any given $N < 7$. The solid grey line shows the best estimation for the number of modes K of the source, 35 ± 2 . (b) Near-collinear phase-matching conditions. Given the wider spiral bandwidth in the near-collinear regime, K saturates to D for $N < 9$. The solid grey line shows the best estimation for the number of modes K of the source, 49 ± 2 .

4.3.2 Experimental results and discussion

The phase masks used have no radial structure. Any sensitivity of the detection apparatus to the radial quantum number p was therefore due to the spatial selectivity of the SMF coupling. Unlike full projective measurements of the down-conversion entangled state over a range of OAM eigenstates $|\ell\rangle$ (fig. 4.2), a phase-mask determination of the dimensionality K of the source does not provide any direct information on the shape of the OAM spectrum.

We considered the OAM spectrum generated by the source and the coincidence probability obtained from the numerical model, both fitted with Gaussian distributions, from which the dimensionalities K and D can respectively be obtained. We performed projective measurements of idler and signal over $|\ell\rangle$ and $|-\ell\rangle$ respectively to verify the validity of the assumption concerning the OAM spectrum (fig. 4.2). The numerical model, from which the values of D

for different N are obtained, calculates the overlap in eq. (4.3). Although the theoretical shape of the distribution of the coefficients γ_ℓ , which characterize the action of a phase mask on a light field, has own distinctive features, its implementation on an SLM makes it possible to approximate it with a Gaussian distribution. In fact, as the hologram representing the phase plate is rotated on the surface of the SLM, any imperfections (finite pixel size, surface roughness, slight unevenness of the phase shift, electrical fluctuations) influence the effect of the phase plate in a stochastic fashion. As this a very small overall effect, it does not change the dimensionality of the phase plate but rather smooths out the distribution of the γ_ℓ coefficients.

When the dimensionality K of the generated state is very different from the dimensionality D accessible to the detection system, the resulting measured dimensionality, M , is given by the smaller of the two. For cases where K and D are comparable, M can be approximated by noting that all three distributions are close to Gaussian in form and hence their contributing widths can be combined as:

$$\frac{1}{M^2} \simeq \frac{1}{D^2} + \frac{1}{K^2} \quad (4.8)$$

which gives:

$$M \simeq \frac{DK}{\sqrt{D^2 + K^2}} \quad (4.9)$$

from which the Schmidt number K can be derived:

$$K \simeq \frac{DM}{\sqrt{D^2 - M^2}}. \quad (4.10)$$

Consequently, the source dimensionality K can be inferred from the maximum number of modes D that can be detected by the N -sector phase mask and the width M of the measured coincidence distribution. The calculated dimensionality for each N -sector phase mask is shown in fig. 4.3a (collinear phase-matching) and 4.3b (near-collinear phase-matching). We measured Schmidt numbers of 35 ± 2 for collinear down-conversion, and 49 ± 2 in the near-collinear case. The

results for source dimensionality obtained from the phase-mask analysis are compatible with the Schmidt number derived from projective spiral bandwidth measurement, with the assumption of perfect single-mode detection.

The mean visibility achieved in the experiment, defined here as the ratio between the mean baseline of the measured coincidence probability and the peak at $\theta - \theta' = 0$, without background subtraction, is 90% for collinear phase-matching, and 92% for near-collinear. Systematic errors due to misalignment are found to be much larger than photon statistics uncertainties.

We have shown how multi-sector phase-mask analysers can be implemented using spatial light modulators, and used them to probe the effective number of modes in the high-dimensional bi-photon entangled state produced by parametric down-conversion. We used a set of several multi-sector analysers to infer the Schmidt number for different phase-matching conditions, and therefore, different widths of the OAM spectrum of the source.

CHAPTER 5

Mutually unbiased bases in high-dimensional subspaces of OAM: measurement and applications

Measurements in sets of mutually unbiased bases (MUB) are integral to quantum science. Two orthonormal bases are said to be mutually unbiased if the measurement of a state in one basis provides no information about the state as described in the other basis. Mutually unbiased bases have found several applications, which include quantum error correction codes [118, 67], quantum cloning [184, 182] and quantum cryptographic protocols [225]. The use of joint local measurements in mutually unbiased bases allows efficient quantum state reconstruction [277, 3, 100]. Defining MUB for arbitrary high-dimensional systems is however theoretically difficult, and measurements in such bases can be experimentally challenging.

Up until recently, mutually unbiased bases have only been applied in experimental quantum optics to optical states of polarization and continuous linear

This chapter includes material previously published in the following papers:

- D. Giovannini, J. Romero, J. Leach, A. Dudley, A. Forbes and M. J. Padgett, “Characterization of high-dimensional entangled systems via mutually unbiased measurements”, *Phys. Rev. Lett.* 110(14), 143601 (2013)
- M. Mafu, A. Dudley, S. Goyal, D. Giovannini, M. McLaren, M. J. Padgett, T. Konrad, F. Petruccione, N. Lütkenhaus and A. Forbes, “Higher-dimensional orbital angular momentum based quantum key distribution with mutually unbiased bases”, *Phys. Rev. A* 88(3), 032305 (2013)

momentum. We extended the use of MUB to high-dimensional finite subspaces of the orbital angular momentum (OAM) of light, which provides a practical degree of freedom to encode quantum information in higher-dimensional alphabets and offers a discrete and unbounded state space for which one can define sets of mutually unbiased bases [277].

Only a subset of the unbounded space provided by OAM is experimentally accessible, as defined by the measurement spiral bandwidth. We employed spontaneous parametric down-conversion (SPDC) to produce two-photon states entangled over a wide range of OAM modes [226]. We demonstrated a scalable implementation of quantum measurements in MUB of high-dimensional OAM subspaces by means of complex amplitude modulation in the single-photon regime. Spatial light modulators allow measurements in any arbitrary superposition of OAM modes, giving access to different high-dimensional subspaces within the same experimental apparatus.

By using this high-spiral bandwidth system and SLM-based detection, we demonstrated single-photon measurements in high-dimensional MUB of OAM. We also showed how these measurements can be used for efficient quantum state reconstruction of bipartite entangled states in dimension d^2 , by means of minimal complete sets of tomographic measurements [111]. We used the full sets of MUB of each of the two photons of an entangled pair to perform a tomographically complete reconstruction of the entangled state with precisely the minimum number of measurements. The experimental procedure and the reconstruction technique presented can be readily extended to higher dimensions and multi-partite systems, whenever MUB for the d -dimensional subsystems can be defined.

The relative ease with which one can generate, manipulate and measure high-dimensional OAM quantum superpositions paves the way to new applications of this degree of freedom and is instrumental in the realization of a number of efficient high-dimensional quantum information protocols and efficient entanglement detection schemes [245]. The implementation of such local measurements also lays the groundwork for high-dimensional realizations of quantum key distribution (QKD), where two parties rely on detection events arising from independent choices among a set of mutually unbiased bases. Us-

ing OAM-entangled photon pairs to encode information in higher-dimensional MUB leads to an increase in the encoding density and secure key rate [171], an area that has previously been explored using other degrees of freedom such as time-energy [31, 253, 7, 188]. In addition, MUB serve as a test bed with which one can explore fundamental topics in quantum information and could provide important insight into the nature of information in physical systems.

5.1 Measuring high-dimensional orbital angular momentum states in MUB

The ability to characterize a quantum state is essential in quantum information. Describing complicated high-dimensional quantum states is challenging but can yield a very large set of states with which to encode information. It is difficult to define MUB for large-dimensional systems, both because of theoretical limitations and practical reasons connected with the experimental implementation of a complete high-dimensional set of MUB. If, however, the system exhibits bi- or multi-partite entanglement, it is possible to perform a reconstruction of the state of the overall system by means of local measurements in MUB of its subsystems. This procedure allows a complete tomographic reconstruction of the overall state, with the same minimum number of measurements, that only requires the definition of MUB in a much smaller Hilbert space (whose size is the square root of the dimension of the overall bipartite system). An example of this procedure is shown in the case of a photonic implementation of a bipartite multi-level entangled system using the orbital angular momentum of light of a pair of down-converted photons.

5.1.1 Mutually unbiased bases

Mutually unbiased bases [277, 133] are a key concept in quantum science, as they are intimately related to the nature of quantum information [272, 23, 93]. Measurements made in one basis part of a set of MUB provide no informa-

tion about the state, if the state was prepared in another basis from the same set of MUB. In quantum mechanics, the amount of information that can be extracted from a physical system is fundamentally limited by the uncertainty relations [272, 23]. In this context, MUB acquire a fundamental relevance, because they serve as a test bed with which one can explore general uncertainty relations and, ultimately, complementarity [241, 93]. Some important questions related to MUB remain open [93, 272]: what is the number of MUB for an arbitrary dimension d and why is mutual unbiasedness not enough to guarantee a strong uncertainty relation? While we do not seek to answer these questions, we provide an accessible experimental platform for exploring these problems by demonstrating measurements in complete sets of MUB.

Many quantum information protocols depend upon the use of MUB. For example, quantum key distribution (QKD) relies on the fact that measurements in one basis preclude knowledge of the state in any of the others [37, 141, 173]. In addition, MUB play an important role in the reconstruction of quantum states [277, 101, 100], where they have been successfully used to enable the optimal reconstruction of entangled states of polarization [3] and single-photon linear momentum states [166].

It is known that a Hilbert space of dimension D will have at most $D + 1$ MUB [133, 277, 22]. In 1989, Wootters showed that if one can find $D + 1$ mutually unbiased bases in dimension D , these bases provide a set of measurements that can be used to optimally determine the density matrix of a D -dimensional system [277]. However, this approach rapidly breaks down for large D for two reasons: first, defining MUB in high dimensions becomes increasingly difficult [93, 59], and second, performing the measurements in a complete high-dimensional set of MUB becomes experimentally challenging [3, 183]. This is especially relevant for multi-level multi-particle systems, where the dimension of the overall system scales as $D = d^N$, with d the dimension of the Hilbert spaces of the N individual subsystems.

We show experimentally that the alternative approach of performing local measurements in the MUB of the single particles of a multi-particle system still allows a complete reconstruction of the overall density matrix with a minimum number of measurements [251]. The significant benefit of our procedure is that

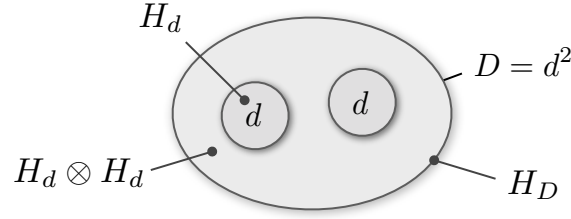


Figure 5.1: Illustration of the state spaces of a bipartite system, where the system has dimension D and each subsystem d . Adamson and Steinberg performed measurements in the Hilbert space H_D of the composite system [3], while we perform joint local measurements in the spaces H_d of the individual subsystems (for $d = 2$ to 5).

it only requires the definition of MUB in a Hilbert space of size $d = D^{1/N}$, as the state spaces of the individual photons are always smaller than the state space of the composite system (fig. 5.1). We illustrated this approach in the case of a photonic implementation of a bipartite, multi-level entangled system ($d = D^{1/2}$) using the orbital angular momentum of light.

Consider two operators in a d -dimensional Hilbert space with orthonormal spectral decompositions. These operators, and their basis states, are said to be mutually unbiased [133, 277] if

$$|\langle \psi_{m,i} | \psi_{n,j} \rangle|^2 = \begin{cases} 1/d & \text{for } m \neq n \\ \delta_{ij} & \text{for } m = n \end{cases} \quad (5.1)$$

for all i and j . For any two bases m and n , the indices i and j indicate the basis states within each of the two bases, respectively. Operators that are quantum-mechanical observables are sometimes called mutually complementary, or maximally noncommutative [241]. The name comes from the fact that, given any eigenstate of one observable, the eigenvalue resulting from a measurement of the other is completely undetermined. In other words, the state of a system described in one MUB provides no information about the state in another. It is known that the number of MUB in dimension d cannot exceed $d + 1$ [277, 93], and it is exactly $d + 1$ if d is prime or a prime power [277, 148].

The simplest set of mutually unbiased observables can be found in dimension $d = 2$. For example, in the two-dimensional Hilbert space of polarization, the bases of horizontal/vertical, diagonal/anti-diagonal and left/right circular

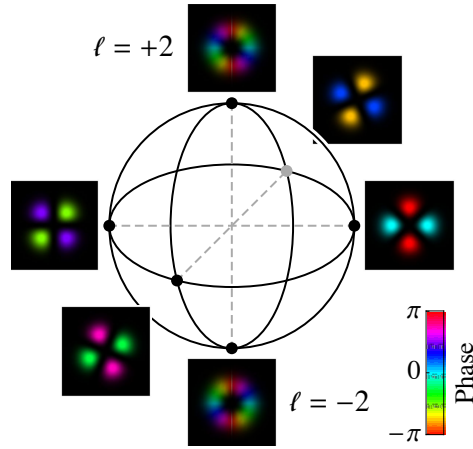


Figure 5.2: Mutually unbiased modes for $d = 2$ in the $|\ell| = 2$ OAM subspace. The brightness of the transverse profiles corresponds to the intensity of the modes; the colour represents phase.

polarizations provide a set of three MUB. Two states belonging to the same basis are orthonormal, while the square of the inner product of any two states belonging to different bases is always $1/2$. Equivalent mutually unbiased states can be implemented using other two-dimensional state spaces, e.g. a subspace of OAM (fig. 5.2).

5.1.2 Mutually unbiased bases for OAM subspaces

The unbounded Hilbert space of OAM is one example of a scalable high-dimensional resource that can be used for quantum information science [172, 161, 121, 234]. For example, the entanglement of high-dimensional states provides implementations of QKD that are more tolerant to eavesdropping and can improve the bit rate in other quantum communication protocols [52, 68, 31, 269, 90, 123].

One of the advantages of OAM is the ability to access d -dimensional subspaces [81], for each of which we can define all existing MUB [124]. We implemented measurements in high-dimensional MUB within the OAM degree of freedom, and we showed that the MUB corresponding to d -dimensional subspaces are readily accessible with simple laboratory procedures. Furthermore, we showed that measurements in MUB of these subspaces can be used for the

complete tomographic reconstruction of multipartite entangled systems with the minimum number of measurements. We produced entangled photon pairs by means of spontaneous parametric down-conversion that we then measured in full sets of $d + 1$ MUB for OAM, for dimensions ranging from $d = 2$ to 5. The states belonging to the MUB are defined as superpositions of Laguerre-Gaussian (LG) modes.

A general single-photon state in a d -dimensional subspace can be described by an orthonormal basis set of OAM modes $\{|\ell\rangle\}$ as

$$|\psi\rangle = \sum_{\{\ell\}} c_{\ell} |\ell\rangle. \quad (5.2)$$

The complex coefficients c_{ℓ} are subject to the normalization condition $\sum c_{\ell}^2 = 1$. Defining MUB in a general d -dimensional space is a difficult problem [59]; however, for a number of low-dimensional cases, it is possible to find complete sets of MUB using simple procedures [60]. For these cases, which include the dimensions 2 to 5, the d orthogonal states $\{|\ell\rangle\}$ can be chosen to be one of the MUB. The states belonging to the remaining d MUB are found to be superpositions of the basis states with coefficients of equal magnitude $|c_{\ell}| = 1/\sqrt{d}$ but differing phases.

5.1.3 Experimental methods

A 3 mm-thick BBO crystal cut for type-I collinear SPDC was used for the production of frequency-degenerate entangled photon pairs at 710 nm (fig. 2.5). In order for the crystal to produce two-photon states entangled over a wider range of OAM modes, we tuned the phase-matching conditions of the BBO crystal to increase the OAM spectrum of the down-converted state [226]. The SLMs act as reconfigurable computer-generated holograms (CGHs) that enabled us to measure any arbitrary superposition of OAM modes. The SLMs were used to modulate the phase and introduce a spatially dependent attenuation to discard light into the zero diffraction order, allowing the manipulation of the complex amplitude of the incoming light [15, 83, 124].

We pumped the crystal with a plane phase front. In order to observe correlations in all bases (instead of anti-correlations), the hologram displayed in one of the two detection arms was phase-conjugate with respect to the other [172]. The projected Gaussian mode in each arm was then imaged onto a single-mode fibre (SMFs) that was coupled to a single-photon photodiode detector. Each of the two detector outputs were routed to coincidence-counting electronics with a timing window of 10 ns. Narrow-band, 10 nm interference filters were placed in front of the detectors to ensure that the frequency spread of the detected down-converted fields is small compared to the central frequencies.

The combination of the two SLMs, single-mode fibres and coincidence-counting electronics were used to perform projective measurements on the entangled state of photons A and B described by the positive operators

$$\Pi_{m,i;n,j} = |\psi_{m,i}\rangle_A |\psi_{n,j}\rangle_B^* \langle\psi_{m,i}|_A \langle\psi_{n,j}|_B^*. \quad (5.3)$$

Here, the single-photon states $|\psi\rangle_A$ and $|\psi\rangle_B$ belong to MUB in d dimensions and are given by

$$|\psi_{m,i}\rangle = \sum_{\{\ell\}} c_{m,i,\ell} |\ell\rangle, \quad (5.4)$$

where $c_{m,i,\ell}$ is a complex coefficient. The indices m and n , which correspond to the basis indices, range from 1 to $d + 1$; the indices i and j , which represent the state within each basis, range from 1 to d . For each dimension d , we chose one set of OAM states $\{|\ell\rangle\}$. The OAM values used were $\{\ell\} = \{-2, +2\}$ for $d = 2$, $\{-2, -1, +1, +2\}$ for $d = 4$, and $\{-\lfloor d/2 \rfloor, \dots, +\lfloor d/2 \rfloor\}$ for $d = 3$ and 5. Modes with $|\ell| = 2$ were chosen for $d = 2$ to ensure the symmetry of the measured superpositions and to reduce the crosstalk between the modes employed (inversely proportional to $\Delta\ell$). For each d , we took the orthonormal basis given above to be the basis corresponding to $m = 1$; the remaining bases were composed of superpositions of the $m = 1$ states with appropriate complex coefficients. For the dimensions considered, the magnitude of these complex coefficients is $1/\sqrt{d}$ for all i and ℓ .

To determine the phase terms $c_{m,i,\ell}$ that define the MUB (for $m = 2$ to $d + 1$),

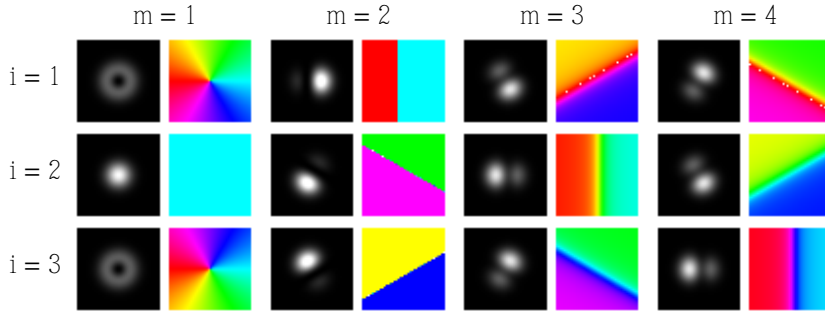


Figure 5.3: Mutually unbiased modes i for each of the 4 bases in $d = 3$. The greyscale images represent the intensity; the colour images represent the phase. The first column, $m = 1$, corresponds to the orthonormal three-dimensional Laguerre-Gaussian basis with OAM ranging from $\ell = -1$ to $+1$.

we used the methods outlined in references [60, 58]: the coefficients were here obtained from the mutually unbiased vectors derived from $d \times d$ dephased Hadamard matrices. These matrices are unique for $d = 2, 3, 4$ and 5 . For $d = 2$, the MUB obtained are the familiar set of bases that one usually associates with polarization states. Consequently, the two-dimensional MUB for OAM [202] are the analogue of those for polarization [63]. All the modes used for $d = 3$ and $d = 5$ are shown in fig. 5.3 and 5.4 respectively. The complete sets of mutually unbiased vectors used in the quantum state tomography, for dimensions from $d = 2$ to 5 , are reported in appendix A.

The experimental procedure and the reconstruction technique can be readily extended to higher dimensions. The existence of full sets of $d + 1$ MUB has however only been proven for dimensions d , where d is a prime number or a power of a prime. Finding MUB in higher prime power dimensions, especially sets that may be suitable for practical implementations, remains challenging. It should also be noted that, despite MUB being particularly advantageous to efficiently reconstruct the density matrix of an unknown state encoded in the spatial modes of a single photon, as d increases the complicated structures of the modes involved may negatively affect the detection efficiency.

After recording the coincidence count rates C_k for each choice of n, m, i and j , and the single-channel count rates A_k and B_k , we converted the count rates

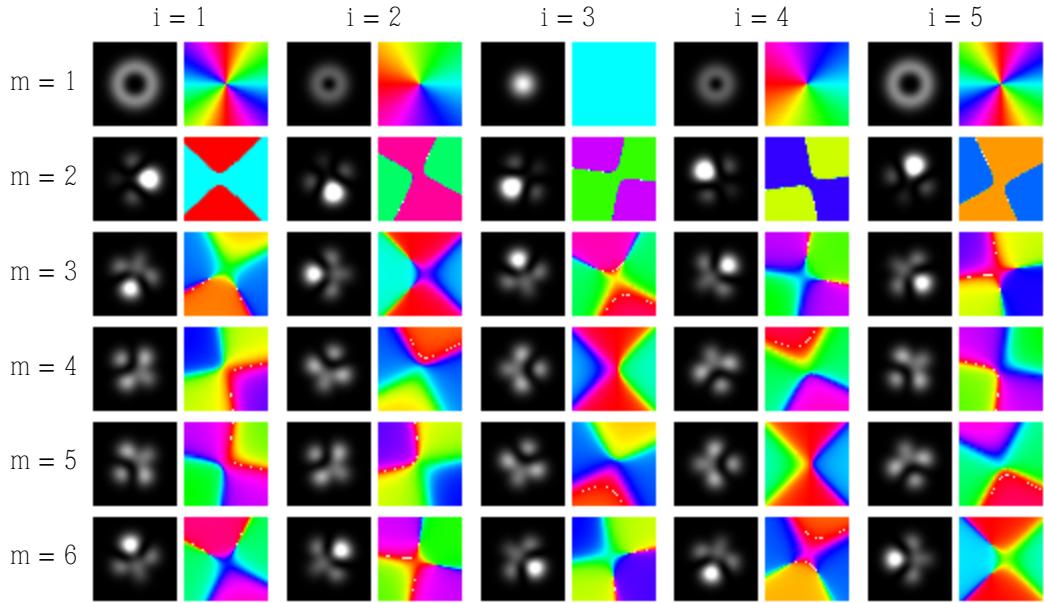


Figure 5.4: Mutually unbiased modes i for each of the 6 bases m in $d = 5$. The greyscale images represent the intensity; the colour images represent the phase. The first row, $m = 1$, corresponds to the orthonormal five-dimensional Laguerre-Gaussian basis with OAM ranging from $\ell = -2$ to $+2$.

to detection probabilities through

$$p_k = \Upsilon \left(\frac{C_k - A_k B_k \Delta t}{A_k B_k \Delta t} \right), \quad (5.5)$$

where Δt is the gate time of our coincidence-counting electronics and Υ an appropriate normalization factor. The term $A_k B_k \Delta t$ corresponds to the uncorrelated accidental count rate U_k and the normalization factor

$$\Upsilon = Q / \sum_{k=1}^{d^2 Q} C_k \quad (5.6)$$

depends on the type of tomographic reconstruction performed, in order to ensure proper normalization of the coincidence probabilities associated with measurements in those bases where a number of basis states smaller than d was considered. The factor Q indicates the number of $d \times d$ quadrants in the correlations matrix for the set of measurements of choice. The product

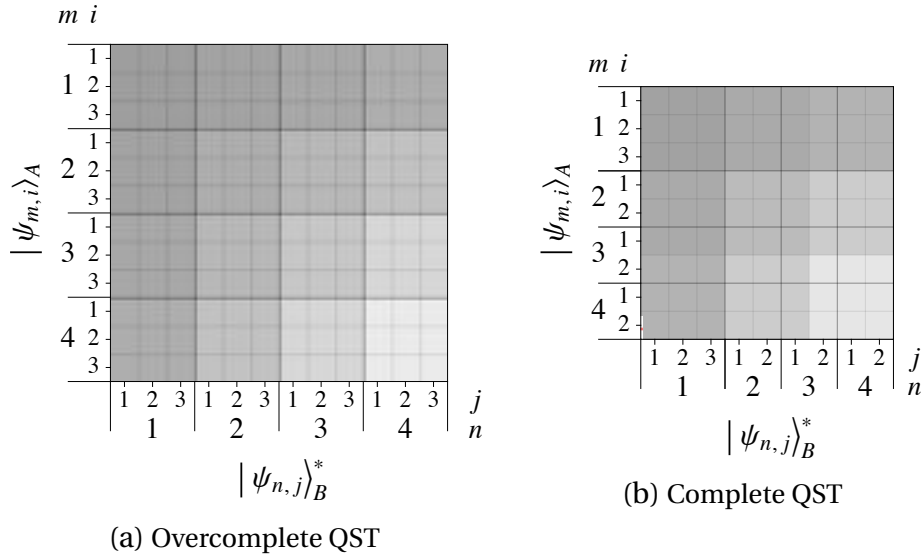


Figure 5.5: Sets of measurements for (a) overcomplete state tomography and (b) complete state tomography, for $d = 3$ ($D = 3^2$). The shaded areas indicate quadrants of size $d \times d$, for each of which we expect $\sum_k p_k = 1$.

$d^2 Q$ corresponds to the total number of independent measurements. For an overcomplete tomography, where we set $\sum_k^{d^2} p_k = 1$ for any given choice of m and n , $Q = (d + 1)^2$ (fig. 5.5a). For a tomographically complete reconstruction that uses the presented subset of MUB measurements, $Q = [1 + (d - 1)]^2 = d^2$ (fig. 5.5b).

5.2 Efficient high-dimensional quantum state reconstruction with mutually unbiased bases

5.2.1 Mutually unbiased bases in quantum state tomography

In general, it is possible for a system to include more than one particle. If one considers a d -dimensional state space for each particle, the dimension D of a system of N particles will be $D = d^N$. Such a system will be unambiguously specified by its density matrix ρ , a positive-semidefinite unit-trace Hermitian

operator that includes $d^{2N} - 1$ independent real parameters ($d^4 - 1$ for a bipartite system).

The determination of the density matrix of an unknown quantum system is called quantum state tomography (QST) [138, 157, 11], a process in which MUB play an important role. One approach to QST is to perform measurements in the MUB of the D -dimensional state space of the composite system [277]. However, such measurements are very challenging, as they require the definition of MUB for Hilbert spaces of very high dimension and can require the implementation of entangled observables [3]. Our approach is simpler, as we use the MUB of the state spaces of the single particles.

Let us consider for simplicity a bipartite system. An overcomplete set of measurements for the reconstruction of the D -dimensional system is provided by the pairwise combinations of all single-particle MUB states. The total number of independent measurements for this approach is equal to $(d(d+1))^2$, which is always greater than $d^4 - 1$. We propose another suitable set of measurements, given by pairwise combinations of states from an appropriate subset of the overcomplete set. This subset contains all the states that constitute one of the MUB and, for each of the remaining d MUB, all states but one. It can be shown that the conditions for the completeness of a set of tomographic measurements [11] are satisfied by this reconstruction strategy.

One can express the density matrix ρ as a linear combination of any complete basis of $d^2 \times d^2$ matrices Γ_μ with complex coefficients γ_μ [251]:

$$\rho = \frac{\Gamma_0}{D} + \sum_{\mu=1}^{D^2-1} \gamma_\mu \Gamma_\mu, \quad (5.7)$$

where $D = d^2$ is the dimension of our bipartite system. The basis matrices Γ_μ here chosen have the following properties:

$$\text{Tr}(\Gamma_\mu \cdot \Gamma_\nu) = \delta_{\mu,\nu} \quad (5.8a)$$

$$\kappa = \sum_{\mu} \Gamma_{\mu} \text{Tr}(\Gamma_{\mu} \cdot \kappa), \quad (5.8b)$$

where κ is any $d^2 \times d^2$ matrix. A suitable set of Hermitian matrices Γ_{μ} for the decomposition of ρ is given by the generalized Gell-Mann matrices for dimension D .

A necessary and sufficient condition for the completeness of the set of tomographic states $\{|\psi_{\mu}\rangle\}$ (associated with the two-qudit observables Π_{μ}) is given by the invertibility of the matrix

$$B_{\mu\nu} = \langle \psi_{\mu} | \Gamma_{\nu} | \psi_{\mu} \rangle, \quad (5.9)$$

which allows us to express the complex coefficients γ_{μ} in terms of probabilities $p_{\mu} = \langle \psi_{\mu} | \rho | \psi_{\mu} \rangle$ [11]:

$$\gamma_{\mu} = d^2 \sum_{\nu=1}^{d^2} (B^{-1})_{\mu\nu} p_{\nu}. \quad (5.10)$$

Let us define the orthonormal set of basis vectors u_i in dimension d , whose elements are given by $(u_i)_j = \delta_{ij}$. For a choice of two single-particle MUB vectors for the qudit subsystems A and B

$$u_A = (a_1, \dots, a_d) \quad (5.11a)$$

$$u_B = (b_1, \dots, b_d), \quad (5.11b)$$

we can express the elements $j = 1, 2, \dots, D$ of the corresponding vector for the D -dimensional state space of the bipartite system as

$$(v_{AB})_j = a_{\alpha} b_{\beta}, \quad (5.12)$$

where (α, β) are all pairwise permutations of indices $\{1, \dots, d\}$. From the D -

dimensional vectors v_{AB} we then define the states $|\psi_\mu\rangle$ that describe the measurements on the composite system. After calculating the states $|\psi_\mu\rangle$ for the subset of MUB measurements for complete tomography defined previously, we find the invertible matrix B through eq. (5.9). This approach gives exactly the d^4 independent measurements that can then be used for a tomographically complete reconstruction of the D -dimensional system. While the number of measurements still scales with d^4 , our approach introduces a significant reduction of the number of measurements performed, as compared to other methods (see tab. 5.1 for an example).

5.2.2 State reconstruction methods

An overcomplete set of measurements was obtained by scanning through all possible values of m and i , for photon A , and n and j , for photon B . For every combination of m, n, i and j , we recorded the coincidence counts and both the single channel counts resulting from the projective measurement. From this set of data, we extracted the tomographically complete set of measurements previously described. These count rates are converted to detection probabilities through the following relationship:

$$p_k = \frac{d^2}{\sum C_k} \frac{C_k - U_k}{U_k}, \quad (5.13)$$

where the index k corresponds to a unique choice of measurement settings m, n, i and j , C_k is the coincidence count rate and U_k is the anticipated uncorrelated coincidence rate, which is estimated by taking the product of the single-channel count rates and the gate time (fig. 5.6). The normalization approach that we took accounts for different hologram efficiencies for different modes. The non-perfect uniformity of the background probabilities for $m \neq n$ can be put down to the intensity-coding approach, which requires complex amplitude modulation on phase-only SLMs. There are variations from basis to basis, because the spatial functions to be reproduced can differ substantially, and some are more difficult to implement on a pixellated device with finite

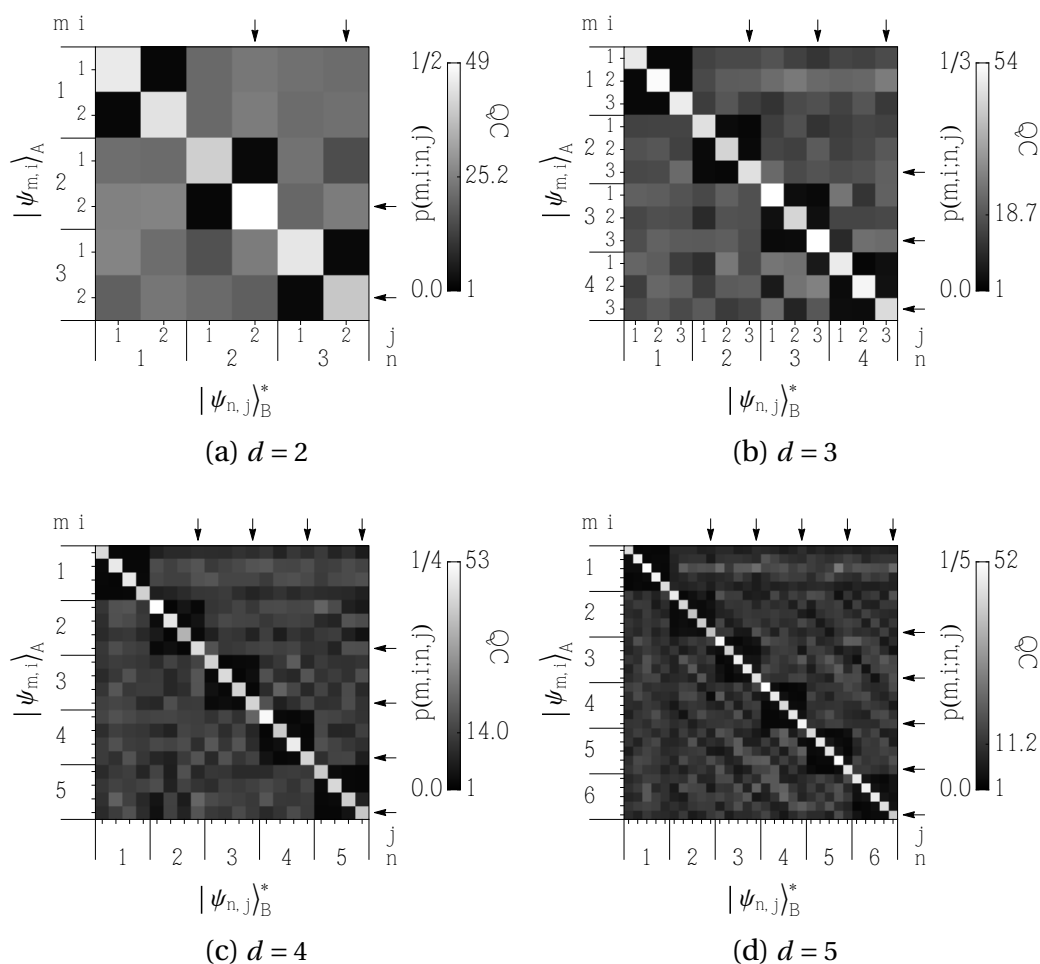


Figure 5.6: Joint probabilities of detecting photon A in state $|\psi_{m,i}\rangle_A$ and photon B in state $|\psi_{n,j}\rangle_B$. The results are normalized such that the sum of the joint detection probabilities for measurements in any two bases m and n are unity. Therefore, the probabilities represented by the leading diagonal are expected to be $1/d$, and all probabilities for $m \neq n$ are expected to be $1/d^2$. We also display the quantum contrast QC , which is given by the ratio of the measured coincidence rate to that of the expected accidental coincidences. The arrows indicate the rows and columns of measurements not required for the complete tomographic reconstruction of the density matrix.

resolution.

The task of the fitting procedure is to find the optimal density matrix ρ of the D -dimensional system that best reproduces the experimental results. The parameters of the density matrix were established through numerical minimization of the Pearson's cumulative test statistic [194, 20]

$$\chi^2 = \sum_{k=1}^{d^4} \frac{(p_k - p'_k)^2}{p'_k}, \quad (5.14)$$

where p_k are the probabilities from the experiment, and $p'_k = \text{Tr}[\rho \Pi_k]$ are those predicted from the reconstructed density matrix. The positivity of the reconstructed density matrices was ensured through an appropriate choice of basis matrices Γ_μ , given here by eqs. (5.8), which make the coefficients of the search space γ_μ real. The density matrices so reconstructed were also checked to be Hermitian and positive semi-definite, as rounding errors in the numerical optimization may lead to non-physical results.

5.2.3 Results

The reconstructed density matrices for dimensions 2, 3, 4 and 5 are shown in fig. 5.7. For each reconstructed density matrix ρ , we calculated the linear entropy $S = 1 - \text{Tr}(\rho^2)$ and the fidelity $F = \text{Tr}[\sqrt{\sqrt{\sigma}\rho\sqrt{\sigma}}]^2$, where σ is the D -dimensional maximally entangled density matrix associated with arbitrarily large spiral bandwidth and perfect detection. The uncertainties were calculated by repeating the reconstruction process for statistically equivalent copies of the original experimental data sets, each obtained by adding Poissonian fluctuations to the measured counts.

The reconstructed density matrices have low entropies, indicating pure states, and very high fidelities with respect to the maximally entangled state (used for reference). Due to the finite spiral bandwidth of our generated state [255, 226] and limitations in our measurement system, one would anticipate the fidelities to decrease and the entropies to increase as the dimension increases. Indeed, we observe this trend in our results.

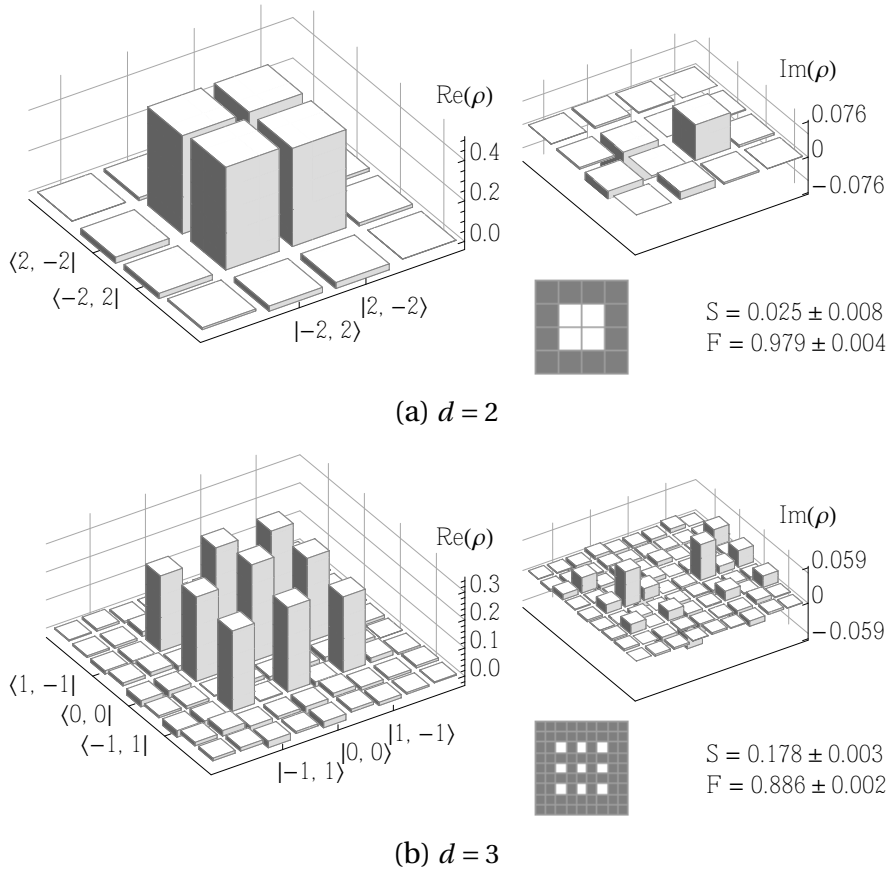
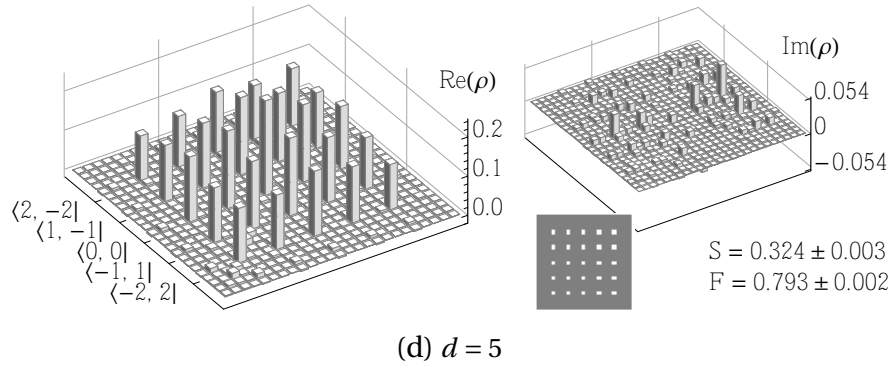
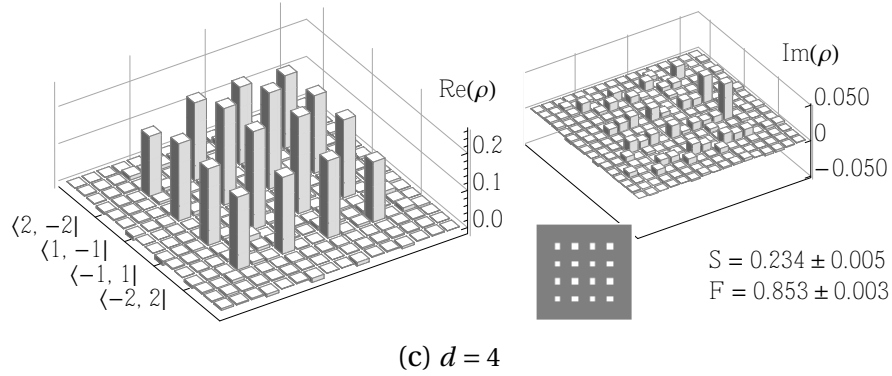


Figure 5.7: Results of tomographic reconstructions using complete sets of single-photon mutually unbiased bases measurements. The real parts of the reconstructed density matrices ρ are shown. Imaginary parts are smaller than 0.076 for $d = 2$, 0.059 for $d = 3$, and 0.050 for $d = 5, 6$. Also shown are the linear entropy S and fidelity F for the reconstructed density matrices. Two-dimensional plots: real parts of the theoretical density matrices for the maximally entangled states. (Continued on page 96.)

For comparison, we also implemented the approach described in [4]. We find comparable entropies and fidelities between the two approaches. However, our method requires significantly fewer measurements. For example, for $d = 5$, the number of measurements required is $d^4 = 625$, compared to 2025 for the procedure outlined in ref. [4]. Both methods rely on projective measurements in appropriate superpositions of the basis states in the dimension of choice. Neither is more experimentally demanding, as they can both be performed using the same set-up and only differ in the choice of projection states.



The number of joint measurements required to perform our reconstruction procedure is given by:

$$M_{\text{MUB}} = d^2 + 2d^2(d-1) + d^2(d-1)^2 = d^4, \quad (5.15)$$

which corresponds to the minimum number of parameters required to perform a complete quantum state tomography. The number of measurements required by the overcomplete quantum state reconstruction strategy outlined in ref. [4] requires instead the following total number of measurements:

$$M_{\text{QST}} = \left[4 \binom{d}{2} + d \right]^2. \quad (5.16)$$

The numerical optimization to find the density matrix ρ that provides the best fit to the experimental probabilities from eq. (5.5) is carried out by performing a random search over the parameter space of a complex left-triangular

	Method	M	S	F
$d = 2$	MUB	16	0.025 ± 0.008	0.979 ± 0.004
	QST	36	0.070 ± 0.007	0.958 ± 0.004
$d = 3$	MUB	81	0.178 ± 0.003	0.886 ± 0.002
	QST	225	0.179 ± 0.005	0.893 ± 0.003
$d = 4$	MUB	256	0.234 ± 0.005	0.853 ± 0.003
	QST	784	0.281 ± 0.009	0.818 ± 0.006
$d = 5$	MUB	625	0.324 ± 0.003	0.793 ± 0.002
	QST	2025	0.364 ± 0.008	0.764 ± 0.006

Table 5.1: Linear entropy S and fidelity F (with respect to a maximally entangled density matrix) for density matrices reconstructed from overcomplete quantum state tomography (QST) and measurements in mutually unbiased bases (MUB). M represents the number of measurements needed for the indicated reconstruction method.

matrix T [11], from which a physical guessed density matrix is derived:

$$\rho' = T^\dagger T / \text{Tr}(T^\dagger T). \quad (5.17)$$

We reconstructed the states from $d = 2$ to 5 using both methods. A quantitative comparison of the results is shown in tab. 5.1.

The MUB reconstruction method is applied here to almost maximally entangled states. The density matrices of maximally entangled states have low rank¹, $r < D$, and could thus be efficiently reconstructed through compressed sensing [122, 168]. In the general case, however, a complete quantum state reconstruction by means of appropriately selected projection operators may be more appropriate and produce results with higher fidelity.

We have thus demonstrated single-photon measurements for MUB in the OAM degree of freedom and shown how these measurements can be used for efficient quantum state reconstruction. The procedure of measuring combinations of all single-photon states in one basis and all but one state in the remaining bases gives a minimal complete set of tomographic measurements. This experimental method can be readily applied to multi-level multi-partite

¹That is, a small number of linearly independent rows or columns.

systems.

The OAM degree of freedom is becoming an important resource for quantum information science. Therefore, the ability to measure states in MUB is an important step for quantum protocols implemented in this degree of freedom. Measuring MUB in high-dimensional spaces is not just of practical importance for QKD protocols, but it can also provide important insight into the nature of information in physical systems.

5.3 Quantum key distribution with high-dimensional OAM mutually unbiased bases

Quantum key distribution (QKD) is one of the first quantum protocols to have been successfully demonstrated in several different laboratory and environmental conditions [89, 258], as well as reaching an advanced level of technical and theoretical development and becoming the first commercial application of quantum cryptography. In quantum key distribution, two parties, commonly named Alice and Bob, use a shared quantum channel to create a shared secret key [113, 238]. The channel is not used to transmit information, but to establish a random sequence of digits (the key) that can then be used as a one-time pad to protect a subsequent classical communication between the two parties.

The first QKD scheme was proposed by Bennett and Brassard in 1984, and it is now known as the BB84 protocol [37]. In the BB84 protocol, Alice and Bob exchange polarized photons over a quantum channel. A classical channel (public channel) allows them instead to compare the preparation and measurement stages. While it should be assumed that an eavesdropper (Eve) is unable to impersonate Bob when communicating classically with Alice, and Alice when communicating with Bob, the fact that Eve may intercept any messages sent over the public channel is to be taken into consideration.

Alice prepares a sequence of single photons, each randomly and uniformly selected to be in a state belonging to one of a set of mutually unbiased bases. In the polarization case, the bases can be taken to be the horizontal/vertical

and diagonal/antidiagonal ones. She associates the bit value 0 with the former basis and the bit value 1 with the latter. The photons are then transmitted to Bob through a suitable quantum channel, for instance free space or an optical fibre. Bob then randomly selects one of the two measurement bases to measure each of the photons received. After the exchange, Bob communicates to Alice over the public channel the basis choices for the measurement of each photon, and Alice tells Bob in which cases they used the same preparation and measurement bases. Uncorrelated preparation-measurement events are discarded; the bit values for those measured in the same preparation basis constitute the sifted key. The possibility of the presence of an eavesdropper must be considered by examining the complete bit stream, and discussed over the public channel.

Quantum key distribution protocols can be classified in prepare-and-measure (PM) schemes or entanglement-based (EB) schemes. Examples of PM schemes are the BB84 [37], B92 [36], six-state [63] and SARG04 [237] protocols. In a prepare-and-measure protocol, a system is prepared in state $|\psi\rangle$ and measured in state $|\psi'\rangle$. Only if $|\psi\rangle$ and $|\psi'\rangle$ belong to the same basis in a set of MUB the two parties share a conclusive outcome. In an entanglement-based scheme, on the other hand, a projective measurement in state $|\psi\rangle$ is performed on one of the two photons in an entangled two-photon state, and a measurement in state $|\psi'\rangle$ is performed on the other, where $|\psi\rangle$ and $|\psi'\rangle$ are all possible states from the same set of MUB for the first and second photons respectively. In general, PM schemes can be translated into EB schemes: the entanglement-based QKD protocol proposed by Ekert in 1991 [97], for instance, can be shown to be equivalent to the prepare-and-measure BB84 protocol [39].

Mutually unbiased bases are of fundamental importance in QKD, since projective measurements in one basis provide no information on the state as described in any of the other bases [37, 93]. If Eve measures the photon transmitted by Alice to Bob in the incorrect basis, either in a PM or EB scheme, she will obtain no information *and* will introduce a disturbance in the system that will lead to her detection. Although MUB offer fundamental security against eavesdropping in QKD protocols, the key generation rate is limited by the number of MUB one can define in a particular implementation. As an example, when using the polarization degree of freedom of light, which is two-dimensional, only a

maximum of one bit of information per photon can be transmitted.

It has been shown, however, that the exchange of systems that give access to a high-dimensional Hilbert space allows more robust implementations of QKD schemes in terms of abstract noise measures [242, 99]. Still, their actual performance in terms of secure key rate, as the dimensionality of the system is increased, depends on the increase in both noise rate and the robustness of the system against noise. It has been shown theoretically that MUB for higher-dimensional OAM states can be used to encode and transmit bit strings securely using the BB84 protocol [68, 284]; three-state systems have received particular interest in the past [30, 121, 57].

A standard PM implementation of a generalized, high-dimensional BB84 protocol has previously been reported [225]. The scheme relied on 11 OAM modes and an orthonormal basis of 11 superposition of these modes, such that one basis is unbiased with respect to the other. Therefore, only two of the $d + 1 = 12$ available MUB were employed. QKD entanglement-based schemes can however also be experimentally implemented using complete sets of high-dimensional MUB, if it can be proven that the detection efficiency depends only on the basis choice and not the element within each basis [171].

5.3.1 Average error rate

A general EB quantum key distribution scheme involves two parties, each of which receives one of a pair of entangled photons. They measure the states received, and publicly announce the measurement basis. The average error rate of the QKD protocol, which results from noise such as that introduced in the transmission channel and by errors in the measurements, is estimated by comparing a small portion of the measurements. Noise, however, could also be introduced by the presence of an eavesdropper. The error rate refers to the probability that Alice sends the state $|\psi_{m,i}\rangle$, while Bob receives one of the possible $d - 1$ orthogonal states $|\psi_{m,j}\rangle$. Given basis m from a set of mutually

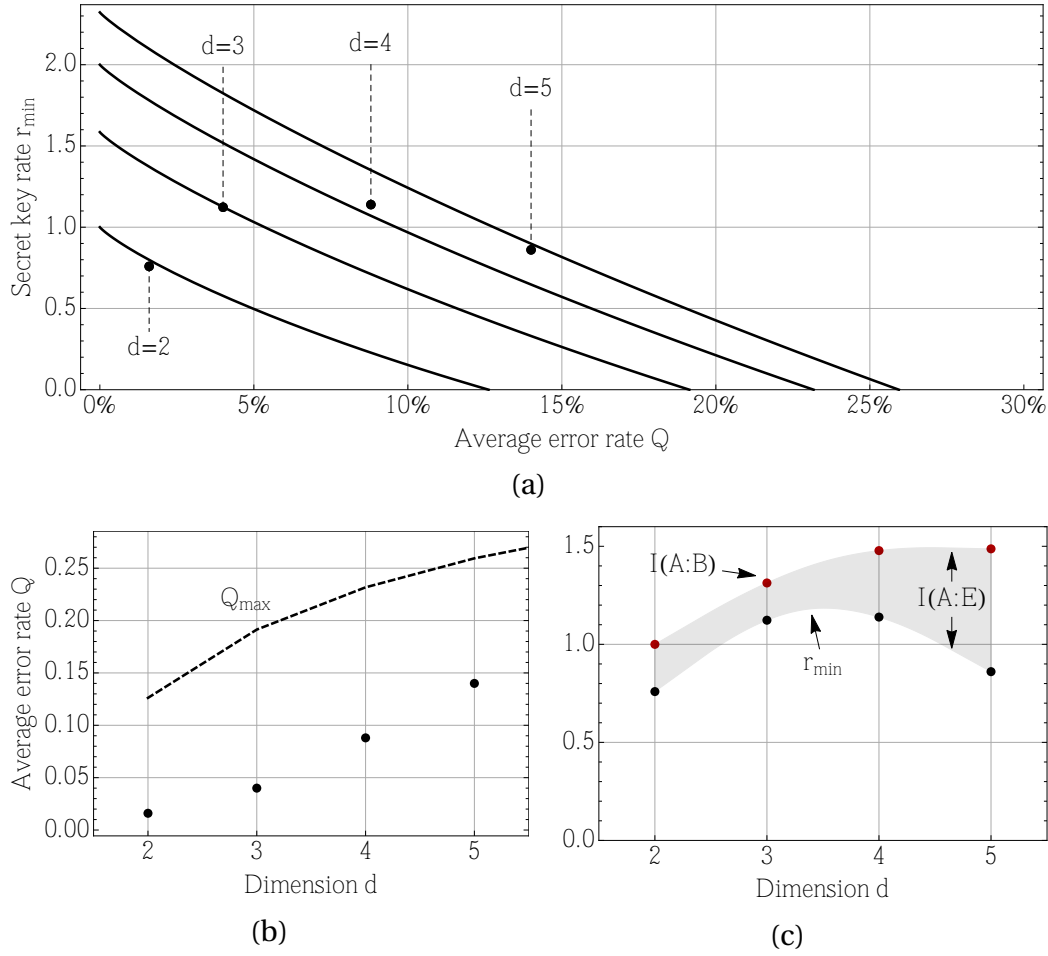


Figure 5.9: (a) Secret key rate r_{\min} as a function of the average error rate Q . The data points indicate the measured values and the curves the theoretical values calculated from eq. (5.20). (b) Measured average error rate Q and maximum permissible error rate (Q_{\max} , evaluated for $r_{\min} = 0$). (c) Shannon mutual information $I(A:B)$ and secret key rate r_{\min} , plotted as a function of d . The shaded region denotes the mutual information between Alice and Eve.

unbiased bases, the corresponding average error rate Q_m is expressed as

$$Q_m = \sum_{i \neq j} \text{Tr} \left[|\psi_{m,i}^*\rangle \langle \psi_{m,i}^*| \otimes |\psi_{m,j}^*\rangle \langle \psi_{m,j}^*| \rho_{AB} \right], \quad (5.18)$$

where ρ_{AB} is the density matrix of the joint two-photon state. The total average error rate Q is defined as the average over the M different MUB employed [99]:

$$Q = \frac{1}{M} \sum_{m=1}^M Q_m. \quad (5.19)$$

If the full set of available MUB for a prime dimension is used, $M = d + 1$.

5.3.2 Secret key rate

A second important figure of merit for the performance of a QKD scheme is the secret key rate, given by the amount of information that can be securely transmitted. It is given by the number of key bits per photon securely generated and measured in the same basis by both parties. The maximum secret key rate that can be achieved is $\log_2 d$ for a d -level system, but it is affected and limited by two factors: a possible adversarial attack by Eve and the consequent error observed by Alice and Bob, which requires them to perform error correction and privacy amplification. Alice and Bob cannot therefore generate a secret key at a rate higher than [242, 99]

$$r_{\min} = \log_2 d + \frac{d+1}{d} Q \log_2 \left[\frac{Q}{d(d-1)} \right] + \left(1 - \frac{d+1}{d} Q \right) \log_2 \left[1 - \frac{d+1}{d} Q \right], \quad (5.20)$$

where Q is the average error rate from eq. (5.19). In addition to common attacks by Eve, one should also consider the fact that an adversarial attack on a key encoded in a d -dimensional state space embedded in a larger space, such as in the case of OAM, may not be detectable in the d -dimensional state space of choice. Some of the consequences of this subtler fair-sampling violation are explored in chap. 6.

In order to assess the security of a QKD scheme, the concepts of Shannon entropy, joint entropy and mutual information are employed. The *Shannon entropy* gives a measure of the uncertainty for a random variable A with alphabet

$\{a\}$, and it is defined as

$$H(A) = - \sum_{\{a\}} p(a) \log_2 p(a), \quad (5.21)$$

where $p(a)$ is the probability of outcome a . The Shannon entropy can also be expressed as the asymptotic number of bits necessary to describe a series of events, divided by the number of events. The *classical mutual information* is defined as the amount by which the Shannon entropy on A decreases when one learns about B [23], and it is a measure of the degree of correlation between Alice and Bob's data. The classical mutual information $I(A : B)$ also provides an upper bound for the secret key rate:

$$I(A : B) = H(A) + H(B) - H(A, B), \quad (5.22)$$

where $H(A, B)$ is the *joint entropy*. The joint entropy is used to measure the total uncertainty for the pair (A, B) . It is expressed as

$$H(A, B) = - \sum_{\{a\}} \sum_{\{b\}} p(a, b) \log_2 p(a, b). \quad (5.23)$$

The quantum mutual information, or von Neumann mutual information, is the quantum-mechanical analogue of the Shannon mutual information.

The effective secret key rate is then given by the difference between the mutual information shared by Alice and Bob and the information shared by Alice and Eve, as expressed by the quantum mutual information, also referred to as the Holevo quantity [238]. The Holevo quantity measures the amount of information on Alice's bits that Eve acquires, as she interacts with the signal directed to Bob. The secret key rate can be expressed as

$$r = I(A : B) - \chi(A : E), \quad (5.24)$$

where $I(A : B)$ is the classical mutual information of Alice and Bob's data, and $\chi(A : E) = H(A) - S(E) - S(A, E)$ is the quantum mutual information between Alice and Eve. H and S are commonly used to denote the Shannon entropy and von Neumann entropy, respectively. The security assessment here presented

does not consider any specific possible attack strategy by Eve, which may affect the average error rate and therefore the effective secret key rate.

After data-processing, Alice and Bob map their respective data to raw keys K and K' . In this step, the total probability distribution remains unchanged but the total classical mutual information changes to $I(A' : B)$, which is expressed as

$$I(A' : B) = H(A') + H(B) - H(A', B). \quad (5.25)$$

The limit on the tolerable error rate that is safe for secret key generation can be improved by implementing a full set of $d+1$ MUB [99, 68]. This happens at the cost of reducing the transmission rate, which is proportional to the probability $1/(d+1)$ that Alice and Bob choose the same basis. In a protocol that makes use of the asymmetric basis choice, however, one does not pay the high cost of sifting with MUB [169]. In order to calculate the maximum tolerable error rate, Q_{\max} , the secret key rate, r_{\min} , is set to zero.

5.3.3 Experiment and result

An experiment was performed in which the dimension d was increased, in order to increase both the secret key rate and the Shannon mutual information. The improvement of these two figures of merit resulted, respectively, in higher key generation rates and higher information capacity. The experiment was carried out by Andrew Forbes and co-workers [171], using a system functionally and technically equivalent to that presented in fig. 2.5.

For each combination of projective measurements performed by Alice and Bob in the EB scheme, single count rates and coincidence count rates were recorded and the normalized joint probabilities calculated for $d = 2, 3, 4$ and 5 (as shown in fig. 5.6 for the quantum state tomography experiment). The average error rate Q was calculated from the normalized joint probabilities according to eq. (5.19). For $d = 2, 3, 4$ and 5 , the average error rates were found to be $Q = 0.016, 0.040, 0.088, \text{ and } 0.14$. Using these values of Q , together with eq. (5.20), the secret key rates were calculated to be $r_{\min} = 0.7590, 1.123, 1.139$ and 0.8606 , respectively. Fig. 5.9a shows the measured secret key rates plotted as

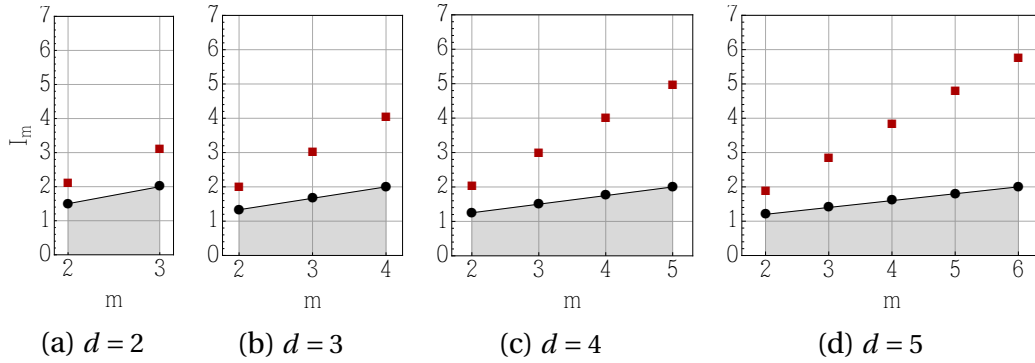


Figure 5.10: Mutual correlation I_m , for dimensions $d = 2$ to 5, and a number of MUB from 2 to $d + 1$ for each dimension considered. The red squares are experimental points corresponding to the data presented in fig. 5.6, the black points define the bound given by eq. (5.34) as $1 + (m - 1)/d$. The grey region corresponds to separable states. Uncertainties for I_m are between 0.018 and 0.032 and therefore not visible in the plots.

a function of the measured average error rates. For each curve, the intersection with the horizontal axis $r_{\min} = 0$ corresponds to the maximum permissible error rate Q_{\max} that guarantees the secure distribution of a secret key. Ideally, the error rate Q should be minimized in order to maximize the secret key rate r_{\min} . These results are shown in a different format in fig. 5.9b, where it is evident that all the measured error rates are well below the maximum permissible error rate.

The Shannon information for $d = 2, 3, 4$, and 5 was calculated to be $I(A : B) = 0.9999, 1.313, 1.478$, and 1.487 (red points in fig. 5.9b). While the Shannon mutual information increases monotonically, it levels off for $d = 4$ and 5. On the other hand, r_{\min} decreases for $d = 5$, indicating that a limit on the dimension in which the protocol can encode has been reached, while still resulting in higher generation rates per photon.

The difference between $I(A : B)$ and r_{\min} is the mutual information between Alice and Eve (grey shaded region in fig. 5.9b). From these results, it is evident that the noise introduced by a disturbance by Eve grows faster than the correlations between Alice and Bob and can thus be used to generate a key. This however is not expected theoretically and may be due to the complexity associated with encoding higher-dimensional states holographically on spatial light modulators with finite resolution.

5.4 Entanglement detection with mutually unbiased bases

The concept of mutually unbiased bases can also be linked with the problem of separability. A separable state can be expressed as a probability distribution over uncorrelated product states. By relying on the maximum complementarity of the associated observables, the properties of MUB can be used to define robust entanglement criteria for arbitrary multipartite high-dimensional systems, for both discrete degrees of freedom and continuous variables.

One such criterion, introduced by Hiesmayr and co-workers in 2012 [245], is applicable to both prime and non-prime dimensions and, therefore, to both complete and non-maximal sets of MUB. The entanglement detection scheme can be summarized as follows. In a bipartite system, for any two observables a and b defined on subsystems A and B respectively, $P_{ab}(i, j)$ is the joint probability that a has outcome i and b has outcome j . The *mutual predictability* is then defined as

$$C_{ab} = \sum_{i=0}^{d-1} P_{ab}(i, i). \quad (5.26)$$

The labelling of the outcomes $\{i\}$ corresponds to a choice of measurement bases. If observables a and b can be shown to be fully correlated for at least one labelling, $C_{ab} = 1$. If however they are fully uncorrelated, for any labelling we get $C_{ab} = 1/d$.

For a bipartite system with density matrix ρ , such as the one so far examined, the probability P_{ab} can be expressed as

$$P_{ab}(i, j) = \langle i | \langle j | \rho | i \rangle | j \rangle, \quad (5.27)$$

from which:

$$C_{ab} = \sum_{i=0}^{d-1} \langle i | \langle j | \rho | i \rangle | j \rangle. \quad (5.28)$$

An entangled bipartite state can be expressed in the orthonormal Schmidt bases

of its subsystems, as

$$|\psi\rangle = \sum_{i=0}^r \lambda_i |i_a^s\rangle |i_b^s\rangle, \quad (5.29)$$

with $r \leq r \leq d-1$. For observables a and b corresponding to these bases, one always obtains $C_{ab} = 1$, as it is also the case for a classically correlated separable state. Therefore, to detect entanglement, the state has to be measured in at least two bases, that shall be taken to correspond to observables a, b, a' and b' .

The treatment for d -level bipartite system proposed by Hiesmayr and co-workers in ref. [245] will be outlined here. If both parties measure their respective subsystems of a pure product state given in an arbitrary basis $\{|i_1\rangle\}$

$$\rho_p = |0_1\rangle |0_1\rangle \langle 0_1| \langle 0_1| \quad (5.30)$$

in the same basis $\{|i_1\rangle\}$, they will obtain $C_{1,1} = 1$. For a second basis $\{|i_2\rangle\}$ taken to be mutually unbiased with the first, they have

$$\begin{aligned} C_{2,2} &= \sum_{i=0}^{d-1} P_{2,2}(i, i) = \sum_{i=0}^{d-1} \langle i_2 | \langle i_2 | \rho_p | i_2 \rangle | i_2 \rangle \\ &= \sum_{i=0}^{d-1} |\langle i_2 | 0_1 \rangle|^2 |\langle i_2 | 0_1 \rangle|^2 = \sum_{i=0}^{d-1} \left(\frac{1}{\sqrt{d}} \right)^2 \left(\frac{1}{\sqrt{d}} \right)^2 = \frac{1}{d}. \end{aligned} \quad (5.31)$$

For the two mutually unbiased measurement bases considered so far, the *mutual correlation* I_m is defined as

$$I_2 = C_{1,1} + C_{2,2} \quad (5.32)$$

and, for a pure state, it takes the value $I_2 = 1 + 1/d$. In the general case where m different MUB are employed,

$$I_m = \sum_{k=1}^m C_{kk} = 1 + \frac{m-1}{d}, \quad (5.33)$$

since, when the mutual predictability C_{ab} corresponds to 1 in one basis, it takes the value $1/d$ in the other $m-1$ bases. Consequently, the following upper bound

for separable states measured in m MUB can be set:

$$I_m = \sum_{k=1}^m C_{kk} \leq 1 + \frac{m-1}{d}, \quad (5.34)$$

where the inequality holds if the state is separable. For a complete set of $m = d+1$ MUB, one has:

$$I_{d+1} = \sum_{k=1}^{d+1} C_{kk} \leq 2, \quad (5.35)$$

a result that had already been obtained as an entropic uncertainty relation for MUB in [278], as a generalization of [158].

The bound was applied to the data presented in fig. 5.6. While the optimal quantum tomography scheme previously described does provide information on the entanglement of the state considered, as it allows a reconstruction of its density matrix, the entanglement detection scheme based on the mutual predictability for any number of MUB $m \geq 2$ offers a more direct and efficient method to determine whether a state is non-separable. The calculated mutual correlations I_m for $d = 2, 3, 4$ and 5 are shown in fig. 5.10. Even using just two of the available MUB in each dimension, the corresponding values of I_2 place the two-photon state produced by down-conversion well above the separable-state bound.

CHAPTER 6

Fair sampling in high-dimensional state spaces

The incompatibility between quantum mechanics and local hidden variable (LHV) theories was first highlighted by the formulation of the Bell inequality in 1964, a milestone of modern quantum theory that made possible experimental investigations of the principle of locality [33]. Such experiments have ruled out, through violations of the Bell inequality, LHV theories [105, 17, 232, 107]. At least one of two main loopholes thwart the violation of Bell's inequalities in all quantum systems. The locality loophole implies the possibility of information travelling from one particle to another, while the detection loophole, so far the more prominent one, involves measurements using less-than-optimal detectors that may not be properly sampling all particles. Most of the experiments implementing tests of Bell inequalities were performed with photons, for which perfectly efficient detection remains a challenge. To interpret violations of the Bell inequality as a demonstration of nonlocality, one has to assume some form of fair sampling, i.e. the photons detected constitute a fair sample of all the photon pairs produced by the source [107, 44]. Failure to comply with this assumption opens a detection loophole.

This chapter includes material previously published in the following paper:

- J. Romero, D. Giovannini, S. M. Barnett and M. J. Padgett, "Tailored two-photon correlation and fair-sampling: a cautionary tale", *New J. Phys.* 15(8), 083047 (2013)

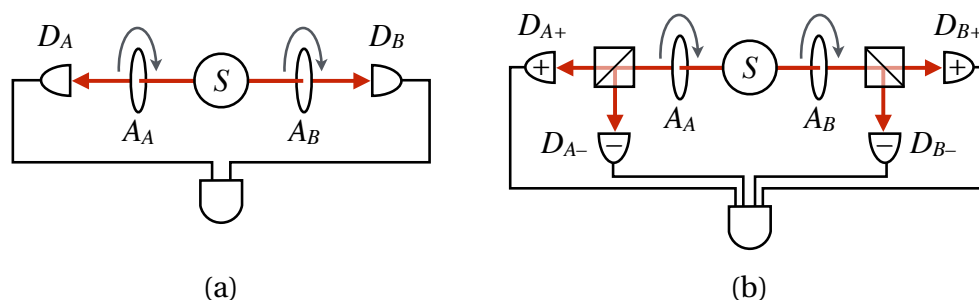


Figure 6.1: (a) Two-channel Bell experiment, as originally proposed in [33]. S denotes the source, D_A and D_B the detectors, and A_A and A_B the spatial analysers. (b) Four-channel Bell experiment, as performed by Aspect and co-workers [17].

In general, detection loopholes can be exploited to design ad hoc LHV theories that artificially violate Bell inequalities [205]. The advent of device-independent quantum protocols, where conclusions are drawn exclusively from measurement statistics, makes compliance with the fair-sampling assumption highly relevant for practical applications [2]. One option to ensure fair sampling is to use very efficient detectors that exceed the threshold efficiency needed for detection loophole-free demonstrations, thus closing the detection loophole [106, 94].

However, there are still cases when even perfectly efficient single-photon detectors do not guarantee fair sampling. As in the work presented in this chapter, a subtle choice of measurement states can in fact lead to an explicit violation of the fair-sampling assumption and a non-physical correlation curve. Correlations inconsistent with the states observed, or even with quantum mechanics, have been recorded previously in experiments with photons that fail to comply with the fair-sampling conditions. In our experiment, which used transverse spatial modes, these super-quantum correlations would persist even if the detection was made perfectly efficient. Our choice of measurement states can lead to tuneable, seemingly super-quantum violations of Bell inequalities beyond the Tsirelson bound for the system in question [71, 69], an interesting result in the context of nonlocal boxes and communication complexity [212, 56].

6.1 Fair sampling in Bell-type experiments

We focussed on the Clauser-Horne-Shimony-Holt (CHSH) inequality and its variants, which are the most tested versions of the Bell inequality [76]. The case considered is illustrated in fig. 6.1a. The basic experimental configuration involves a source of particle pairs and two spatially separated analysers (A_A and A_B) and detectors (D_A and D_B). The Bell parameter S in the CHSH inequality is derived from the correlation function, E , of observables Q_A and Q_B as a function of the settings of the analysers. Q_A and Q_B can each assume values ± 1 , which can be taken to correspond to detection or non-detection of a photon. The correlation function E as a function of analyser settings a and b in arms A and B , respectively, can be written as

$$E(a, b) = P(Q_A = Q_B | a, b) - P(Q_A \neq Q_B | a, b), \quad (6.1)$$

where $P(Q_A = Q_B | a, b)$ is the probability that $Q_A = Q_B$ for A_A set to a and A_B to b . The same goes for $Q_A \neq Q_B$ and $P(Q_A \neq Q_B | a, b)$ [236].

More intuitively, E is the difference between the probability of recording a coincidence count and the probability of not recording one, for the settings $\{a, b\}$. The Bell parameter S is defined as

$$S = |E(a, b) - E(a, b') + E(a', b) + E(a', b')|. \quad (6.2)$$

Bell's theorem states that LHV theories satisfy the inequality $S \leq 2$, for any set of orientations $\{a, b, a', b'\}$. The inequality is violated by entangled states, from which the maximum achievable value of S , $2\sqrt{2}$, can be predicted – also known as the Tsirelson bound [71]. Interestingly, the Tsirelson bound is smaller than the maximum value obtained from simple algebraic arguments, which is 4; this difference has been attributed to complementarity and compliance with information causality [71, 69, 204]. Hence, experiments which exhibit values of S beyond the Tsirelson bound would show super-quantum correlations.

Because the experiments considered can only measure count rates, probabilities are obtained by normalizing these counts. Ideally, all count rates are normalized with respect to the pair emission rate of the source, which can

be measured by event-ready detectors [286]. However, event-ready detection is prohibitive to implement, requiring, for example, two cascaded entangled photon sources in the experiment of [286]. It was not used, in particular, in the celebrated 1980s experiments by Aspect and co-workers [17], nor in the vast majority of experiments thereafter. Instead, in each arm of a source of polarization-entangled pairs, photons were sorted into two orthogonal polarizations and sent to two different detectors. This required two-fold coincidence counting on four detectors, as shown in fig. 6.1b. The correlation function can be defined in terms of the four count rates R_{ij} where $\{i, j\}$ correspond to the \pm channels, each associated with one of the two possible outcomes of each arm:

$$E(a, b) = \frac{R_{++} + R_{--} - R_{+-} - R_{-+}}{R_{++} + R_{--} + R_{+-} + R_{-+}}. \quad (6.3)$$

One can associate the first two terms to the coincidence probabilities in detectors \pm respectively, and the last two to the probability of not recording a coincidence, for settings $\{a, b\}$. In the ideal case of perfect detection, these two correlation functions are the same if the sum at the denominator of (6.3) corresponds to the emission rate of the source. Since polarization is described in a two-dimensional state space, it seems only natural for this equality to hold. In this ideal case, Clauser notes, the experiments by Aspect and co-workers were more similar to Bohm's thought experiment [47] and therefore closer to the original idealized experiment considered by Bell in his 1964 paper [73, 33].

For (6.3) and (6.1) to be considered equivalent, the detected four-fold coincidences are assumed to be a fair sample of all photons emitted by the source. Post-selection, however, is introduced: in calculating E , only the effective detected outcomes are considered. Since the total four-fold count rates could be related to the emission rate of the source in a nontrivial way, (6.3) is not necessarily equivalent to (6.1).

Resulting coincidence curves may need to be renormalized in order to show a violation of the Bell inequality [77]. In the literature, the normalization in (6.3) is referred to as the CHSH normalisation. However, as Clauser pointed out in 2002, this is "adamantly not" the 1969 CHSH normalisation [76, 73]. The difference between the two may be subtle, but nevertheless important [73, 70, 75, 81].

6.2 Synthesizing super-quantum correlations with spatial modes

In the context of our experiment, sector states were defined as equally weighted superpositions of modes carrying OAM with mutually opposite handedness. If sector states are used to perform a Bell-type experiment, the resulting coincidence curve is a sinusoidal function of the relative orientations of the sector-state analysers. When choosing appropriate superpositions of such states, arbitrary two-photon correlations can be produced. By choosing an appropriate normalization, we examined the case of a non-physical square correlation curve associated with a parameter S that violates a Bell inequality. A square wave correlation curve was here chosen as an example of super-quantum correlations as it approaches the case of a PR box [212] and can be synthesized from appropriate post-selection on a two-state system embedded in a high-dimensional space. A square wave can be approximated in terms of its first Fourier components, each of which corresponds to a sinusoidal correlation function for an odd sector state. By considering these states, we synthesized a coincidence curve that approximates a square wave using its first four Fourier components and results in a CHSH Bell parameter well beyond the upper limit of $2\sqrt{2}$ for nonlocal quantum correlations.

A common feature of all experiments that observed super-quantum correlations with photons is their failure to comply with fair sampling. In [249], for example, some of the photons were intentionally discarded, thus making the denominator of (6.3) smaller than it should be. Other schemes involved threshold detectors, amplification and fake state generation, all of which can replicate both quantum and super-quantum violations with classical light sources [211, 108]. The conceptual schematic of our experiment, however, was exactly that of fig. 6.1a, where, instead of polarization, the analysers were set to measure specific spatial modes. There was no tampering with the photon detectors or with the source. Moreover, the super-quantum Bell parameter so obtained would persist even for perfectly efficient detectors.

Transverse spatial modes of single photons carrying optical orbital angular momentum (OAM) have steadily risen as a practical degree of freedom for

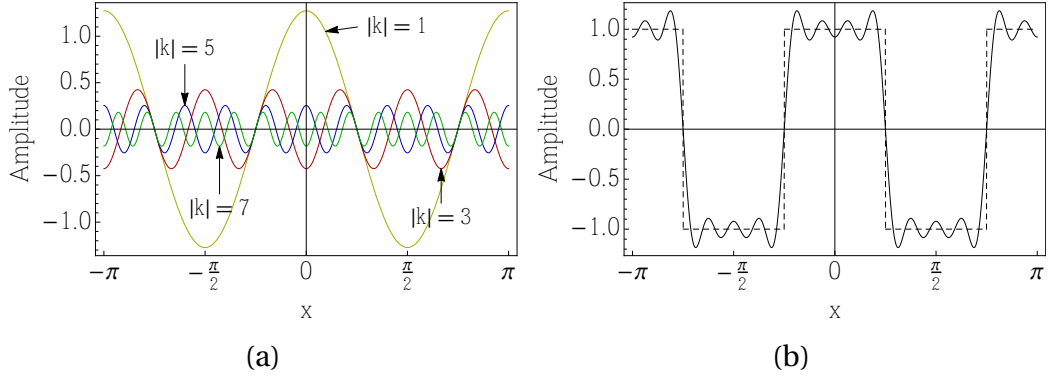


Figure 6.2: (a) A combination of sinusoidal curves with appropriate weights and odd values of k can be used to synthesize (b) a Fourier series approximation of a square wave, with x corresponding to the experimental parameter $\Delta\theta$.

observing quantum correlations. We denote a photon with OAM $\ell\hbar$ as the state $|\ell\rangle$, conveniently described by the Laguerre-Gaussian family of modes $\text{LG}_{\ell,p}$. The radial index p is here set to 0. We considered photon pairs generated via spontaneous parametric down-conversion (SPDC). As OAM is conserved in the process of SPDC [172], the general generated two-photon state $|\psi\rangle$ in the OAM basis is

$$|\psi\rangle = \sum_{\ell=-\infty}^{\infty} c_{\ell} |\ell\rangle_A |-\ell\rangle_B. \quad (6.4)$$

The quantity $|c_{\ell}|^2$ corresponds to the probability that the photon in arm A is in the state $|\ell\rangle_A$ and the photon in arm B in $|-\ell\rangle_B$. Bell tests on OAM-entangled photons have been implemented via the measurement of equal-amplitude, coherent superpositions of opposite-valued OAM modes exhibiting $|\ell|$ -fold symmetry, described by the state

$$|\alpha_{\ell}(\theta)\rangle = \frac{1}{\sqrt{2}} \left(e^{i\ell\theta} |\ell\rangle + e^{-i\ell\theta} |-\ell\rangle \right). \quad (6.5)$$

The state $|\alpha_{\ell}(\theta)\rangle$ corresponds to a $2|\ell|$ -sector state, oriented at an angle θ and characterized by $2|\ell|$ sectors of alternating 0 and π phase.

If sector states are probed in a Bell-type experiment, the resulting coincidence curve is a sinusoidal function of the relative orientations of the sector

state analysers, with a period of $2\pi/|\ell|$ [162]. The convenience of the direct relationship between ℓ and the period of the coincidence curves can be exploited, in light of the Fourier decomposition, for the synthesis of any arbitrary two-photon correlation curve by an appropriate weighting of sinusoidal curves of varying frequencies. We focus here on the case of a square wave-like coincidence curve, because, after post-selection, this gives the algebraic maximum value of $S = 4$, just as in the example presented by Popescu and Rohrlich [212].

Any function $g(x)$ with period T and frequency ω_0 can be expressed as a Fourier series [116]:

$$g(x) = \sum_{k=-\infty}^{\infty} f_k e^{i\omega_0 k x}, \quad (6.6)$$

where the coefficients f_k are given by

$$f_k = \frac{1}{\pi} \int_{-T/2}^{T/2} g(x) e^{-i\omega_0 k x} dx. \quad (6.7)$$

The exponential form of the Fourier series was chosen to highlight the similarity between a general superposition of sector states in (6.5) and the general Fourier decomposition of function $g(x)$.

For the square wave in fig. 6.2b (dashed line), $\omega_0 = 2$ and coefficients f_k are non-zero only for the odd values of k . We therefore considered the superposition of four odd sector states,

$$|\phi(\theta)\rangle = \sum_{\ell} b_{\ell} |\alpha_{\ell}(\theta)\rangle, \quad (6.8)$$

where $\{\ell\} = \{1, 3, 5, 7\}$, θ is the azimuthal angle and b_{ℓ} are complex coefficients $b_1 \simeq 0.778$, $b_3 \simeq 0.467$, $b_5 \simeq 0.389i$ and $b_7 \simeq 0.155$, found by experimental optimization. A $\pi/2$ rotation of the analyser for $|\phi(\theta)\rangle$ allows the measurement of $|\phi(\theta + \pi/2)\rangle$, which is orthogonal to $|\phi(\theta)\rangle$. For brevity, we will refer to these as $|\phi^{\perp}\rangle$ and $|\phi\rangle$, respectively.

Photon pairs were produced by pumping a 3 mm-thick β -barium borate (BBO) crystal cut for type-I collinear SPDC with a 355 nm Gaussian beam to produce entangled photon pairs at 710 nm (fig. 2.5). Signal and idler photons

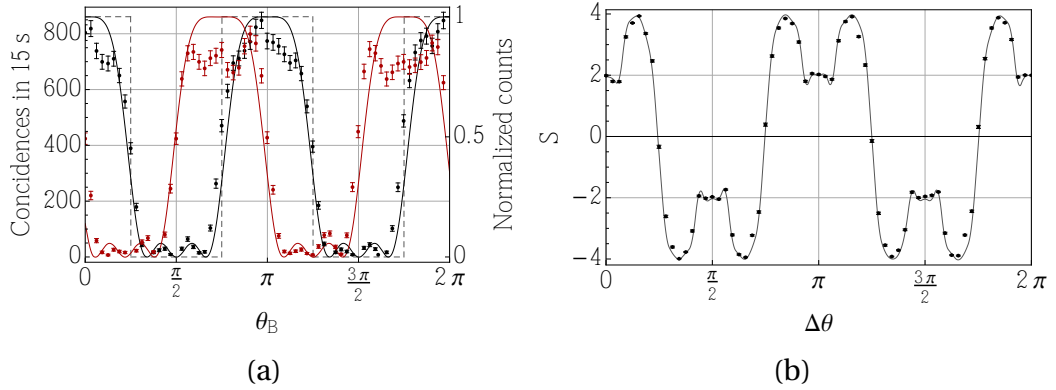


Figure 6.3: (a) Sample coincidence curves as a function of θ_B from our experiment (black and red dots) for two values of θ_A (0 and $3\pi/4$ respectively), and fit from theory (black and red lines). A square coincidence curve is also shown for reference (dashed grey line). (b) We achieved a Bell parameter S above the Tsirelson bound, using the normalization in (6.3). Our experimental values agree very well with theory (grey line), which predicts almost perfect Popescu-Rohrlich correlations with post-selection.

were separated by a beam splitter (BS) and directed to spatial light modulators (SLMs), which allowed us to measure any arbitrary superposition of OAM modes [83]. The appropriate phase and amplitude modulation for state (6.8) was encoded on the SLMs for both arms. The SLMs, used here as our analysers, were placed in the image plane of the output face of the crystal. The output of the two single-photon detectors were connected to a coincidence counting circuit, used to monitor the coincidences as a function of the modes displayed on each SLM. The accidental coincidences, typically $\simeq 5\%$ of the total counts, were subtracted from the recorded counts (eq. (3.24)).

Fig. 6.3a shows the coincidences counts as a function of the orientations θ_B of the analyser in arm B , for two orientations $\theta_A = 0$ and $3\pi/4$ of the analyser in arm A [227]. By normalizing with respect to the maximum values, we fitted our experimental coincidence curves with the expected coincidences as a function of the relative orientation $\Delta\theta = \theta_A - \theta_B$ (right scale in fig. 6.3a, solid lines). This is given by

$$C_{\text{th}}(\Delta\theta) = \left| {}_A\langle\phi(\theta)|_B\langle\phi(\theta + \Delta\theta)|\psi\rangle \right|^2, \quad (6.9)$$

assuming an ideal OAM spectrum where all the $|\ell\rangle_A|-\ell\rangle_B$ states are equally

weighted. In contrast to usual Bell-type experiments, the coincidence curve is not sinusoidal. Instead, as intended, it appears to be close to a square wave (fig. 6.3a, dashed line). Measurements were not performed with the equivalent of a polarising beam splitter for our OAM states, which would distinguish between $|\phi\rangle$ and $|\phi^\perp\rangle$. With only one detector in each arm, in order to apply the normalization (6.3) we had to measure $|\phi\rangle$ and $|\phi^\perp\rangle$ sequentially instead, as previously done in [162, 189]. With this normalisation procedure, we calculated the correlations and obtained the value of S as a function of $\Delta\theta$, showing good agreement with theory (fig. 6.3b). We obtained values of S above the Tsirelson bound for a range of $\Delta\theta$, with the maximum being $S = 3.99 \pm 0.02$, thus achieving almost perfect Popescu-Rohrlich correlation.

It should be noted that the two-photon state $|\psi\rangle$ contains all other ℓ values. However, because of the orthogonality of the OAM modes, the measurements performed were only sensitive to $\ell = \{\pm 1, \pm 3, \pm 5, \pm 7\}$. With the pump being Gaussian and the OAM spectrum centred on $\ell = 0$, the values of $|c_\ell|^2$ decrease as ℓ increases. As we are dealing with low OAM values, however, this fact does not significantly skew the experimental results, as can be seen in the comparison with the theoretical curves calculated from an ideal OAM spectrum in fig. 6.3.

Caution is therefore needed when interpreting results of Bell-type tests performed in a state space embedded in a higher-dimensional space, such as is the case with OAM. As in the experiment here presented, super-quantum correlations can be observed even in the case of otherwise perfect fair sampling. Bell tests are currently used to verify the security of quantum communication and cryptography systems; guaranteeing their reliability in the face of subtler loopholes is therefore of paramount importance, especially with the advent of device-independent quantum protocols.

6.3 Sampling high-dimensional state spaces

If the measurement states are known, it is possible to verify whether the choice of measurement states satisfies fair sampling, thus avoiding the detection loophole associated with subspaces of high-dimensional state spaces. However, if the

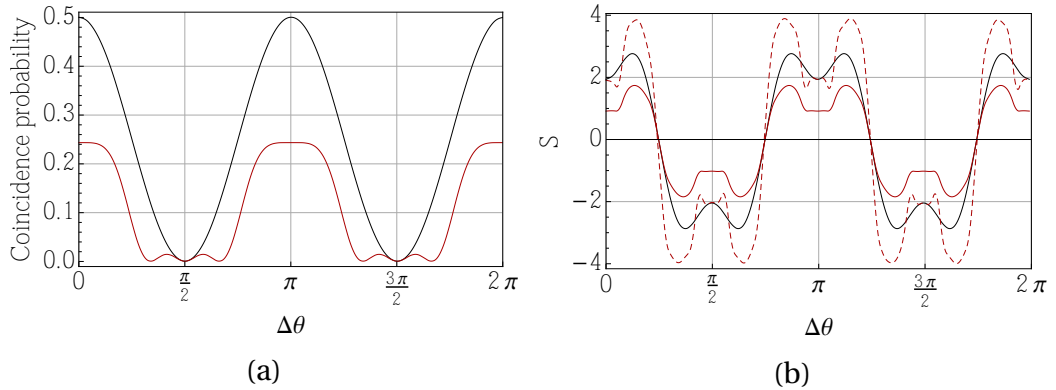


Figure 6.4: (a) Theoretical coincidence probability for our measurement settings (red line) as a function of $\Delta\theta$ is less than that of the polarization case (black line). (b) Using the correct normalization, the maximum value of S should have been 1.79 (red line), in contrast to $2\sqrt{2}$ and 3.99 for the wrong normalization (dashed red line).

experiment can be modelled as a black box and one is only presented with the resulting coincidence curve and corresponding values for S , as in fig. 6.3, they may wrongly conclude that it is a legitimate Bell experiment and the Tsirelson bound was violated. We performed a two-setting, two-outcome experiment, which corresponds to the original experiment necessary to test a Bell inequality (fig. 6.1a). As previously mentioned, the normalization (6.3) implies a dimensionality $d = 2$ for each of the two subsystems. Placing a bound on d from the measurement statistics is possible in a device-independent manner by implementing dimension witnesses [62]. This requires testing Bell inequalities formulated for higher dimensions, such as the Collin-Gisin-Linden-Massar-Popescu (CGLMP) inequality [79], which has been violated in [81].

Another way of assessing the effective dimensionality of the system is to calculate the inverse of the area under the peak-normalized coincidence curve [216, 191], as shown in chap. 4. Using this method for the coincidence curves in fig. 6.3, resulting from sector-state measurements, one obtains $d = 2.21$. Unlike the results of [191], which show parabolic coincidence fringes that immediately hint at the high-dimensional nature of the measurements space, the dimensionality here recorded is not far from the assumption $d = 2$ of eq. (6.3). It should be noted that $d = 2.21$ may not necessarily be the correct dimensionality, because of the peak-normalization involved: normalizing with respect to the maximum

recorded coincidence rate may be unjustified, when fair sampling is not satisfied. In order to realize that $d = 2.21$ may not involve the correct normalization, however, one has to recognize that the fair-sampling conditions are not satisfied in the first place.

A general CHSH-Bell experiment involves projecting onto a state $|\beta\rangle\langle\beta|$ and the orthogonal state $|\beta^\perp\rangle\langle\beta^\perp|$. The part of the Hilbert space sampled by these measurements is given by

$$\hat{H} = |\beta\rangle\langle\beta| + |\beta^\perp\rangle\langle\beta^\perp|. \quad (6.10)$$

This should be independent of the orientation of the analysers, in order for it to satisfy fair sampling [81]. For a two-dimensional Hilbert space, \hat{H} spans the whole state space, as the sum in eq. (6.10) corresponds to the identity operator $\mathbb{1}$. For example, we can consider the case of $|\alpha_\ell(\theta)\rangle$, defined previously in eq. (6.5) and used in [162], to violate a Bell inequality. The state orthogonal to $|\alpha_\ell(\theta)\rangle$ is $|\alpha^\perp_\ell(\theta)\rangle = |\alpha_\ell(\theta + \pi/2)\rangle$. One can check that, in fact,

$$\hat{H}_\alpha = |\alpha_\ell(\theta)\rangle\langle\alpha_\ell(\theta)| + |\alpha^\perp_\ell(\theta)\rangle\langle\alpha^\perp_\ell(\theta)| = |\ell\rangle\langle\ell| + |-\ell\rangle\langle-\ell| = \mathbb{1}, \quad (6.11)$$

which is independent of θ .

Calculating $\hat{H}_\phi = |\phi\rangle\langle\phi| + |\phi^\perp\rangle\langle\phi^\perp|$ for our settings, as a function of orientation θ , results in an 8×8 matrix with non-zero off-diagonal elements because the values of ℓ do not always sum to zero. Looking at the top-left corner of the matrix, one has:

$$\hat{H}_\phi = \begin{pmatrix} b_7 b_7^* & 0 & b_7 b_3^* e^{-i4\theta} & \dots \\ 0 & b_5 b_5^* & 0 & \dots \\ b_3 b_7^* e^{i4\theta} & 0 & b_3 b_3^* & \dots \\ \vdots & \vdots & \vdots & \ddots \end{pmatrix} \quad (6.12)$$

which shows a dependence on the angle θ . As we rotate our analysers, \hat{H}_ϕ changes and we are sampling a different portion of the Hilbert space. Consequently, fair sampling is not satisfied, regardless of light collection and detection efficiencies. Even if a scheme equivalent to that of fig. 6.1b was used, which

would imply the use of a perfect sorter for the two orthogonal states and perfectly efficient detectors, one would still not satisfy fair sampling because of our choice of measurement states.

The theoretical coincidence probability of our experiment (assuming an ideal OAM spectrum) is compared in fig. 6.4a to that of a Bell-type experiment for polarization, without renormalization. These curves could be derived experimentally if the pair emission rate of the source was known. The discrepancy between the maximum probability recorded in our experiment (0.24) and that of the polarization case (0.5) highlights the inherent loss due to the choice of OAM measurement settings and the fact that they are not phase-conjugates of each other, as in [162, 229]. Had the analysers been phase-conjugates of each other, the maximum probability would also have been 0.5; the shape of the coincidence curve, however, would not have been a non-physical square wave. If we follow the prescription of CHSH and use the correlation function defined in (6.1) to calculate the Bell parameter, we obtain the curves in fig. 6.4b. This gives a maximum violation for our settings of $S = 1.79$, in contrast to $S = 3.99$, obtained previously by incorrectly normalizing the count rates.

The choice of measurement states and imperfect detector efficiency introduce different losses. The latter can be accounted for without violating fair sampling, as it is in general independent of the measurement setting (e.g. the orientation of the analysers in the two-dimensional polarization case) [44]. This is not true, however, for our analysers, which act in a higher-dimensional state space: a physical rotation of the analysers does not correspond to a rotation in a given plane of the Bloch sphere spanned by states $|\psi\rangle$ and $|\psi^\perp\rangle$. This introduces an orientation-dependent post-selection, which is not immediately obvious. Moreover, our tailored coincidence curves are possible only because the two-photon OAM state space of $|\psi\rangle$ is high-dimensional. If $|\psi\rangle$ were only described by a pair of phase-conjugated OAM states, one would get the usual sinusoidal coincidence curve.

An analogous experiment could be implemented by replacing two-fold detection with a mode sorter and multiple detectors for both Alice and Bob [43]. A mode sorter arrangement able to separate and detect all the OAM states spanned by the rotation of the analysers could thus close the fair-sampling loophole here

presented.

From the point of view of nonlocality, the OAM experiment is a convenient way of implementing tuneable Popescu-Rohrlich correlations, which can be viewed as a nonlocal AND gate with the fidelity given by $F = (S + 4)/8$ [249]. We achieved fidelities as high as 99%, higher than the 90.8% upper bound above which communication complexity is trivial [249, 56].

CHAPTER 7

Extending the Hilbert space of transverse modes using the radial degree of freedom

So far, the transverse electromagnetic field of light has been described in terms of modes carrying orbital angular momentum (OAM). The family of Laguerre-Gaussian (LG) modes with no radial phase discontinuities, in particular, is especially convenient as it forms a complete orthonormal basis set of solutions for paraxial light beams and such modes can be experimentally produced and detected using a variety of methods. The OAM of photons whose states are described by LG decompositions can in addition be used in conjunction with other degrees of freedom, such as polarization or longitudinal momentum [27, 259]. Combining different degrees of freedom provides the opportunity to access larger Hilbert spaces, without the complications that arise from employing low-dimensional degrees of freedom (such as polarization) in multi-particle scenarios.

This chapter includes material previously published in the following papers:

- D. Giovannini, J. Romero and M. Padgett, “Interference of probability amplitudes: a simple demonstration within the Hong-Ou-Mandel experiment”, *J. Opt.* 16(3), 032002 (2014)
- E. Karimi, D. Giovannini, E. Bolduc, N. Bent, F. M. Miatto, M. J. Padgett and R. W. Boyd, “Exploring the quantum nature of the radial degree of freedom of a photon via Hong-Ou-Mandel interference”, *Phys. Rev. A* 89, 013829 (2014)

The ability to harness additional degrees of freedom adds power and flexibility to quantum algorithms and protocols. One such degree of freedom is the radial transverse mode of light which, together with the set of azimuthal, OAM-carrying modes with a single on-axis phase singularity, provides a complete description of the transverse field. Hong-Ou-Mandel (HOM) interference is a quintessential quantum effect and the basic constituent of many quantum protocols; the HOM interference between two photons appropriately labelled with both the azimuthal index ℓ and the radial index p can be tuned by manipulating their radial transverse modal profiles. This result points to the feasibility of single-photon utilizations of the radial degree of freedom, and allows us to extend the dimension of the accessible state space provided by transverse modes, as well as to achieve greater versatility of existing protocols and significantly increase the information channel capacity.

7.1 The radial degree of freedom

If one ignores the vectorial characteristic of a paraxial optical field, associated with its polarization, the transverse structure of the field can be decomposed into the Laguerre-Gaussian basis, whose eigenstates form a complete basis of transverse spatial modes in cylindrical coordinates. In general, Laguerre-Gaussian modes $LG_{\ell p}$ are labelled by two independent parameters, ℓ and p , which correspond to the azimuthal and radial quantum numbers [8, 142]. As radial modes with the same value of ℓ are mutually orthogonal, they provide a complete basis for the corresponding unbounded Hilbert space. Unlike OAM, however, the symmetry group associated with the radial degree of freedom of an optical field is a noncompact $SU(1, 1)$ Lie group [144]. It has been theoretically proven and experimentally verified that considering the radial degree of freedom of an entangled photon pair generated in parametric down-conversion can greatly increase the entanglement strength and lead to hyperentangled states involving both OAM and p index [234, 176]. Employing radial modes presents some difficulties not associated with OAM, the main of which is the fact that the chosen basis depends on the beam waist; an eigenstate for a specific beam waist

turns into a superposition of p modes for any other beam waist. In addition, the accurate generation of a specific $\text{LG}_{\ell p}$ is made challenging by the requirements of intensity masking, on top of the azimuthal phase dependence introduced by appropriate forked holograms, to achieve the desired amplitude distribution in the transverse field.

If one only takes into account the radial profile of the optical field, by assuming all other quantum numbers as identical whenever photon pairs are considered and taking $\ell = 0$, the field modes are exclusively labelled by the radial number p :

$$|\psi\rangle = \sum_{p=0}^{\infty} c_p |p\rangle, \quad (7.1)$$

where $|p\rangle$ stands for a radial eigenmode of radial number p . The expansion coefficients c_p are normalized to one, $\sum_{p=0}^{\infty} |c_p|^2 = 1$. Since Laguerre-Gauss modes are mutually orthogonal, we have $\langle p|p'\rangle = \delta_{pp'}$.

Some of the properties of physical systems that manifest themselves at the classical level, such as radial modes, can also be successfully used to label distinct single-photon states in the quantum regime. This feature of radial modes can be assessed in the quintessentially quantum context of Hong-Ou-Mandel interference, where any property that can help distinguish the photons leads to a positive contribution to the probability of the photons leaving from different ports of a balanced beam splitter. The quantum nature of radial modes and OAM is quite different from that of Cartesian modes such as the Hermite-Gauss set, although both describe transverse modes of optical fields. HOM interference has been shown for degrees of freedom such as wavelength [128], polarization [233], Hermite-Gaussian transverse modes [267] and OAM [184, 182]. Consequently, several quantum gates and algorithms, such as the C-NOT gate and Shor's algorithm, were proposed or demonstrated with some of the degrees of freedom just mentioned [74, 247, 151, 104], as well as the measurement of the associated parametric down-conversion spectra [87]. Moreover, correlations in radial modes of entangled photon pairs generated in down-conversion [179] have recently been explored by Löffler and co-workers [234], arousing interest in the use of this degree of freedom.

7.2 Interference of probability amplitudes in the Hong-Ou-Mandel effect

The Hong-Ou-Mandel (HOM) experiment is arguably the simplest and most elegant multi-particle interference experiment in quantum physics. In the first HOM experiment [128], each of the degenerate signal and idler photons (s and i in fig. 7.1a) produced in spontaneous parametric down-conversion (SPDC) was separately sent to an input of a beam splitter. Detectors at each of the outputs of the beam splitter then recorded the coincidence rate as a function of the relative path delay (Δz in fig. 7.1a) between the otherwise indistinguishable signal and idler photons. The coincidence rate obtained shows a minimum (referred to as a coincidence ‘dip’) when the optical paths of the signal and idler from the crystal to the beam splitter are matched to within the coherence length L of the light.

Because the dip disappears as the relative path delay is increased to the point that it becomes possible to distinguish between the signal and idler photons, it is natural to think of the dip as arising from the interference between two individual photons entering the beam splitter. However, as previous works have already highlighted [128, 156, 209], the interference in the HOM experiment is not the result of interference between two single photons, but rather the interference between probability amplitudes that describe the various alternatives that can lead to a coincidence event. In the simple arrangement of fig. 7.1a, coincidences are registered when the photons impinging on the beam splitter are either both reflected or both transmitted. It is not the indistinguishability between the individual photons that is necessary, but rather, the indistinguishability between alternatives that lead to the detectors clicking after the photons have passed through the interferometer.

The interference of probability amplitudes has been demonstrated within the Hong-Ou-Mandel experiment. In 1996, Pittman and co-workers [209] demonstrated that any path difference between the photons entering the beam splitter can actually be compensated for after the beam splitter. The HOM dip in their experiment then cannot be interpreted as the interference of the two individual photons because, for the two photons entering the beam splitter, $\Delta z \gg L$. The distinguishing information is not limited to path length. In the 1992 ‘quantum

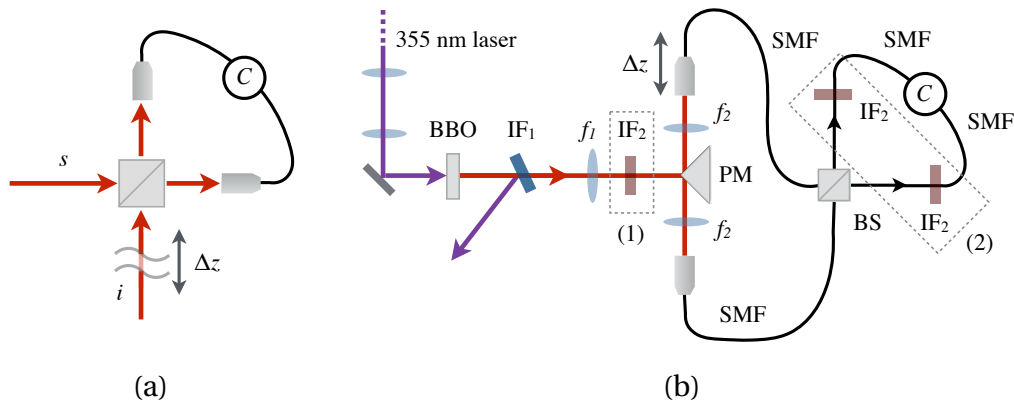


Figure 7.1: (a) Basic Hong–Ou–Mandel experiment. The signal (s) and idler (i) photons from SPDC combine in a beam splitter. When the optical path difference (Δz) between the photons is zero, the two photons in each pair are detected in the same detector, leading to a dip in the coincidence counts between the two detectors. (b) Experimental set-up. Type-I SPDC in a BBO crystal results to signal and idler photons with the same polarization; the pump residue is blocked by a longpass reflective interference filter IF_1 . These photons are separately coupled to single-mode fibres (SMFs), which are input to a fibre-optic beam splitter (BS). We considered two configurations: (1) The photons are spectrally filtered by narrow-band bandpass filter IF_2 before they combine in the beam splitter. (2) The spectral filtering is done by IF_2 filters placed just before the detectors, after the photons have combined in the beam splitter. In both cases, the coincidence count is monitored as the relative path difference (Δz) between the two photons is varied.

eraser' experiment by Kwiat and co-workers [156], one of the photons was labelled by rotating its polarization so that it was orthogonal to that of the other photon. Polarizers were then placed right before the detectors, thus showing that the visibility of the resulting dip depends on the relative orientation of the polarizers. The polarizers placed before the detectors appear to 'erase' the labelling of the photons after they have exited the beam splitter. Again, this experiment can only be interpreted in terms of exchange symmetry, with the dip being a result of the interference of indistinguishable probability amplitudes rather than indistinguishable photons. HOM-type interference has also been predicted and experimentally observed with photons that have different spectra [120, 55, 199, 222, 167].

Our experiments was simpler than the experiments previously mentioned, in that we do not try to label any of the photons combining in the beam splitter. We

simply measure the width of the HOM dip for two different narrow-bandwidth spectral filters [112]. In each case, the filter was placed before the beam splitter (before the individual photons combine) or after the beam splitter (after the photons have combined, just before they reach the detectors). For a given filter, if the HOM effect was truly due to the interference of two photons, as opposed to the interference of their probability amplitudes prior to detection, the width of the dip should be unchanged regardless of where the bandwidth filtering takes place.

The dip in the HOM experiment can be elegantly described as a result of the destructive interference of the two indistinguishable events that lead to a coincidence, i.e. when the individual photons are both reflected or both transmitted. If we let r and t be the reflection and transmission coefficients respectively, the probability of a coincidence count for a balanced beam splitter is given by

$$P_C = |r \times r + t \times t|^2 = \left| \left(\frac{i}{2} \right)^2 + \left(\frac{1}{2} \right)^2 \right|^2 = 0. \quad (7.2)$$

Indistinguishability between the alternatives leading to a coincidence is the necessary condition for complete destructive interference. In many cases, but definitely not always, this means that the photons entering the beam splitter should be indistinguishable themselves. The photons in many HOM-type experiments come from parametric down-conversion. Here, a pump photon (with frequency ω_p) incident on a nonlinear crystal decays into the signal and idler photons (with frequencies ω_s and ω_i , respectively) with a small probability. Being a parametric process, the total energy of the photons is conserved such that $\omega_p = \omega_s + \omega_i$. The fact that the pump is not perfectly monochromatic, and the phase-matching conditions due to the finite size of the nonlinear crystal, introduce a spread in the frequencies of the signal and idler photons. Hence, to ensure indistinguishability, most experiments of this type use nonlinear crystals cut for degenerate SPDC ($\omega_s = \omega_i$), and identical narrow-band interference filters centred on the degenerate frequency are introduced to ensure that the two photons have the same spectra. If we assume that the interference filters have a Gaussian profile, of standard deviation σ in frequency, the two-photon

coincidence count N_C can be approximated as

$$N_c \simeq 1 - \frac{2RT}{R^2 + T^2} \exp \left[-\frac{(\sigma \Delta z)^2}{2c^2} \right], \quad (7.3)$$

where $R = r^2$ and $T = t^2$ (the reflectivity and transmissivity of the beam splitter, respectively), Δz is the optical path difference between the two photons and c is the speed of light [200].

The interference filters can be placed before the beam splitter or after the beam splitter (e.g. right before the detectors). In the former case, the filters ensure the indistinguishability of the photons *before* they combine in the beam splitter. In the latter case, the filters are placed *after* the photons have combined in the beam splitter. This second case induces a spectral filtering after the interference of the two photons has taken place, if the two-photon HOM interference can indeed be attributed to the interference of the individual photons. However, since the HOM dip in the coincidence between the detector outputs is due to the interference of the probability amplitudes of the outcomes, the width of the HOM dip with the filters placed before the detectors or before the beam splitter is expected to be the same.

We used a 3 mm long β -barium borate crystal (BBO) cut for type-I degenerate, collinear SPDC (fig. 7.1b) producing signal and idler photons having the same polarization. To minimise background counts, a longpass interference filter (IF₁) blocks the pump beam after the BBO crystal. The 710 nm down-converted photons were focussed by a lens (f_1) onto a knife-edge prism mirror (PM) aligned such that the signal and idler photons are directed to the facets of separate polarization-maintaining single-mode fibres. One of the fibres was mounted on a translation stage that allowed us to match the path lengths of the signal and idler photons. For ease of alignment, we employed a balanced fibre-coupled beam splitter, which consists of a 50/50 beam splitter connected to two polarization-maintaining input single-mode fibres and two output single-mode fibres. The signal and idler photons entered the beam splitter via the input fibres. Interference filters (IF₂) centred at 710 nm were used to select the signal and idler photons.

We considered two cases. In the first case, a filter (IF₂) was placed just before

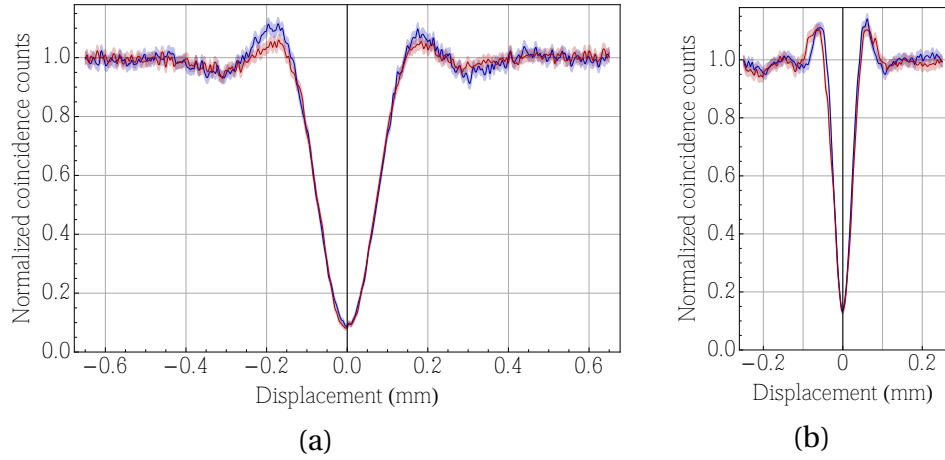


Figure 7.2: The Hong-Ou-Mandel dips in the experiment are the same regardless of where the interference filter is placed. (a) HOM dip for a 2 nm filter placed before (blue) and after (red) the beam splitter. Coincidence counts for each position were recorded over 4 s. Coincidence counts for completely distinguishable photon pairs are 2500 s^{-1} , with average single-channel counts of 70000 s^{-1} and approximately 1000 s^{-1} dark counts. (b) HOM dip for a 10 nm filter placed before (blue) and after (red) the beam splitter. Coincidence counts for each position were recorded over 2.5 s. Coincidence counts for completely distinguishable photon pairs are 3600 s^{-1} with average single-channel counts of 163000 s^{-1} . The width of the dip is inversely proportional to the bandwidth of the filter. The shaded regions about the trace denote the uncertainty. The uncertainty in the relative path difference is set by the stage and it corresponds to $0.055 \mu\text{m}$.

the mirror, thus making the spectra of the two photons identical before the photons reach the beam splitter. The fibres at the output ports of the beam splitter were then fed directly to avalanche photodiodes that served as single-photon detectors. In the second case, no filter was present before the beam splitter apart from IF_1 ; instead, each of the fibres at the output port of the beam splitter was connected to a short free-space fibre coupler which held one of an identical pair of interference filters (IF_2). The output of each fibre coupler was then sent to a single-photon detector. The outputs of the detectors were in both cases sent to a coincidence circuit, which allowed to monitor the coincidences as the position of the translation stage was scanned.

Given the different efficiencies of the two configurations, each set of coincidence counts was normalized with respect to the constant coincidence count observed for $\Delta z \gg L$. Fig. 7.2 shows the normalized coincidences as a function

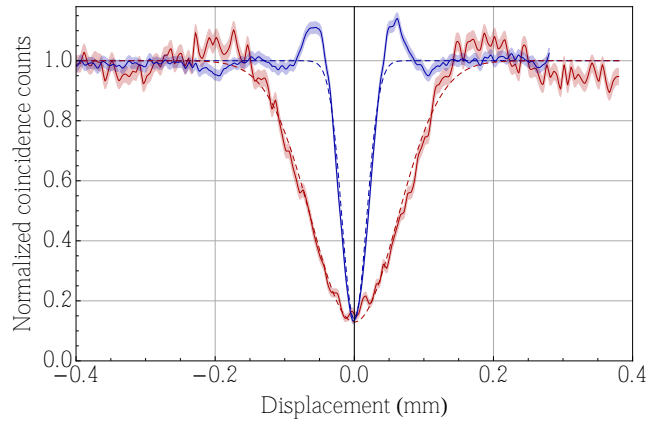


Figure 7.3: Hong-Ou-Mandel dips for filters with different bandwidths placed before and after the beam splitter. The width of the HOM dip when a 10 nm filter is placed before and a 2 nm filter is placed after the BS (red) is wider than the HOM dip that results from having just a 10 nm filter before the BS (blue). The FWHM for the former case is $146.0 \mu\text{m}$, closer to the FWHM of an HOM dip resulting from a 2 nm filter (fig. 7.2b). The shaded regions denote the uncertainty. The Gaussian curves shown come from least-squares fits.

of the relative path difference Δz of the signal and idler photons, for two bandpass filters with different widths. Fig. 7.2a shows the coincidences for a 2 nm filter placed before (blue) and after (red) the beam splitter. Fig. 7.2b shows the coincidences for analogous placements of a 10 nm filter. As expected, we found a minimum in the coincidences for $\Delta z = 0$. The results show that, regardless of the position of the filter with respect to the beam splitter, the shape and width of the HOM dip remains the same. The full width at half maximum (FWHM) of the dip for a 2 nm filter placed before or after the beam splitter is $141.5 \pm 1.2 \mu\text{m}$ and $142.2 \pm 0.8 \mu\text{m}$ respectively. As evident from eq. (7.3), the width of the HOM dip is inversely proportional to the width of the interference filter. A narrower dip is therefore expected for the 10 nm filter. The FWHM for a 10 nm filter placed before and after the beam splitter is $41.7 \pm 0.5 \mu\text{m}$ and $46.6 \pm 0.6 \mu\text{m}$ respectively. These values were calculated from a least-squares Gaussian fit of the data in fig. 7.2. The actual shape of the HOM dip can be fully described by considering the spectrum of the two-photon state, to which the dip shape is related by a Fourier transform. The spectrum of the photon pair is here determined by the bandpass filters inserted in the system. Were the bandpass filters ideal, with a

perfectly rectangular frequency response, the dip would then assume the shape $\sin(\Delta z)/\Delta z$. For the filters used in the experiment, however, a Gaussian curve provides an excellent approximation. Because the HOM interference arises from an interference of probability amplitudes, rather than from the interference of individual photon pairs at the beam splitter, the width of the HOM dip is expected to be the same regardless of the position of the interference filters, as supported by the experimental results.

We also considered the case where the filters placed before and after the beam splitter have the same central wavelength but different bandwidths. A 10 nm filter was placed before the beam splitter and 2 nm filters after. The result is shown in fig. 7.3. We compared the resulting HOM dip from this case (red) to the earlier result that employed just a 10 nm filter before the beam splitter (blue). If the interference were due to the individual photons that have passed through the 10 nm bandwidth filters before reaching the beam splitter, one would expect the width of the resulting HOM dip (red) to be unaffected by the 2 nm filter. The width of the dip will be the same as that of the blue curve, but with reduced coincidences due to the presence of the the 2 nm filters, which limit the number of photons that reach the detectors. This is not what one can observe in the experiment: the red curve is wider, with a FWHM of $146.0 \pm 3.0 \mu\text{m}$, similar to the FWHM of the HOM dip when only the 2 nm filter was present. The 2 nm filter placed after the beamsplitter seems to ‘retroactively’ alter the width of the coincidence dip, *after* the individual photons have interfered, if one subscribes to the most simplistic interpretation of the phenomenon.

This result highlights how the interference resulting to the HOM dip is not simply an interference of the input photons. The fact that the width of the dip appears to be affected by the 2 nm filters placed just before the detectors supports the notion that it is the interference of the probability of the outcomes that leads to the HOM dip. The width and shape of the HOM dip are determined by the filter with the narrowest bandwidth, regardless of where that filter is placed.

7.3 Exploring the quantum nature of the radial degree of freedom

In order to study the properties of radial modes in a single-photon context and show their potential for quantum applications, we employed Hong-Ou-Mandel interference. An experiment was carried out in the laboratories of the University of Ottawa, in collaboration with Robert Boyd's research group [143]. In the experiment, we prepared photons pairs in a down-conversion process. A frequency-tripled quasi-CW mode-locked Nd-YAG laser (repetition rate of 100 MHz and average output power of 150 mW at 355 nm) was used to pump a 3 mm thick nonlinear BBO crystal cut for type-I phase matching in a near-collinear regime to generate identical photon pairs with degenerate frequency of $\lambda = 710$ nm. The signal and idler photons so generated were each coupled into one of two identical single-mode optical fibres, which selected the fundamental transverse spatial mode. The fibres were then directed to the main part of the experimental set-up, where the HOM interference was tested (fig. 7.4).

After the fibres, any spatial entanglement between the two photons was erased but the photons remain synchronized in time. The radial modes of signal and idler, initially a Gaussian mode with waist $w_0 = 954 \mu\text{m}$, were reshaped by computer-generated holograms of 1920×1080 pixels displayed on two Holoeye Pluto spatial light modulators. An overall quantum efficiency of 20% with a coincidence rate of 37 kHz was obtained by splitting the photon pairs with a knife-edge prism mirror (PM) prior to the coupling into the SMFs. The polarization shift of signal and idler induced by the fibre propagation was compensated for by a combination of quarter-wave and half-wave plates, also used to rotate the polarization of the incoming photons to match the working polarization of the SLMs, i.e. the polarization that provides the maximum diffraction efficiency.

The desired modes generated at the first order of diffraction of the blazed holograms shown on the SLMs were then sent into a balanced nonpolarizing beam splitter (BS_1). Its output were coupled to low-mode optical fibres (MMFs) with a core size of $10 \mu\text{m}$, after being spectrally filtered by an interference filter with bandwidth 10 nm. Photon pairs were detected by two silicon avalanche photodiodes, connected to a data acquisition card that recorded photon counts

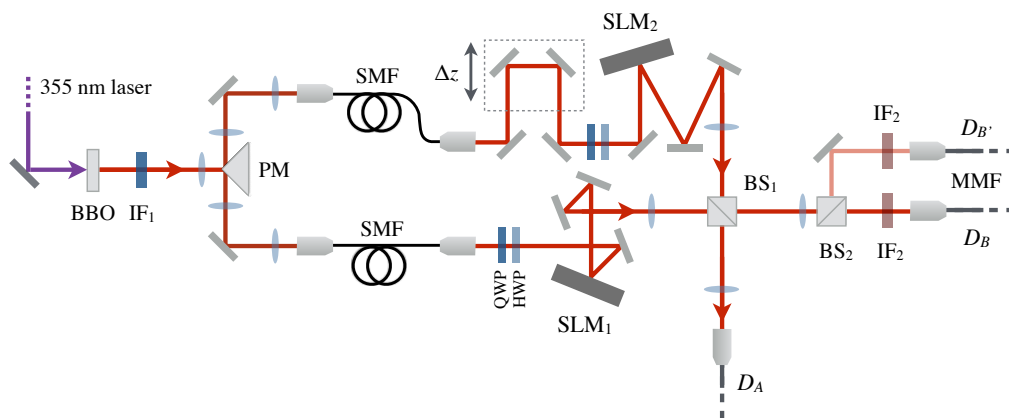


Figure 7.4: The photon pairs generated via spontaneous parametric down-conversion are made indistinguishable in all internal degrees of freedom by being coupled to SMFs, where only the Gaussian transverse mode is selected. They are then sent to the main apparatus in order to demonstrate the HOM interference. A quarter-wave (QWP) and half-wave (HWP) plates are used to compensate and rotate the polarization state of both signal and idler photons to horizontal (suitable to obtain a maximum efficiency at the spatial light modulators). Appropriate kinoforms are displayed on both spatial light modulators, SLM_1 and SLM_2 , to manipulate the radial DOF of the two photons and to render them completely indistinguishable, partially distinguishable or completely distinguishable. The insets near the SLMs show two possible types of holographic kinoforms. The two photons interfere on a 50:50 symmetric nonpolarizing beam splitter (BS). Then, they are collected by low-mode optical fibres coupled to single-photon counting modules (D_A and D_B), and detected in coincidence. In order to check the HOM coalescence enhancement, an additional non-polarizing BS is inserted in arm B, and the coincidence counts are read between detectors D_B and $D_{B'}$.

and coincidences between the signal and idler detectors with a detection window of 25 ns. A tunable free-space delay line, controlled by a computer-controlled movable stage with a step size of $1 \mu\text{m}$, was used to synchronize the arrival time of the photons at the beam splitter and thus tune the temporal distinguishability.

Two tests of indistinguishability were performed. The first involved the traditional visibility measurements of HOM interference, and the second what we termed coalescence enhancement, an additional that is performed to verify the quality of the interference. While two completely distinguishable photons do not coalesce at a balanced BS and one-fourth of the times leave the BS together from a specific port, in a configuration including a second beam splitter BS_2 (right-hand side of fig. 7.4) two indistinguishable photons leave this BS from

the same port together half of the times. Therefore, the coincidence counts recorded by D_B and $D_{B'}$ after the photons pass through the second BS will double. In general, the enhancement C satisfies $1 \leq C \leq 2$ and is a function of the distinguishability of the photons.

As a first step, the two MMFs were replaced with single-mode fibres and a standard HOM dip between two Gaussian photons was observed with a visibility of 0.987. With MMFs, due to non-perfect mode post-selection, a visibility of 0.725 was achieved within the same set-up. The visibility value was improved to 0.800 by setting up apertures at the far field of the MMFs, that is at the planes of the SLMs, in order to emphasise how the indistinguishability can be recovered by spatial filtering. Nonetheless, the coalescence enhancement was sufficiently close to the maximum theoretical value, and as such it provides an indistinguishability test less affected by dark counts and experimental imperfections.

The combinations of wave plates and SLMs manipulate the signal and idler photons and their transverse modes so that they become effectively indistinguishable in all degrees of freedom except for the radial one, which we can adjust to be identical, partially different or completely orthogonal. As previously mentioned, the radial states of each of the two photons, in general, are

$$|\psi_s\rangle = \sum_{p=0}^{\infty} c_p^s |p\rangle \quad (7.4a)$$

$$|\psi_i\rangle = \sum_{p=0}^{\infty} c_p^i |p\rangle \quad (7.4b)$$

respectively, where c_p^s and c_p^i coefficients determine the distinguishability of the photons. The two states are taken to be completely factorable after the spatial filtering that takes place in the input single-mode fibres. They are indistinguishable if the overlap of the two satisfies $\langle \psi_s | \psi_i \rangle = 1$ and, conversely, they are entirely distinguishable if $\langle \psi_s | \psi_i \rangle = 0$. Partial distinguishability is expected for a partial overlap between the two states. For instance, a state with only the $p = 0$ component (a Gaussian state) is orthogonal to any superposition that has no $p = 0$ component.

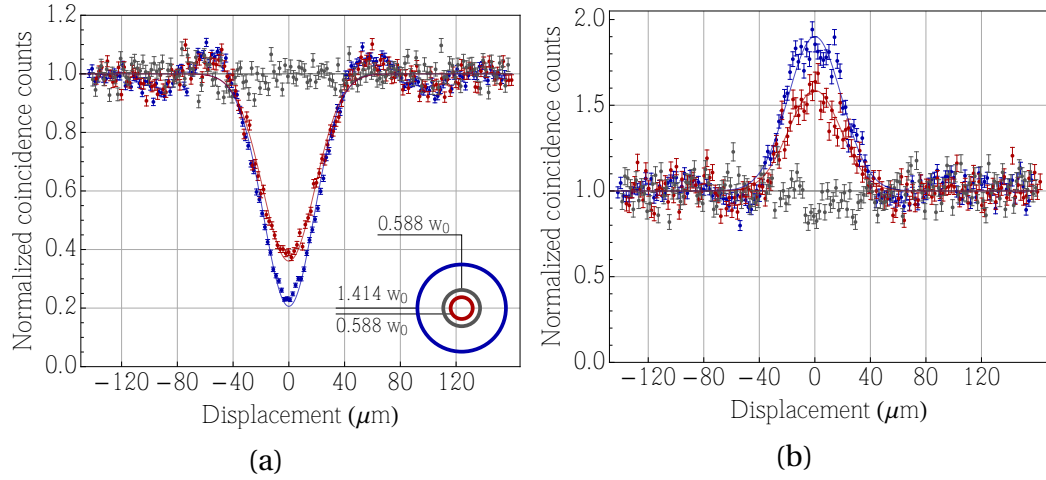


Figure 7.5: (a) Experimental data of the Hong-Ou-Mandel interference in the radial degree of freedom (coincidence detection with D_A and D_B). The HOM dip shows indistinguishability between the two photons; the flat data (grey) corresponds to two completely distinguishable radial states, while the other two curves correspond to partially distinguishable and completely indistinguishable radial states. The visibilities of the dips are $V = 0.014 \pm 0.027$, 0.465 ± 0.030 and 0.646 ± 0.026 respectively. The inset shows the radius of each holographic kinoform displayed on the SLM which determined the value of the distinguishability. (b) Experimental data of the Hong-Ou-Mandel coalescence enhancement (coincidence detection with D_B and $D_{B'}$). The enhancement increases for photons indistinguishable in the radial degree of freedom. The enhancements due to coalescence are $C = 1.113 \pm 0.093$, 1.590 ± 0.060 and 1.907 ± 0.047 respectively. The error bars correspond to one standard deviation and were calculated from a Poisson distribution. Coincidence counts were recorded over 100s in both cases. Solid curves are the best theoretical Gaussian fits. Note that the normalization factors for (a) and (b) are different.

Generating a beam in a specific radial mode, or superposition of radial modes, with efficient phase-only SLMs requires intensity masking. The intensity mask only employs part of the SLM surface, in order to diffract the excess power across the desired mode into the first order. While this allows a versatile and flexible use of the SLMs for the control of the full transverse field, the count rates decrease linearly with the extent of the surface undergoing intensity masking, thus affecting the coincidence count rate quadratically. In order to improve on the hologram encoding used to far, in the first part of the experiment a different type of holographic phase-only kinoform that uses the whole SLM surface was introduced. As a consequence, the coincidence rate was kept constant during

ρ_0	$ c_0 ^2$	Theoretical C	Experimental C
0.000	1.000	$C = 2.00$	$C = 1.973 \pm 0.051$
0.353	0.310	$C = 1.69$	$C = 1.590 \pm 0.060$
0.588	0.000	$C = 1.00$	$C = 1.113 \pm 0.093$
1.414	0.928	$C = 1.92$	$C = 1.907 \pm 0.047$

Table 7.1: Theoretical value of expansion coefficients c_0 , and theoretical and experimental HOM enhancements for various values of the circle radius ρ_0 .

all experimental tests. The kinoforms contain a blazed grating with a centred disk of radius ρ_0 , which introduces a π phase shift with respect to the remaining surface. The first-order diffracted mode from a Gaussian beam incident on such a kinoform is given by

$$\mathcal{E}(\rho) = \sqrt{\frac{2}{\pi}} e^{-\rho^2} \times \begin{cases} -1 & \text{for } \rho < \rho_0 \\ +1 & \text{for } \rho > \rho_0. \end{cases} \quad (7.5)$$

The beam can then be expanded in the LG basis with fixed ℓ , in this case $\ell = 0$: $\mathcal{E}(\rho) = \sum_{p=0}^{\infty} c_p(\rho_0) \text{LG}_p(\rho)$, where we omit the azimuthal index. The LG_p modes in the dimensionless coordinate at the pupil are

$$\text{LG}_p(\rho) = \sqrt{\frac{2}{\pi}} e^{-\rho^2} L_p(2\rho^2), \quad (7.6)$$

where L_p are the Laguerre polynomials of order p .

The expansion coefficients can be calculated by taking

$$c_p(\rho_0) = 2\pi \int_0^{\infty} d\rho \rho \text{LG}_p^*(\rho) \mathcal{E}(\rho) \quad (7.7)$$

and are given by

$$c_p(\rho_0) = 4\rho_0^2 {}_1F_1(p+1, 2, -2\rho_0^2) - \delta_{p,0} \quad (7.8)$$

where ${}_1F_1$ is a hypergeometric function. The disk radius ρ_0 can be adjusted such that the Gaussian component of the diffracted beam is entirely suppressed, which happens at $\rho_0 \simeq 0.588w_0$. We made the photon pairs completely distin-

guishable by displaying a diffraction grating on SLM₁ and a kinoform with a π phase jump at radius $\rho_0 \simeq 0.588w_0$ on SLM_B (grey data points in fig. 7.5a). In this situation, the photon pairs do not interfere, and the coincidence counts are effectively constant as a function of the trombone displacement, which yields a visibility of the HOM dip of $V = 0.014 \pm 0.027$. Correspondingly, no coalescence enhancement was observed between detectors D_A and D_B , placed after the first beam splitter (grey data points in fig. 7.5b).

After having labelled the signal and idler quantum states using their radial modes, we further increased the distinguishability of the two photons by changing the radial position of the π step on the SLM to $\rho_0 = 0.353w_0$ and $\rho_0 = 1.414w_0$, and measured corresponding visibilities of $V = 0.465 \pm 0.030$ and 0.646 ± 0.026 , and coalescence enhancements of $C = 1.590 \pm 0.060$ and 1.907 ± 0.047 (fig. 7.5). Expected theoretical and observed coalescence enhancements and the first-order expansion coefficient c_0 for different values of circle radius are shown in tab. 7.1.

We then observed the HOM interference between two identical spatial modes with no Gaussian component. A coalescence enhancement of $C = 1.946$ was observed, which shows an excellent indistinguishability between two photons with identical superpositions of $p \geq 1$ modes. This last test was performed using a large portion of the Hilbert space of the radial degree of freedom. Imperfections in the system, such as aberrations in the SLMs, alignment, dark count and thermal drift prevented the minimum of the coincidence dip to reach exactly zero. The limited sizes of the apertures in the system, mainly the microscope objectives and the effective limited active areas on the SLMs, also affect the radial states examined.

The mutual orthogonality of the radial modes associated with indices p_s and p_i was examined by implementing intensity-masked holograms in both arms, in order to generate different radial eigenmodes with very good approximation. The overall fidelity of the generated states, however, is bounded by the pixel size, the active area on the SLM and the SLM gamma function modulation (which mediates the conversion of greyscale pixel data to pixel voltages). Despite these limitations, a fidelity of about 98% was observed in previous work [82]. In this case, low-mode optical fibres at the detection stage (D_A and D_B) were replaced

with multimode optical fibres with core size $200\ \mu\text{m}$, which support a wider range of spatial modes. The observed visibility of the dip obtained for radial modes from $p = 0$ to 9 ranged from 62% to 32%. The effects introduced by the experimental limitations previously listed were made in this case more prominent by the necessary use of large-core multimode fibres.

CHAPTER 8

Conclusions

Considerable interest has been shown in the generation and manipulation of light carrying OAM, for the effective production of high-dimensional entangled states and quantum information purposes. In this thesis, entanglement in the unbounded discrete state space of the orbital angular momentum of light was explored. A series of experiments were performed to study high-dimensional states produced by parametric down-conversion, entangled in OAM and its conjugate variable, angular position, which is continuous and periodic. By considering both variables we were able to produce experimentally a considerable widening of the spiral bandwidth, defined as the correlation spectrum of accessible OAM modes produced by down-conversion. A wider spiral bandwidth, and correspondingly narrower angular correlations, were produced by carefully tuning the phase-matching conditions of down-conversion and designing a versatile adaptive-optics detection system able to perform measurements over a large range of OAM-carrying transverse modes. The observation of both conjugate variables allowed us to describe not just the correlation spectrum, but also characterize the entanglement of the high-dimensional states so produced.

We have shown how the size of the spiral bandwidth can be affected by appropriately tuning the ratio of pump width and detection-mode widths, and the crystal thickness divided by the Rayleigh range of the pump. An appropriate choice of these parameters, coupled with the convenience of spatial light modulator-based measurements, allowed us to produce and detect correlations consistent with a bi-photon state entangled in over thirty OAM modes, as well as

angular position correlations compatible with the Fourier relationship between angle and OAM. These correlations can also be tailored by manipulating the pump beam used in down-conversion. We showed how the OAM spectrum of a pump prepared in a superposition of transverse modes can be transferred to the down-converted fields; their OAM and angular position correlations were studied using the same techniques previously introduced.

A different method to determine the dimension of a two-photon state entangled in multiple OAM modes, based on the same experimental techniques, was also presented. Using complex superpositions of several OAM modes encoded in phase-only masks, we were able to effectively determine the effective detected dimension of the down-conversion state without resorting to a series of measurements in each of the states of interest. These masks were used to measure a Schmidt number of about fifty. Similar holograms, prepared for superpositions of full sets of mutually unbiased bases of Laguerre-Gaussian modes in d -dimensional subspaces of the OAM degree of freedom, were also experimentally implemented. As a full set of mutually unbiased bases provide exactly the minimum number of measurements needed to fully reconstruct a quantum state, we applied our measurements to the efficient tomographic reconstruction of the state produced by our down-conversion source. An analogous experimental configuration in which measurements in the same mutually unbiased bases were implemented was used to realize a proof-of-principle high-dimensional QKD system. A security assessment and experimental implementations for full mutually unbiased single-photon bases from $d = 2$ to 5 were presented.

The ability to generate and measure photons with complicated transverse structures therefore makes the spatial modes of a photon an appealing resource for quantum information processing and various quantum protocols. However, new loopholes previously not fully recognized accompany the use of state spaces embedded in a higher-dimensional space. A subtle form of fair-sampling loophole has to be accounted for when performing Bell-type tests using OAM. We outlined the importance of this consideration as device-independent quantum protocols become available and new attack strategies have to be considered in the context of QKD.

The techniques, theoretical treatments, experiments and results here pre-

sented can represent the groundwork for future experiments exploring bipartite high-dimensional entanglement and the foundations of quantum mechanics, as well as applications in quantum information and technology. We have shown how the OAM of light can be conveniently combined with its radial degree of freedom, and how both can be manipulated within the same experimental apparatus. Each stage of the experiments described throughout this thesis have the potential to be used in different systems where manipulation and detection of OAM are required, including prospective generalizations to multi-partite high-dimensional photonic states. The various theoretical and experimental aspects of OAM provide a valuable experimental resource and an ever surprising outlook on old and new fundamental problems in optics, electromagnetism and quantum mechanics. We hope that the work here presented will be a useful reference for others to learn more about the foundations of quantum mechanics, but also to take advantage of the quantum nature of light and bring about groundbreaking advances in information and communication technology.

APPENDIX A

Mutually unbiased vectors

For each vector v_{mi} , m indicates the basis among the $d+1$ available in dimension d and i the vector within the basis. Each vector provides the corresponding set of complex coefficients for the superposition of the basis modes of choice.

A.1 Coefficients for $d = 2$

m	i	c_1	c_2
1	1	1	0
	2	0	1
2	1	$1/\sqrt{2}$	$1/\sqrt{2}$
	2	$1/\sqrt{2}$	$-1/\sqrt{2}$
3	1	$1/\sqrt{2}$	$i/\sqrt{2}$
	2	$1/\sqrt{2}$	$-i/\sqrt{2}$

A.2 Coefficients for $d = 3$

m	i	c_1	c_2	c_3
-----	-----	-------	-------	-------

	1	1	0	0
1	2	0	1	0
	3	0	0	1
<hr/>				
	1	$1/\sqrt{3}$	$1/\sqrt{3}$	$1/\sqrt{3}$
2	2	$1/\sqrt{3}$	$e^{2i\pi/3}/\sqrt{3}$	$e^{-2i\pi/3}/\sqrt{3}$
	3	$1/\sqrt{3}$	$e^{-2i\pi/3}/\sqrt{3}$	$e^{2i\pi/3}/\sqrt{3}$
<hr/>				
	1	$1/\sqrt{3}$	$e^{2i\pi/3}/\sqrt{3}$	$e^{2i\pi/3}/\sqrt{3}$
3	2	$1/\sqrt{3}$	$e^{-2i\pi/3}/\sqrt{3}$	$1/\sqrt{3}$
	3	$1/\sqrt{3}$	$1/\sqrt{3}$	$e^{-2i\pi/3}/\sqrt{3}$
<hr/>				
	1	$1/\sqrt{3}$	$e^{-2i\pi/3}/\sqrt{3}$	$e^{-2i\pi/3}/\sqrt{3}$
4	2	$1/\sqrt{3}$	$1/\sqrt{3}$	$e^{2i\pi/3}/\sqrt{3}$
	3	$1/\sqrt{3}$	$e^{2i\pi/3}/\sqrt{3}$	$1/\sqrt{3}$
<hr/>				

A.3 Coefficients for $d = 4$

m	i	c_1	c_2	c_3	c_4
	1	1	0	0	0
1	2	0	1	0	0
	3	0	0	1	0
	4	0	0	0	1
<hr/>					
	1	$1/2$	$1/2$	$1/2$	$1/2$
2	2	$1/2$	$1/2$	$-1/2$	$-1/2$
	3	$1/2$	$-1/2$	$-1/2$	$1/2$
	4	$1/2$	$-1/2$	$1/2$	$-1/2$
<hr/>					
	1	$1/2$	$1/2$	$-i/2$	$i/2$
3	2	$1/2$	$1/2$	$i/2$	$-i/2$
	3	$1/2$	$-1/2$	$i/2$	$i/2$
	4	$1/2$	$-1/2$	$-i/2$	$-i/2$
<hr/>					
	1	$1/2$	$i/2$	$-1/2$	$i/2$

	2	1/2	-i/2	-1/2	-i/2
	3	1/2	i/2	1/2	-i/2
	4	1/2	-i/2	1/2	i/2
	1	1/2	i/2	i/2	-1/2
	2	1/2	-i/2	-i/2	-1/2
5	3	1/2	i/2	-i/2	1/2
	4	1/2	-i/2	i/2	1/2

A.4 Coefficients for $d = 5$

m	i	c_1	c_2	c_3	c_4	c_5
	1	1	0	0	0	0
	2	0	1	0	0	0
1	3	0	0	1	0	0
	4	0	0	0	1	0
	5	0	0	0	0	1
	1	$1/\sqrt{5}$	$1/\sqrt{5}$	$1/\sqrt{5}$	$1/\sqrt{5}$	$1/\sqrt{5}$
	2	$1/\sqrt{5}$	$e^{2i\pi/5}/\sqrt{5}$	$e^{4i\pi/5}/\sqrt{5}$	$e^{-4i\pi/5}/\sqrt{5}$	$e^{-2i\pi/5}/\sqrt{5}$
2	3	$1/\sqrt{5}$	$e^{4i\pi/5}/\sqrt{5}$	$e^{-2i\pi/5}/\sqrt{5}$	$e^{2i\pi/5}/\sqrt{5}$	$e^{-4i\pi/5}/\sqrt{5}$
	4	$1/\sqrt{5}$	$e^{-4i\pi/5}/\sqrt{5}$	$e^{2i\pi/5}/\sqrt{5}$	$e^{-2i\pi/5}/\sqrt{5}$	$e^{4i\pi/5}/\sqrt{5}$
	5	$1/\sqrt{5}$	$e^{-2i\pi/5}/\sqrt{5}$	$e^{-4i\pi/5}/\sqrt{5}$	$e^{4i\pi/5}/\sqrt{5}$	$e^{2i\pi/5}/\sqrt{5}$
	1	$1/\sqrt{5}$	$e^{2i\pi/5}/\sqrt{5}$	$e^{-2i\pi/5}/\sqrt{5}$	$e^{-2i\pi/5}/\sqrt{5}$	$e^{2i\pi/5}/\sqrt{5}$
	2	$1/\sqrt{5}$	$e^{4i\pi/5}/\sqrt{5}$	$e^{2i\pi/5}/\sqrt{5}$	$e^{4i\pi/5}/\sqrt{5}$	$1/\sqrt{5}$
3	3	$1/\sqrt{5}$	$e^{-4i\pi/5}/\sqrt{5}$	$e^{-4i\pi/5}/\sqrt{5}$	$1/\sqrt{5}$	$e^{-2i\pi/5}/\sqrt{5}$
	4	$1/\sqrt{5}$	$e^{-2i\pi/5}/\sqrt{5}$	$1/\sqrt{5}$	$e^{-4i\pi/5}/\sqrt{5}$	$e^{-4i\pi/5}/\sqrt{5}$
	5	$1/\sqrt{5}$	$1/\sqrt{5}$	$e^{4i\pi/5}/\sqrt{5}$	$e^{2i\pi/5}/\sqrt{5}$	$e^{4i\pi/5}/\sqrt{5}$
	1	$1/\sqrt{5}$	$e^{4i\pi/5}/\sqrt{5}$	$e^{-4i\pi/5}/\sqrt{5}$	$e^{-4i\pi/5}/\sqrt{5}$	$e^{4i\pi/5}/\sqrt{5}$
	2	$1/\sqrt{5}$	$e^{-4i\pi/5}/\sqrt{5}$	$1/\sqrt{5}$	$e^{2i\pi/5}/\sqrt{5}$	$e^{2i\pi/5}/\sqrt{5}$
	3	$1/\sqrt{5}$	$e^{-2i\pi/5}/\sqrt{5}$	$e^{4i\pi/5}/\sqrt{5}$	$e^{-2i\pi/5}/\sqrt{5}$	$1/\sqrt{5}$
4	4	$1/\sqrt{5}$	$1/\sqrt{5}$	$e^{-2i\pi/5}/\sqrt{5}$	$e^{4i\pi/5}/\sqrt{5}$	$e^{-2i\pi/5}/\sqrt{5}$

5	$1/\sqrt{5}$	$e^{2i\pi/5}/\sqrt{5}$	$e^{2i\pi/5}/\sqrt{5}$	$1/\sqrt{5}$	$e^{-4i\pi/5}/\sqrt{5}$
1	$1/\sqrt{5}$	$e^{-4i\pi/5}/\sqrt{5}$	$e^{4i\pi/5}/\sqrt{5}$	$e^{4i\pi/5}/\sqrt{5}$	$e^{-4i\pi/5}/\sqrt{5}$
2	$1/\sqrt{5}$	$e^{-2i\pi/5}/\sqrt{5}$	$e^{-2i\pi/5}/\sqrt{5}$	$1/\sqrt{5}$	$e^{4i\pi/5}/\sqrt{5}$
5	3	$1/\sqrt{5}$	$1/\sqrt{5}$	$e^{2i\pi/5}/\sqrt{5}$	$e^{-4i\pi/5}/\sqrt{5}$
4	$1/\sqrt{5}$	$e^{2i\pi/5}/\sqrt{5}$	$e^{-4i\pi/5}/\sqrt{5}$	$e^{2i\pi/5}/\sqrt{5}$	$1/\sqrt{5}$
5	$1/\sqrt{5}$	$e^{4i\pi/5}/\sqrt{5}$	$1/\sqrt{5}$	$e^{-2i\pi/5}/\sqrt{5}$	$e^{-2i\pi/5}/\sqrt{5}$
1	$1/\sqrt{5}$	$e^{-2i\pi/5}/\sqrt{5}$	$e^{2i\pi/5}/\sqrt{5}$	$e^{2i\pi/5}/\sqrt{5}$	$e^{-2i\pi/5}/\sqrt{5}$
2	$1/\sqrt{5}$	$1/\sqrt{5}$	$e^{-4i\pi/5}/\sqrt{5}$	$e^{-2i\pi/5}/\sqrt{5}$	$e^{-4i\pi/5}/\sqrt{5}$
6	3	$1/\sqrt{5}$	$e^{2i\pi/5}/\sqrt{5}$	$1/\sqrt{5}$	$e^{4i\pi/5}/\sqrt{5}$
4	$1/\sqrt{5}$	$e^{4i\pi/5}/\sqrt{5}$	$e^{4i\pi/5}/\sqrt{5}$	$1/\sqrt{5}$	$e^{2i\pi/5}/\sqrt{5}$
5	$1/\sqrt{5}$	$e^{-4i\pi/5}/\sqrt{5}$	$e^{-2i\pi/5}/\sqrt{5}$	$e^{-4i\pi/5}/\sqrt{5}$	$1/\sqrt{5}$

APPENDIX B

List of abbreviations

- BBO** β -barium borate
- BS** beam splitter
- CGH** computer-generated hologram
- CHSH** Clauser-Horne-Shimony-Holt (inequality)
- EPR** Einstein-Podolsky-Rosen
- HG** Hermite-Gauss mode
- HOM** Hong-Ou-Mandel (interference)
- HWP** half-wave plate
- LG** Laguerre-Gauss modes
- LHV** local hidden variable (theories)
- MMF** multi-mode optical fibre
- MUB** mutually unbiased bases
- OAM** orbital angular momentum
- PBS** polarizing beam splitter

QST quantum state tomography

QWP quarter-wave plate

SMF single-mode optical fibre

SPDC spontaneous parametric down-conversion

TEM transverse electromagnetic mode

UV ultraviolet

WP wave plate

Bibliography

- [1] M. Abramowitz and I. Stegun, *Handbook of Mathematical Functions* (Dover, 1965).
- [2] A. Acín, N. Brunner, N. Gisin, S. Massar, S. Pironio and V. Scarani, “Device-Independent Security of Quantum Cryptography against Collective Attacks”, *Phys. Rev. Lett.* 98, 230501 (2007).
- [3] R. B. A. Adamson and A. M. Steinberg, “Improving Quantum State Estimation with Mutually Unbiased Bases”, *Phys. Rev. Lett.* 105, 030406 (2010).
- [4] M. Agnew, J. Leach, M. McLaren, F. S. Roux and R. W. Boyd, “Tomography of the quantum state of photons entangled in high dimensions”, *Phys. Rev. A* 84, 062101 (2011).
- [5] Y. Aharonov, P. G. Bergmann and J. L. Lebowitz, “Time Symmetry in the Quantum Process of Measurement”, *Phys. Rev.* 134(6B), B1410 (1964).
- [6] Y. Aharonov and L. Vaidman, “Complete description of a quantum system at a given time”, *J. Phys. A* 24(10), 2315 (1991).
- [7] I. Ali-Khan, C. J. Broadbent and J. C. Howell, “Large-Alphabet Quantum Key Distribution Using Energy-Time Entangled Bipartite States”, *Phys. Rev. Lett.* 98, 060503 (2007).
- [8] L. Allen, S. Barnett and M. Padgett, *Optical Angular Momentum* (Taylor & Francis, 2003).
- [9] L. Allen, M. W. Beijersbergen, R. J. C. Spreeuw and J. P. Woerdman, “Orbital angular momentum of light and the transformation of Laguerre-Gaussian laser modes”, *Phys. Rev. A* 45, 8185 (1992).
- [10] L. Allen, J. Courtial and M. J. Padgett, “Matrix formulation for the propagation of light beams with orbital and spin angular momenta”, *Phys. Rev. E* 60(6), 7497 (1999).
- [11] J. B. Altepeter, E. R. Jeffrey and P. G. Kwiat, “Photonic State Tomography”, in “Advances in Atomic, Molecular, and Optical Physics”, (Elsevier, 2005).

- [12] D. Andrews and M. Babiker (editors), *The Angular Momentum of Light* (Cambridge University Press, 2012).
- [13] J. Arlt and K. Dholakia, “Generation of high-order Bessel beams by use of an axicon”, *Opt. Commun.* 177(1–6), 297 (2000).
- [14] J. Arlt, K. Dholakia, L. Allen and M. J. Padgett, “The production of multiringed Laguerre-Gaussian modes by computer-generated holograms”, *J. Mod. Opt.* 45, 1231 (1998).
- [15] V. Arrizón, U. Ruiz, R. Carrada and L. A. González, “Pixelated phase computer holograms for the accurate encoding of scalar complex fields”, *J. Opt. Soc. Am. A* 24(11), 3500 (2007).
- [16] A. Aspect, J. Dalibard and G. Roger, “Experimental Test of Bell’s Inequalities Using Time-Varying Analyzers”, *Phys. Rev. Lett.* 49, 1804 (1982).
- [17] A. Aspect, P. Grangier and G. Roger, “Experimental Tests of Realistic Local Theories via Bell’s Theorem”, *Phys. Rev. Lett.* 47, 460 (1981).
- [18] A. Aspect, P. Grangier and G. Roger, “Experimental Realization of Einstein-Podolsky-Rosen-Bohm *Gedankenexperiment*: A New Violation of Bell’s Inequalities”, *Phys. Rev. Lett.* 49, 91 (1982).
- [19] M. Avenhaus, M. V. Chekhova, L. A. Krivitsky, G. Leuchs and C. Silberhorn, “Experimental verification of high spectral entanglement for pulsed waveguided spontaneous parametric down-conversion”, *Phys. Rev. A* 79, 043836 (2009).
- [20] K. Banaszek, G. M. D’Ariano, M. G. A. Paris and M. F. Sacchi, “Maximum-likelihood estimation of the density matrix”, *Phys. Rev. A* 61, 010304 (1999).
- [21] M. A. Bandres and J. C. Gutiérrez-Vega, “Ince-Gaussian beams”, *Opt. Lett.* 29(2), 144 (2004).
- [22] S. Bandyopadhyay, P. O. Boykin, V. Roychowdhury and F. Vatan, “A New Proof for the Existence of Mutually Unbiased Bases”, *Algorithmica* 34, 512 (2002).
- [23] S. M. Barnett, *Quantum Information* (Oxford University Press, 2009).
- [24] S. M. Barnett and D. T. Pegg, “Quantum theory of optical phase correlations”, *Phys. Rev. A* 42(11), 6713 (1990).
- [25] S. M. Barnett and D. T. Pegg, “Quantum theory of rotation angles”, *Phys. Rev. A* 41, 3427 (1990).
- [26] S. M. Barnett, D. T. Pegg and J. Jeffers, “Bayes’ theorem and quantum retrodiction”, *J. Mod. Opt.* 47(11), 1779 (2000).

- [27] J. T. Barreiro, N. K. Langford, N. A. Peters and P. G. Kwiat, “Generation of Hyper-entangled Photon Pairs”, *Phys. Rev. Lett.* 95(26), 260501 (2005).
- [28] J. T. Barreiro, T.-C. Wei and P. G. Kwiat, “Beating the channel capacity limit for linear photonic superdense coding”, *Nat. Phys.* 4(4), 282 (2008).
- [29] V. Y. Bazhenov, M. V. Vasnetsov and M. S. Soskin, “Laser beams with screw dislocations in their wavefronts”, *JETP Lett.* 52(8), 429 (1990).
- [30] H. Bechmann-Pasquinucci and A. Peres, “Quantum Cryptography with 3-State Systems”, *Phys. Rev. Lett.* 85, 3313 (2000).
- [31] H. Bechmann-Pasquinucci and W. Tittel, “Quantum cryptography using larger alphabets”, *Phys. Rev. A* 61, 062308 (2000).
- [32] M. W. Beijersbergen, L. Allen, H. E. L. O. van der Veen and J. P. Woerdman, “Astigmatic laser mode converters and transfer of orbital angular momentum”, *Opt. Commun.* 96(1-3), 123 (1993).
- [33] J. S. Bell, “On the Einstein-Podolski-Rosen Paradox”, *Physics* 1(3), 195 (1964).
- [34] J. S. Bell, “On the Problem of Hidden Variables in Quantum Mechanics”, *Rev. Mod. Phys.* 38, 447 (1966).
- [35] J. S. Bell, *Speakable and unspeakable in quantum mechanics* (Cambridge University Press, 1987).
- [36] C. H. Bennett, “Quantum cryptography using any two nonorthogonal states”, *Phys. Rev. Lett.* 68, 3121 (1992).
- [37] C. H. Bennett and G. Brassard, “Quantum cryptography: Public key distribution and coin tossing”, in “Proceedings of the IEEE International Conference on Computers, Systems, and Signal Processing, Bangalore”, 175 (1984).
- [38] C. H. Bennett, G. Brassard, C. Crépeau, R. Jozsa, A. Peres and W. K. Wootters, “Teleporting an unknown quantum state via dual classical and Einstein-Podolsky-Rosen channels”, *Phys. Rev. Lett.* 70, 1895 (1993).
- [39] C. H. Bennett, G. Brassard and N. D. Mermin, “Quantum cryptography without Bell’s theorem”, *Phys. Rev. Lett.* 68, 557 (1992).
- [40] C. H. Bennett, G. Brassard, S. Popescu, B. Schumacher, J. A. Smolin and W. K. Wootters, “Purification of Noisy Entanglement and Faithful Teleportation via Noisy Channels”, *Phys. Rev. Lett.* 76(5), 722 (1996).
- [41] C. H. Bennett and S. J. Wiesner, “Communication via one- and two-particle operators on Einstein-Podolsky-Rosen states”, *Phys. Rev. Lett.* 69, 2881 (1992).

- [42] R. S. Bennink, “Optimal collinear Gaussian beams for spontaneous parametric down-conversion”, *Phys. Rev. A* 81, 053805 (2010).
- [43] G. C. G. Berkhout, M. P. J. Lavery, J. Courtial, M. W. Beijersbergen and M. J. Padgett, “Efficient Sorting of Orbital Angular Momentum States of Light”, *Phys. Rev. Lett.* 105(15), 153601 (2010).
- [44] D. W. Berry, H. Jeong, M. Stobińska and T. C. Ralph, “Fair-sampling assumption is not necessary for testing local realism”, *Phys. Rev. A* 81, 012109 (2010).
- [45] R. A. Beth, “Mechanical Detection and Measurement of the Angular Momentum of Light”, *Phys. Rev.* 50, 115 (1936).
- [46] D. Bohm, *Quantum Theory*, Dover Books on Physics Series (Dover Publications, 1951).
- [47] D. Bohm and Y. Aharonov, “Discussion of Experimental Proof for the Paradox of Einstein, Rosen, and Podolsky”, *Phys. Rev.* 108, 1070 (1957).
- [48] N. Bohr, “The Quantum Postulate and the Recent Development of Atomic Theory”, *Nature* 121, 580 (1928).
- [49] N. Bohr, “Can Quantum-Mechanical Description of Physical Reality be Considered Complete?” *Phys. Rev.* 48, 696 (1935).
- [50] N. Bohr, “Niels Bohr, Collected Works”, in L. Rosenfeld and J. R. Nielsen (editors), “The Correspondence Principle (1918–1923)”, (North-Holland, 1976).
- [51] E. Bolduc, N. Bent, E. Santamato, E. Karimi and R. W. Boyd, “Exact solution to simultaneous intensity and phase encryption with a single phase-only hologram”, *Opt. Lett.* 38(18), 3546 (2013).
- [52] M. Bourennane, A. Karlsson, G. Björk, N. Gisin and N. J. Cerf, “Quantum key distribution using multilevel encoding: security analysis”, *J. Phys. A* 35(47), 10065 (2002).
- [53] D. Bouwmeester, A. Ekert and A. Zeilinger (editors), *The Physics of Quantum Information: Quantum Cryptography, Quantum Teleportation, Quantum Computation* (Springer, 2000).
- [54] R. W. Boyd, *Nonlinear Optics* (Academic Press, 2008), 3rd ed.
- [55] D. Branning, W. P. Grice, R. Erdmann and I. A. Walmsley, “Engineering the Indistinguishability and Entanglement of Two Photons”, *Phys. Rev. Lett.* 83, 955 (1999).
- [56] G. Brassard, H. Buhrman, N. Linden, A. A. Méthot, A. Tapp and E. Unger “Limit on Nonlocality in Any World in Which Communication Complexity Is Not Trivial”, *Phys. Rev. Lett.* 96, 250401 (2006).

- [57] I. Bregman, D. Aharonov, M. Ben-Or and H. S. Eisenberg, “Simple and secure quantum key distribution with biphotons”, *Phys. Rev. A* 77, 050301 (2008).
- [58] S. Brierley and S. Weigert, “Constructing mutually unbiased bases in dimension six”, *Phys. Rev. A* 79(5), 052316 (2009).
- [59] S. Brierley and S. Weigert, “Mutually unbiased bases and semi-definite programming”, *J. Phys. Conf. Ser.* 254(1), 012008 (2010).
- [60] S. Brierley, S. Weigert and I. Bengtsson, “All mutually unbiased bases in dimensions two to five”, *Quantum Inf. Comput.* 10, 0803 (2010).
- [61] T. Brougham and S. M. Barnett, “Information communicated by entangled photon pairs”, *Phys. Rev. A* 85, 032322 (2012).
- [62] N. Brunner, S. Pironio, A. Acin, N. Gisin, A. A. Méthot and V. Scarani, “Testing the Dimension of Hilbert Spaces”, *Phys. Rev. Lett.* 100, 210503 (2008).
- [63] D. Bruß, “Optimal Eavesdropping in Quantum Cryptography with Six States”, *Phys. Rev. Lett.* 81, 3018 (1998).
- [64] D. C. Burnham and D. L. Weinberg, “Observation of Simultaneity in Parametric Production of Optical Photon Pairs”, *Phys. Rev. Lett.* 25, 84 (1970).
- [65] F. Buscemi, “All Entangled Quantum States Are Nonlocal”, *Phys. Rev. Lett.* 108, 200401 (2012).
- [66] D. P. Caetano, M. P. Almeida, P. H. Souto Ribeiro, J. A. O. Huguenin, B. Coutinho dos Santos and A. Z. Khoury, “Conservation of orbital angular momentum in stimulated down-conversion”, *Phys. Rev. A* 66, 041801 (2002).
- [67] A. R. Calderbank, E. M. Rains, P. W. Shor and N. J. A. Sloane, “Quantum Error Correction and Orthogonal Geometry”, *Phys. Rev. Lett.* 78, 405 (1997).
- [68] N. J. Cerf, M. Bourennane, A. Karlsson and N. Gisin, “Security of Quantum Key Distribution Using d -Level Systems”, *Phys. Rev. Lett.* 88, 127902 (2002).
- [69] A. Chefles and S. M. Barnett, “Complementarity and Cirel’son’s inequality”, *J. Phys. A* 29(10), L237 (1996).
- [70] Y.-A. Chen, T. Yang, A.-N. Zhang, Z. Zhao, A. Cabello and J.-W. Pan, “Experimental Violation of Bell’s Inequality beyond Tsirelson’s Bound”, *Phys. Rev. Lett.* 97, 170408 (2006).
- [71] B. Cirel’son, “Quantum generalizations of Bell’s inequality”, *Lett. Math. Phys.* 4(2), 93 (1980).
- [72] M. A. Cirone, “Entanglement correlations, Bell inequalities and the concurrence”, *Physics Letters A* 339(3–5), 269 (2005).

- [73] J. F. Clauser, “Early History of Bell’s Theorem”, in “Quantum [Un]speakables”, 61–98 (Springer Berlin Heidelberg, 2002).
- [74] J. F. Clauser and J. P. Dowling, “Factoring integers with Young’s N -slit interferometer”, *Phys. Rev. A* 53, 4587 (1996).
- [75] J. F. Clauser and M. A. Horne, “Experimental consequences of objective local theories”, *Phys. Rev. D* 10, 526 (1974).
- [76] J. F. Clauser, M. A. Horne, A. Shimony and R. A. Holt, “Proposed Experiment to Test Local Hidden-Variable Theories”, *Phys. Rev. Lett.* 23, 880 (1969).
- [77] J. F. Clauser and A. Shimony, “Bell’s theorem. Experimental tests and implications”, *Rep. Prog. Phys.* 41(12), 1881 (1978).
- [78] M. Clifford, J. Arlt, J. Courtial and K. Dholakia, “High-order Laguerre–Gaussian laser modes for studies of cold atoms”, *Opt. Commun.* 156(4–6), 300 (1998).
- [79] D. Collins, N. Gisin, N. Linden, S. Massar and S. Popescu, “Bell Inequalities for Arbitrarily High-Dimensional Systems”, *Phys. Rev. Lett.* 88, 040404 (2002).
- [80] J. H. Crichton and P. L. Marston, “The measurable distinction between the spin and orbital angular momenta of electromagnetic radiation”, *Elec. Journ. Diff. Eq. Conf.* 4, 37 (2000).
- [81] A. C. Dada, J. Leach, G. S. Buller, M. J. Padgett and E. Andersson, “Experimental high-dimensional two-photon entanglement and violations of generalized Bell inequalities”, *Nat. Phys.* 7(9), 677 (2011).
- [82] V. D’Ambrosio, F. Cardano, E. Karimi, E. Nagali, E. Santamato, L. Marrucci and F. Sciarrino, “Test of mutually unbiased bases for six-dimensional photonic quantum systems”, *Sci. Rep.* 3 (2013).
- [83] J. A. Davis, D. M. Cottrell, J. Campos, M. J. Yzuel and I. Moreno, “Encoding Amplitude Information onto Phase-Only Filters”, *Appl. Opt.* 38(23), 5004 (1999).
- [84] H. De Riedmatten, I. Marcikic, H. Zbinden and N. Gisin, “Creating high-dimensional time-bin entanglement using mode-locked lasers”, *Quant. Inf. Comp.* 2, 425 (2002).
- [85] V. Delaubert, D. A. Shaddock, P. K. Lam, B. C. Buchler, H.-A. Bachor and D. E. McClelland, “Generation of a phase-flipped Gaussian mode for optical measurements”, *J. Opt. A-Pure Appl. Op.* 4(4), 393 (2002).
- [86] H. Di Lorenzo Pires, F. M. G. J. Coppens and M. P. van Exter, “Type-I spontaneous parametric down-conversion with a strongly focused pump”, *Phys. Rev. A* 83(3), 033837 (2011).

- [87] H. Di Lorenzo Pires, H. C. B. Florijn and M. P. van Exter, “Measurement of the Spiral Spectrum of Entangled Two-Photon States”, *Phys. Rev. Lett.* 104(2), 020505 (2010).
- [88] H. Di Lorenzo Pires and M. P. van Exter, “Near-field correlations in the two-photon field”, *Phys. Rev. A* 80(5), 053820 (2009).
- [89] A. R. Dixon, Z. L. Yuan, J. F. Dynes, A. W. Sharpe and A. J. Shields, “Gigahertz decoy quantum key distribution with 1 Mbit/s secure key rate”, *Opt. Express* 16(23), 18790 (2008).
- [90] P. B. Dixon, G. A. Howland, J. Schneeloch and J. C. Howell, “Quantum Mutual Information Capacity for High-Dimensional Entangled States”, *Phys. Rev. Lett.* 108, 143603 (2012).
- [91] B. C. dos Santos, A. Z. Khoury and J. A. O. Huguenin, “Transfer of orbital angular momentum in a multimode parametric oscillator”, *Opt. Lett.* 33(23), 2803 (2008).
- [92] T. Durt, “A new expression for mutually unbiased bases in prime power dimensions”, (2004), arXiv:quant-ph/0409090.
- [93] T. Durt, B.-G. Englert, I. Bengtsson and K. Życzkowski, “On mutually unbiased bases”, *International Journal of Quantum Information* 08(04), 535 (2010).
- [94] P. H. Eberhard, “Background level and counter efficiencies required for a loophole-free Einstein-Podolsky-Rosen experiment”, *Phys. Rev. A* 47, R747 (1993).
- [95] A. Einstein, B. Podolsky and N. Rosen, “Can Quantum-Mechanical Description of Physical Reality Be Considered Complete?” *Phys. Rev.* 47, 777 (1935).
- [96] A. Ekert and P. L. Knight, “Entangled quantum systems and the Schmidt decomposition”, *Am. J. Phys.* 63(5), 415 (1995).
- [97] A. K. Ekert, “Quantum cryptography based on Bell’s theorem”, *Phys. Rev. Lett.* 67, 661 (1991).
- [98] B.-G. Englert, “Fringe Visibility and Which-Way Information: An Inequality”, *Phys. Rev. Lett.* 77, 2154 (1996).
- [99] A. Ferenczi and N. Lütkenhaus, “Symmetries in quantum key distribution and the connection between optimal attacks and optimal cloning”, *Phys. Rev. A* 85, 052310 (2012).
- [100] A. Fernández-Pérez, A. B. Klimov and C. Saavedra, “Quantum process reconstruction based on mutually unbiased basis”, *Phys. Rev. A* 83, 052332 (2011).
- [101] S. N. Filippov and V. I. Man’ko, “Mutually unbiased bases: tomography of spin states and the star-product scheme”, *Phys. Scripta* T143, 014010 (2011).

- [102] S. Franke-Arnold, S. M. Barnett, M. J. Padgett and L. Allen, “Two-photon entanglement of orbital angular momentum states”, *Phys. Rev. A* 65(3), 033823 (2002).
- [103] S. Franke-Arnold, S. M. Barnett, E. Yao, J. Leach, J. Courtial and M. Padgett, “Uncertainty principle for angular position and angular momentum”, *New J. Phys.* 6(1), 103 (2004).
- [104] J. Franson and T. Pittman, “An Optical Approach to Quantum Computing”, in C. Williams (editor), “Quantum Computing and Quantum Communications”, vol. 1509 of *Lecture Notes in Computer Science*, 383–390 (Springer Berlin Heidelberg, 1999).
- [105] S. J. Freedman and J. F. Clauser, “Experimental Test of Local Hidden-Variable Theories”, *Phys. Rev. Lett.* 28, 938 (1972).
- [106] A. Garg and N. D. Mermin, “Detector inefficiencies in the Einstein-Podolsky-Rosen experiment”, *Phys. Rev. D* 35, 3831 (1987).
- [107] M. Genovese, “Research on hidden variable theories: A review of recent progresses”, *Phys. Rep.* 413(6), 319 (2005).
- [108] I. Gerhardt, Q. Liu, A. Lamas-Linares, J. Skaar, V. Scarani, V. Makarov and C. Kurtsiefer, “Experimentally Faking the Violation of Bell’s Inequalities”, *Phys. Rev. Lett.* 107, 170404 (2011).
- [109] D. Giovannini, F. M. Miatto, J. Romero, S. M. Barnett, J. P. Woerdman and M. J. Padgett, “Determining the dimensionality of bipartite orbital-angular-momentum entanglement using multi-sector phase masks”, *New J. Phys.* 14(7), 073046 (2012).
- [110] D. Giovannini, E. Nagali, L. Marrucci and F. Sciarrino, “Resilience of orbital-angular-momentum photonic qubits and effects on hybrid entanglement”, *Phys. Rev. A* 83(4), 042338 (2011).
- [111] D. Giovannini, J. Romero, J. Leach, A. Dudley, A. Forbes and M. J. Padgett, “Characterization of High-Dimensional Entangled Systems via Mutually Unbiased Measurements”, *Phys. Rev. Lett.* 110(14), 143601 (2013).
- [112] D. Giovannini, J. Romero and M. J. Padgett, “Interference of probability amplitudes: a simple demonstration within the Hong–Ou–Mandel experiment”, *J. Opt.* 16(3), 032002 (2014).
- [113] N. Gisin, G. Ribordy, W. Tittel and H. Zbinden, “Quantum cryptography”, *Rev. Mod. Phys.* 74(1), 145 (2002).
- [114] M. Giustina, A. Mech, S. Ramelow, B. Wittmann, J. Kofler, J. Beyer, A. Lita, B. Calkins, T. Gerrits, S. W. Nam, R. Ursin and A. Zeilinger, “Bell violation using entangled photons without the fair-sampling assumption”, *Nature* 497(7448), 227 (2013).

- [115] R. M. Gomes, A. Salles, F. Toscano, P. H. Souto Ribeiro and S. P. Walborn, “Quantum entanglement beyond Gaussian criteria”, *Proc. Natl. Acad. Sci. USA* 106(51), 21517 (2009).
- [116] J. W. Goodman, *Introduction to Fourier Optics* (Roberts & Company, 2005).
- [117] J. B. Götte, K. O’Holleran, D. Preece, F. Flossmann, S. Franke-Arnold, S. M. Barnett and M. J. Padgett, “Light beams with fractional orbital angular momentum and their vortex structure”, *Opt. Express* 16(2), 993 (2008).
- [118] D. Gottesman, “Class of quantum error-correcting codes saturating the quantum Hamming bound”, *Phys. Rev. A* 54, 1862 (1996).
- [119] W. Gough, “The angular momentum of radiation”, *Eur. J. Phys.* 7(2), 81 (1986).
- [120] W. P. Grice, R. Erdmann, I. A. Walmsley and D. Branning, “Spectral distinguishability in ultrafast parametric down-conversion”, *Phys. Rev. A* 57, R2289 (1998).
- [121] S. Gröblacher, T. Jennewein, A. Vaziri, G. Weihs and A. Zeilinger, “Experimental quantum cryptography with qutrits”, *New J. Phys.* 8(5), 75 (2006).
- [122] D. Gross, Y.-K. Liu, S. T. Flammia, S. Becker and J. Eisert, “Quantum State Tomography via Compressed Sensing”, *Phys. Rev. Lett.* 105, 150401 (2010).
- [123] M. T. Gruneisen, J. P. Black, R. C. Dymale and K. E. Stoltenberg, “Projective quantum measurements on spatial modes of the photon with transmission volume holograms”, in “Proc. SPIE 8542, Electro-Optical Remote Sensing, Photonic Technologies, and Applications VI, 85421Q”, 85421Q–85421Q–14 (2012).
- [124] M. T. Gruneisen, W. A. Miller, R. C. Dymale and A. M. Sweiti, “Holographic generation of complex fields with spatial light modulators: application to quantum key distribution”, *Appl. Opt.* 47(4), A32 (2008).
- [125] N. Heckenberg, R. McDuff, C. Smith, H. Rubinsztein-Dunlop and M. Wegener, “Laser beams with phase singularities”, *Opt. Quant. Electron.* 24(9), S951 (1992).
- [126] S. Hill and W. K. Wootters, “Entanglement of a Pair of Quantum Bits”, *Phys. Rev. Lett.* 78(26), 5022 (1997).
- [127] C. K. Hong and L. Mandel, “Theory of parametric frequency down conversion of light”, *Phys. Rev. A* 31(4), 2409 (1985).
- [128] C. K. Hong, Z. Y. Ou and L. Mandel, “Measurement of subpicosecond time intervals between two photons by interference”, *Phys. Rev. Lett.* 59(18), 2044 (1987).
- [129] R. Horodecki and M. Horodecki, “Information-theoretic aspects of inseparability of mixed states”, *Phys. Rev. A* 54, 1838 (1996).

- [130] R. Horodecki, P. Horodecki, M. Horodecki and K. Horodecki, “Quantum entanglement”, *Rev. Mod. Phys.* 81, 865 (2009).
- [131] J. C. Howell, R. S. Bennink, S. J. Bentley and R. W. Boyd, “Realization of the Einstein-Podolsky-Rosen Paradox Using Momentum- and Position-Entangled Photons from Spontaneous Parametric Down Conversion”, *Phys. Rev. Lett.* 92(21), 210403 (2004).
- [132] J. Humblet, “Sur le moment d’impulsion d’une onde électromagnétique”, *Physica* 10(7), 585 (1943).
- [133] I. D. Ivanović, “Geometrical description of quantal state determination”, *J. Phys. A* 14, 3241 (1981).
- [134] B. Jack, *Quantum entanglement of the spatial modes of light*, Ph.D. thesis, University of Glasgow (2012).
- [135] B. Jack, P. Aursand, S. Franke-Arnold, D. G. Ireland, J. Leach, S. M. Barnett and M. J. Padgett, “Demonstration of the angular uncertainty principle for single photons”, *J. Opt.* 13(6), 064017 (2011).
- [136] B. Jack, A. M. Yao, J. Leach, J. Romero, S. Franke-Arnold, D. G. Ireland, S. M. Barnett and M. J. Padgett, “Entanglement of arbitrary superpositions of modes within two-dimensional orbital angular momentum state spaces”, *Phys. Rev. A* 81, 043844 (2010).
- [137] G. Jaeger, A. Shimony and L. Vaidman, “Two interferometric complementarities”, *Phys. Rev. A* 51, 54 (1995).
- [138] D. F. V. James, P. G. Kwiat, W. J. Munro and A. G. White, “Measurement of qubits”, *Phys. Rev. A* 64(5), 052312 (2001).
- [139] A. K. Jha, B. Jack, E. Yao, J. Leach, R. W. Boyd, G. S. Buller, S. M. Barnett, S. Franke-Arnold and M. J. Padgett, “Fourier relationship between the angle and angular momentum of entangled photons”, *Phys. Rev. A* 78(4), 043810 (2008).
- [140] A. K. Jha, J. Leach, B. Jack, S. Franke-Arnold, S. M. Barnett, R. W. Boyd and M. J. Padgett, “Angular Two-Photon Interference and Angular Two-Qubit States”, *Phys. Rev. Lett.* 104, 010501 (2010).
- [141] L. Jun-Lin and W. Chuan, “Six-State Quantum Key Distribution Using Photons with Orbital Angular Momentum”, *Chinese Phys. Lett.* 27(11), 110303 (2010).
- [142] E. Karimi, R. W. Boyd, P. de la Hoz, H. de Guise, J. Řeháček, Z. Hradil, A. Aiello, G. Leuchs and L. L. Sánchez-Soto, “Radial quantum number of Laguerre-Gauss modes”, *Phys. Rev. A* 89, 063813 (2014).

- [143] E. Karimi, D. Giovannini, E. Bolduc, N. Bent, F. M. Miatto, M. J. Padgett and R. W. Boyd, “Exploring the quantum nature of the radial degree of freedom of a photon via Hong-Ou-Mandel interference”, *Phys. Rev. A* 89, 013829 (2014).
- [144] E. Karimi and E. Santamato, “Radial coherent and intelligent states of paraxial wave equation”, *Opt. Lett.* 37(13), 2484 (2012).
- [145] E. Karimi, G. Zito, B. Piccirillo, L. Marrucci and E. Santamato, “Hypergeometric-Gaussian modes”, *Opt. Lett.* 32(21), 3053 (2007).
- [146] D. Kawase, Y. Miyamoto, M. Takeda, K. Sasaki and S. Takeuchi, “Observing Quantum Correlation of Photons in Laguerre-Gauss Modes Using the Gouy Phase”, *Phys. Rev. Lett.* 101, 050501 (2008).
- [147] I. Kimel and L. R. Elias, “Relations between Hermite and Laguerre Gaussian modes”, *IEEE J. Quantum Elect.* 29(9), 2562 (1993).
- [148] A. Klappenecker and M. Rötteler, “Constructions of Mutually Unbiased Bases”, in “Finite Fields and Applications”, vol. 2948/2004, 262–266 (Springer, 2004).
- [149] D. A. Kleinman, “Theory of Optical Parametric Noise”, *Phys. Rev.* 174, 1027 (1968).
- [150] D. N. Klyshko, “A simple method of preparing pure states of an optical field, of implementing the Einstein–Podolsky–Rosen experiment, and of demonstrating the complementarity principle”, *Sov. Phys. Uspekhi* 31(1), 74 (1988).
- [151] P. Kok, W. J. Munro, K. Nemoto, T. C. Ralph, J. P. Dowling and G. J. Milburn, “Linear optical quantum computing with photonic qubits”, *Rev. Mod. Phys.* 79, 135 (2007).
- [152] P. Kolenderski, W. Wasilewski and K. Banaszek, “Modeling and optimization of photon pair sources based on spontaneous parametric down-conversion”, *Phys. Rev. A* 80, 013811 (2009).
- [153] H. Kragh, “Photon: New light on an old name”, (2014), arXiv:1401.0293 [physics.hist-ph].
- [154] P. G. Kwiat, “Hyper-entangled states”, *J. Mod. Opt.* 44(11-12), 2173 (1997).
- [155] P. G. Kwiat, K. Mattle, H. Weinfurter, A. Zeilinger, A. V. Sergienko and Y. Shih, “New High-Intensity Source of Polarization-Entangled Photon Pairs”, *Phys. Rev. Lett.* 75(24), 4337 (1995).
- [156] P. G. Kwiat, A. M. Steinberg and R. Y. Chiao, “Observation of a “quantum eraser”: A revival of coherence in a two-photon interference experiment”, *Phys. Rev. A* 45, 7729 (1992).
- [157] N. K. Langford, R. B. Dalton, M. D. Harvey, J. L. O’Brien, G. J. Pryde, A. Gilchrist, S. D. Bartlett and A. G. White, “Measuring Entangled Qutrits and Their Use for Quantum Bit Commitment”, *Phys. Rev. Lett.* 93(5), 053601 (2004).

- [158] U. Larsen, “Superspace geometry: the exact uncertainty relationship between complementary aspects”, *J. Phys. A* 23(7), 1041 (1990).
- [159] C. K. Law and J. H. Eberly, “Analysis and Interpretation of High Transverse Entanglement in Optical Parametric Down Conversion”, *Phys. Rev. Lett.* 92(12), 127903 (2004).
- [160] C. K. Law, I. A. Walmsley and J. H. Eberly, “Continuous Frequency Entanglement: Effective Finite Hilbert Space and Entropy Control”, *Phys. Rev. Lett.* 84, 5304 (2000).
- [161] J. Leach, B. Jack, J. Romero, A. K. Jha, A. M. Yao, S. Franke-Arnold, D. G. Ireland, R. W. Boyd, S. M. Barnett and M. J. Padgett, “Quantum Correlations in Optical Angle-Orbital Angular Momentum Variables”, *Science* 329(5992), 662 (2010).
- [162] J. Leach, B. Jack, J. Romero, M. Ritsch-Marte, R. W. Boyd, A. K. Jha, S. M. Barnett, S. Franke-Arnold and M. J. Padgett, “Violation of a Bell inequality in two-dimensional orbital angular momentum state-spaces”, *Opt. Express* 17(10) (2009).
- [163] J. Leach, R. E. Warburton, D. G. Ireland, F. Izdebski, S. M. Barnett, A. M. Yao, G. S. Buller and M. J. Padgett, “Quantum correlations in position, momentum, and intermediate bases for a full optical field of view”, *Phys. Rev. A* 85, 013827 (2012).
- [164] G. N. Lewis, “The conservation of photons”, *Nature* 118(2981), 874 (1926).
- [165] C.-M. Li, K. Chen, A. Reingruber, Y.-N. Chen and J.-W. Pan, “Verifying Genuine High-Order Entanglement”, *Phys. Rev. Lett.* 105, 210504 (2010).
- [166] G. Lima, L. Neves, R. Guzmán, E. S. Gómez, W. A. T. Nogueira, A. Delgado, A. Vargas and C. Saavedra, “Experimental quantum tomography of photonic qudits via mutually unbiased basis”, *Opt. Express* 19(4), 3542 (2011).
- [167] C. Liu, J. F. Chen, S. Zhang, S. Zhou, Y.-H. Kim, M. M. T. Loy, G. K. L. Wong and S. Du, “Two-photon interferences with degenerate and nondegenerate paired photons”, *Phys. Rev. A* 85, 021803 (2012).
- [168] W.-T. Liu, T. Zhang, J.-Y. Liu, P.-X. Chen and J.-M. Yuan, “Experimental Quantum State Tomography via Compressed Sampling”, *Phys. Rev. Lett.* 108, 170403 (2012).
- [169] H.-K. Lo, H. Chau and M. Ardehali, “Efficient Quantum Key Distribution Scheme and a Proof of Its Unconditional Security”, *J. Cryptol.* 18(2), 133 (2005).
- [170] R. Loudon, *The Quantum Theory of Light* (Oxford University Press, 2000), 3rd ed.
- [171] M. Mafu, A. Dudley, S. Goyal, D. Giovannini, M. McLaren, M. J. Padgett, T. Konrad, F. Petruccione, N. Lütkenhaus and A. Forbes, “Higher-dimensional orbital-angular-momentum-based quantum key distribution with mutually unbiased bases”, *Phys. Rev. A* 88(3), 032305 (2013).

- [172] A. Mair, V. Alipasha, G. Weihs and A. Zeilinger, “Entanglement of the orbital angular momentum states of photons”, *Nature* 412, 313 (2001).
- [173] M. Malik, M. O’Sullivan, B. Rodenburg, M. Mirhosseini, J. Leach, M. P. J. Lavery, M. J. Padgett and R. W. Boyd, “Influence of atmospheric turbulence on optical communications using orbital angular momentum for encoding”, *Opt. Express* 20(12), 13195 (2012).
- [174] T. Markvart, “The thermodynamics of optical étendue”, *J. Opt. A* 10(1), 015008 (2008).
- [175] M. Martinelli, J. A. O. Huguenin, P. Nussenzeig and A. Z. Khoury, “Orbital angular momentum exchange in an optical parametric oscillator”, *Phys. Rev. A* 70, 013812 (2004).
- [176] F. Miatto, H. Lorenzo Pires, S. Barnett and M. Exter, “Spatial Schmidt modes generated in parametric down-conversion”, *Eur. Phys. J. D* 66(10), 1 (2012).
- [177] F. M. Miatto, T. Brougham and A. M. Yao, “Cartesian and polar Schmidt bases for down-converted photons”, (2011), arXiv:1111.6449v1 [quant-ph].
- [178] F. M. Miatto, D. Giovannini, J. Romero, S. Franke-Arnold, S. M. Barnett and M. J. Padgett, “Bounds and optimisation of orbital angular momentum bandwidths within parametric down-conversion systems”, *Eur. Phys. J. D* 66(7), 178 (2012).
- [179] F. M. Miatto, A. M. Yao and S. M. Barnett, “Full characterization of the quantum spiral bandwidth of entangled biphotons”, *Phys. Rev. A* 83(3), 033816 (2011).
- [180] G. Molina-Terriza, J. P. Torres and L. Torner, “Management of the Angular Momentum of Light: Preparation of Photons in Multidimensional Vector States of Angular Momentum”, *Phys. Rev. Lett.* 88, 013601 (2001).
- [181] C. H. Monken, P. H. S. Ribeiro and S. Pádua, “Transfer of angular spectrum and image formation in spontaneous parametric down-conversion”, *Phys. Rev. A* 57(4), 3123 (1998).
- [182] E. Nagali, D. Giovannini, L. Marrucci, S. Slussarenko, E. Santamato and F. Sciarrino, “Experimental Optimal Cloning of Four-Dimensional Quantum States of Photons”, *Phys. Rev. Lett.* 105(7), 073602 (2010).
- [183] E. Nagali, L. Sansoni, L. Marrucci, E. Santamato and F. Sciarrino, “Experimental generation and characterization of single-photon hybrid ququarts based on polarization and orbital angular momentum encoding”, *Phys. Rev. A* 81(5), 052317 (2010).
- [184] E. Nagali, L. Sansoni, F. Sciarrino, F. De Martini, L. Marrucci, B. Piccirillo, E. Karimi and E. Santamato, “Optimal quantum cloning of orbital angular momentum photon qubits via Hong-Ou-Mandel coalescence”, *Nat. Photonics* 3, 720 (2009).

- [185] L. Neves, G. Lima, J. G. Aguirre Gómez, C. H. Monken, C. Saavedra and S. Pádua, “Generation of Entangled States of Qudits using Twin Photons”, *Phys. Rev. Lett.* 94, 100501 (2005).
- [186] H. Nihira and C. R. Stroud, “Robust multipartite multilevel quantum protocols”, *Phys. Rev. A* 72, 022337 (2005).
- [187] W. A. T. Nogueira, S. P. Walborn, S. Pádua and C. H. Monken, “Generation of a Two-Photon Singlet Beam”, *Phys. Rev. Lett.* 92, 043602 (2004).
- [188] J. Nunn, L. J. Wright, C. Söller, L. Zhang, I. A. Walmsley and B. J. Smith, “Large-alphabet time-frequency entangled quantum key distribution by means of time-to-frequency conversion”, *Opt. Express* 21(13), 15959 (2013).
- [189] S. S. R. Oemrawsingh, A. Aiello, E. R. Eliel, G. Nienhuis and J. P. Woerdman, “Violation of local realism in a high-dimensional two-photon setup with non-integer spiral phase plates”, (2004), arXiv:quant-ph/0401148v5.
- [190] S. S. R. Oemrawsingh, J. A. de Jong, X. Ma, A. Aiello, E. R. Eliel, G. W. 't Hooft and J. P. Woerdman, “High-dimensional mode analyzers for spatial quantum entanglement”, *Phys. Rev. A* 73, 032339 (2006).
- [191] S. S. R. Oemrawsingh, X. Ma, D. Voigt, A. Aiello, E. R. Eliel, G. W. 't Hooft and J. P. Woerdman, “Experimental Demonstration of Fractional Orbital Angular Momentum Entanglement of Two Photons”, *Phys. Rev. Lett.* 95(24), 240501 (2005).
- [192] H. C. Ohanian, “What is spin?” *Am. J. Phys.* 54, 500 (1986).
- [193] L. Olislager, J. Cussey, A. T. Nguyen, P. Emplit, S. Massar, J.-M. Merolla and K. P. Huy, “Frequency-bin entangled photons”, *Phys. Rev. A* 82, 013804 (2010).
- [194] T. Opatrný, D.-G. Welsch and W. Vogel, “Least-squares inversion for density-matrix reconstruction”, *Phys. Rev. A* 56, 1788 (1997).
- [195] C. I. Osorio, G. Molina-Terriza, B. G. Font and J. P. Torres, “Azimuthal distinguishability of entangled photons generated in spontaneous parametric down-conversion”, *Opt. Express* 15(22), 14636 (2007).
- [196] C. I. Osorio, G. Molina-Terriza and J. P. Torres, “Correlations in orbital angular momentum of spatially entangled paired photons generated in parametric down-conversion”, *Phys. Rev. A* 77(1), 015810 (2008).
- [197] C. I. Osorio, G. Molina-Terriza and J. P. Torres, “Orbital angular momentum correlations of entangled paired photons”, *J. Opt. A-Pure Appl. Op.* 11(9), 094013 (2009).
- [198] M. N. O’Sullivan-Hale, I. Ali Khan, R. W. Boyd and J. C. Howell, “Pixel Entanglement: Experimental Realization of Optically Entangled $d = 3$ and $d = 6$ Qudits”, *Phys. Rev. Lett.* 94(22), 220501 (2005).

- [199] Z. Y. Ou, “Temporal distinguishability of an N-photon state and its characterization by quantum interference”, *Phys. Rev. A* 74, 063808 (2006).
- [200] Z. Y. J. Ou, *Multi-Photon Quantum Interference*, chap. 3 (Springer, 2007).
- [201] M. J. Padgett and L. Allen, “The Poynting vector in Laguerre-Gaussian laser modes”, *Opt. Commun.* 121(1-3), 36 (1995).
- [202] M. J. Padgett and J. Courtial, “Poincaré sphere equivalent for light beams containing orbital angular momentum”, *Opt. Lett.* 24(7), 430 (1999).
- [203] A. K. Pati, P. Parashar and P. Agrawal, “Probabilistic superdense coding”, *Phys. Rev. A* 72, 012329 (2005).
- [204] M. Pawłowski, T. Paterek, D. Kaszlikowski, V. Scarani, A. Winter and M. Żukowski, “Information causality as a physical principle”, *Nature* 461(7267), 1101 (2009).
- [205] P. M. Pearle, “Hidden-Variable Example Based upon Data Rejection”, *Phys. Rev. D* 2, 1418 (1970).
- [206] D. Pegg, J. Vaccaro and S. M. Barnett, “Quantum-optical Phase and Canonical Conjugation”, *J. Mod. Opt.* 37(11), 1703 (1990).
- [207] D. T. Pegg and S. M. Barnett, “Quantum optical phase”, *J. Mod. Opt.* 44(2), 225 (1997).
- [208] T. B. Pittman, D. V. Strekalov, D. N. Klyshko, M. H. Rubin, A. V. Sergienko and Y. H. Shih, “Two-photon geometric optics”, *Phys. Rev. A* 53(4), 2804 (1996).
- [209] T. B. Pittman, D. V. Strekalov, A. Migdall, M. H. Rubin, A. V. Sergienko and Y. H. Shih, “Can Two-Photon Interference be Considered the Interference of Two Photons?” *Phys. Rev. Lett.* 77(10), 1917 (1996).
- [210] M. Planck, “On the Law of Distribution of Energy in the Normal Spectrum”, *Ann. Phys.* 4, 553 (1901).
- [211] E. Pomarico, B. Sanguinetti, P. Sekatski, H. Zbinden and N. Gisin, “Experimental amplification of an entangled photon: what if the detection loophole is ignored?” *New J. Phys.* 13(6), 063031 (2011).
- [212] S. Popescu and D. Rohrlich, “Quantum nonlocality as an axiom”, *Found. Phys.* 24, 379 (1994).
- [213] B. J. Pors, *Entangling light in high dimensions*, Ph.D. thesis, Leiden University (2011).
- [214] B.-J. Pors, E. Miatto, G. W. 't Hooft, E. R. Eliel and J. P. Woerdman, “High-dimensional entanglement with orbital-angular-momentum states of light”, *J. Opt.* 13(6), 064008 (2011).

- [215] J. B. Pors, A. Aiello, S. S. R. Oemrawsingh, M. P. van Exter, E. R. Eliel and J. P. Woerdman, “Angular phase-plate analyzers for measuring the dimensionality of multimode fields”, *Phys. Rev. A* 77(3), 033845 (2008).
- [216] J. B. Pors, S. S. R. Oemrawsingh, A. Aiello, M. P. van Exter, E. R. Eliel, G. W. ’t Hooft and J. P. Woerdman, “Shannon Dimensionality of Quantum Channels and Its Application to Photon Entanglement”, *Phys. Rev. Lett.* 101(12), 120502 (2008).
- [217] J. H. Poynting, “On the Transfer of Energy in the Electromagnetic Field”, *Philos. T. R. Soc. Lond.* 175, 343 (1884).
- [218] J. H. Poynting, “The Wave Motion of a Revolving Shaft, and a Suggestion as to the Angular Momentum in a Beam of Circularly Polarised Light”, *P. R. Soc. Lond. A* 82(557), 560 (1909).
- [219] M. F. Pusey, J. Barrett and T. Rudolph, “On the reality of the quantum state”, *Nat. Phys.* 8(6), 475 (2012).
- [220] H. Qassim, F. M. Miatto, J. P. Torres, M. J. Padgett, E. Karimi and R. W. Boyd, “Limitations to the determination of a Laguerre-Gauss spectrum via projective, phase-flattening measurement”, *J. Opt. Soc. Am. B* 31(6), A20 (2014).
- [221] J. G. Rarity and P. R. Tapster, “Two-color photons and nonlocality in fourth-order interference”, *Phys. Rev. A* 41, 5139 (1990).
- [222] M. G. Raymer, S. J. van Enk, C. J. McKinstrie and H. J. McGuinness, “Interference of two photons of different color”, *Opt. Commun.* 283(5), 747 (2010).
- [223] A. Rényi, *Probability Theory* (North-Holland, 1970).
- [224] D. Richart, Y. Fischer and H. Weinfurter, “Experimental implementation of higher dimensional time–energy entanglement”, *Appl. Phys. B* 106(3), 543 (2012).
- [225] B. Rodenburg, M. P. J. Lavery, M. Malik, M. N. O’Sullivan, M. Mirhosseini, D. J. Robertson, M. Padgett and R. W. Boyd, “Influence of atmospheric turbulence on states of light carrying orbital angular momentum”, *Opt. Lett.* 37(17), 3735 (2012).
- [226] J. Romero, D. Giovannini, S. Franke-Arnold, S. M. Barnett and M. J. Padgett, “Increasing the dimension in high-dimensional two-photon orbital angular momentum entanglement”, *Phys. Rev. A* 86(1), 012334 (2012).
- [227] J. Romero, D. Giovannini, D. S. Tasca, S. M. Barnett and M. J. Padgett, “Tailored two-photon correlation and fair-sampling: a cautionary tale”, *New J. Phys.* 15(8), 083047 (2013).
- [228] J. Romero, J. Leach, B. Jack, S. M. Barnett, M. J. Padgett and S. Franke-Arnold, “Violation of Leggett inequalities in orbital angular momentum subspaces”, *New J. Phys.* 12(12), 123007 (2010).

- [229] J. Romero, J. Leach, B. Jack, M. R. Dennis, S. Franke-Arnold, S. M. Barnett and M. J. Padgett, “Entangled Optical Vortex Links”, *Phys. Rev. Lett.* 106(10), 100407 (2011).
- [230] M. J. Romero, *Orbital angular momentum entanglement*, Ph.D. thesis, University of Glasgow (2012).
- [231] A. Rossi, G. Vallone, A. Chiuri, F. De Martini and P. Mataloni, “Multipath Entanglement of Two Photons”, *Phys. Rev. Lett.* 102, 153902 (2009).
- [232] M. A. Rowe, D. Kielpinski, V. Meyer, C. A. Sackett, W. M. Itano, C. Monroe and D. J. Wineland, “Experimental violation of a Bell’s inequality with efficient detection”, *Nature* 409(6822), 791 (2001).
- [233] M. H. Rubin, D. N. Klyshko, Y. H. Shih and A. V. Sergienko, “Theory of two-photon entanglement in type-II optical parametric down-conversion”, *Phys. Rev. A* 50, 5122 (1994).
- [234] V. D. Salakhutdinov, E. R. Eliel and W. Löffler, “Full-Field Quantum Correlations of Spatially Entangled Photons”, *Phys. Rev. Lett.* 108, 173604 (2012).
- [235] B. E. A. Saleh and M. C. Teich, *Fundamentals of Photonics* (John Wiley & Sons, Inc., 2007), 2nd ed.
- [236] V. Scarani, “The device-independent outlook on quantum physics (lecture notes on Bell inequalities)”, (2013), arXiv:1303.3081 [quant-ph].
- [237] V. Scarani, A. Acín, G. Ribordy and N. Gisin, “Quantum Cryptography Protocols Robust against Photon Number Splitting Attacks for Weak Laser Pulse Implementations”, *Phys. Rev. Lett.* 92, 057901 (2004).
- [238] V. Scarani, H. Bechmann-Pasquinucci, N. J. Cerf, M. Dušek, N. Lütkenhaus and M. Peev, “The security of practical quantum key distribution”, *Rev. Mod. Phys.* 81, 1301 (2009).
- [239] A. Schreiber, K. N. Cassemiro, V. Potoček, A. Gábris, P. J. Mosley, E. Andersson, I. Jex and C. Silberhorn, “Photons Walking the Line: A Quantum Walk with Adjustable Coin Operations”, *Phys. Rev. Lett.* 104, 050502 (2010).
- [240] E. Schrödinger, “Discussion of Probability Relations between Separated Systems”, *P. Camb. Philos. Soc.* 31(4), 555 (1935).
- [241] J. Schwinger, “Unitary operator bases”, *Proc. Natl. Acad. Sci. USA* 46(4), 570 (1960).
- [242] L. Sheridan and V. Scarani, “Security proof for quantum key distribution using qudit systems”, *Phys. Rev. A* 82, 030301 (2010).
- [243] Y. H. Shih and C. O. Alley, “New Type of Einstein-Podolsky-Rosen-Bohm Experiment Using Pairs of Light Quanta Produced by Optical Parametric Down Conversion”, *Phys. Rev. Lett.* 61, 2921 (1988).

- [244] A. E. Siegman, *Lasers* (University Science Books, 1986).
- [245] C. Spengler, M. Huber, S. Brierley, T. Adaktylos and B. C. Hiesmayr, “Entanglement detection via mutually unbiased bases”, *Phys. Rev. A* 86, 022311 (2012).
- [246] D. V. Strekalov, A. V. Sergienko, D. N. Klyshko and Y. H. Shih, “Observation of Two-Photon “Ghost” Interference and Diffraction”, *Phys. Rev. Lett.* 74(18), 3600 (1995).
- [247] J. Summhammer, “Factoring and Fourier transformation with a Mach-Zehnder interferometer”, *Phys. Rev. A* 56, 4324 (1997).
- [248] E.-K. Tan, J. Jeffers, S. M. Barnett and D. T. Pegg, “Retrodictive states and two-photon quantum imaging”, *Eur. Phys. J. D* 22(3), 495 (2003).
- [249] D. S. Tasca, S. P. Walborn, F. Toscano and P. H. Souto Ribeiro, “Observation of tunable Popescu-Rohrlich correlations through postselection of a Gaussian state”, *Phys. Rev. A* 80, 030101 (2009).
- [250] R. T. Thew, A. Acín, H. Zbinden and N. Gisin, “Bell-Type Test of Energy-Time Entangled Qutrits”, *Phys. Rev. Lett.* 93, 010503 (2004).
- [251] R. T. Thew, K. Nemoto, A. G. White and W. J. Munro, “Qudit quantum-state tomography”, *Phys. Rev. A* 66(1), 012303 (2002).
- [252] W. Tittel, J. Brendel, H. Zbinden and N. Gisin, “Violation of Bell Inequalities by Photons More Than 10 km Apart”, *Phys. Rev. Lett.* 81, 3563 (1998).
- [253] W. Tittel, J. Brendel, H. Zbinden and N. Gisin, “Quantum Cryptography Using Entangled Photons in Energy-Time Bell States”, *Phys. Rev. Lett.* 84, 4737 (2000).
- [254] J. P. Torres, A. Alexandrescu, S. Carrasco and L. Torner, “Quasi-phase-matching engineering for spatial control of entangled two-photon states”, *Opt. Lett.* 29(4), 376 (2004).
- [255] J. P. Torres, A. Alexandrescu and L. Torner, “Quantum spiral bandwidth of entangled two-photon states”, *Phys. Rev. A* 68(5), 050301 (2003).
- [256] J. P. Torres, Y. Deyanova, L. Torner and G. Molina-Terriza, “Preparation of engineered two-photon entangled states for multidimensional quantum information”, *Phys. Rev. A* 67, 052313 (2003).
- [257] J. P. Torres, G. Molina-Terriza and L. Torner, “The spatial shape of entangled photon states generated in non-collinear, walking parametric downconversion”, *J. Opt. B.* 7(9), 235 (2005).

- [258] R. Ursin, F. Tiefenbacher, T. Schmitt-Manderbach, H. Weier, T. Scheidl, M. Lindenthal, B. Blauensteiner, T. Jennewein, J. Perdigues, P. Trojek, B. Omer, M. Furst, M. Meyenburg, J. Rarity, Z. Sodnik, C. Barbieri, H. Weinfurter and A. Zeilinger, “Entanglement-based quantum communication over 144 km”, *Nat Phys* 3(7), 481 (2007).
- [259] G. Vallone, R. Ceccarelli, F. De Martini and P. Mataloni, “Hyperentanglement of two photons in three degrees of freedom”, *Phys. Rev. A* 79, 030301 (2009).
- [260] S. J. van Enk, “Geometric phase, transformations of gaussian light beams and angular momentum transfer”, *Opt. Commun.* 102(1-2), 59 (1993).
- [261] S. J. van Enk and G. Nienhuis, “Eigenfunction description of laser beams and orbital angular momentum of light”, *Opt. Commun.* 94(1-3), 147 (1992).
- [262] M. P. van Exter, A. Aiello, S. S. R. Oemrawsingh, G. Nienhuis and J. P. Woerdman, “Effect of spatial filtering on the Schmidt decomposition of entangled photons”, *Phys. Rev. A* 74, 012309 (2006).
- [263] H. Vanherzeele and C. Chen, “Widely tunable parametric generation in beta barium borate”, *Appl. Opt.* 27(13), 2634 (1988).
- [264] A. Vaziri, J.-W. Pan, T. Jennewein, G. Weihs and A. Zeilinger, “Concentration of Higher Dimensional Entanglement: Qutrits of Photon Orbital Angular Momentum”, *Phys. Rev. Lett.* 91(22), 227902 (2003).
- [265] A. Vaziri, G. Weihs and A. Zeilinger, “Experimental Two-Photon, Three-Dimensional Entanglement for Quantum Communication”, *Phys. Rev. Lett.* 89(24), 240401 (2002).
- [266] T. Vértesi, S. Pironio and N. Brunner, “Closing the Detection Loophole in Bell Experiments Using Qudits”, *Phys. Rev. Lett.* 104(6), 060401 (2010).
- [267] S. P. Walborn, A. N. de Oliveira, S. Pádua and C. H. Monken, “Multimode Hong-Ou-Mandel Interference”, *Phys. Rev. Lett.* 90(14), 143601 (2003).
- [268] S. P. Walborn, A. N. de Oliveira, R. S. Thebaldi and C. H. Monken, “Entanglement and conservation of orbital angular momentum in spontaneous parametric down-conversion”, *Phys. Rev. A* 69(2), 023811 (2004).
- [269] S. P. Walborn, D. S. Lemelle, M. P. Almeida and P. H. S. Ribeiro, “Quantum Key Distribution with Higher-Order Alphabets Using Spatially Encoded Qudits”, *Phys. Rev. Lett.* 96, 090501 (2006).
- [270] P. Walther, K. J. Resch, T. Rudolph, E. Schenck, H. Weinfurter, V. Vedral, M. Aspelmeyer and A. Zeilinger, “Experimental one-way quantum computing”, *Nature* 434(169-176) (2005).

- [271] G. N. Watson, *A Treatise on the Theory of Bessel Functions*, Cambridge Mathematical Library (Cambridge University Press, 1995).
- [272] S. Wehner and A. Winter, “Entropic uncertainty relations—a survey”, *New J. Phys.* 12(2), 025009 (2010).
- [273] G. Weihs, T. Jennewein, C. Simon, H. Weinfurter and A. Zeilinger, “Violation of Bell’s Inequality under Strict Einstein Locality Conditions”, *Phys. Rev. Lett.* 81, 5039 (1998).
- [274] M. Wiesniak, T. Paterek and A. Zeilinger, “Entanglement in mutually unbiased bases”, (2011), arXiv:1102.2080v3 [quant-ph].
- [275] W. K. Wootters, “Entanglement of Formation of an Arbitrary State of Two Qubits”, *Phys. Rev. Lett.* 80(10), 2245 (1998).
- [276] W. K. Wootters, “Entanglement of formation and concurrence”, *Quant. Inf. Comp.* 27–44 (2001).
- [277] W. K. Wootters and B. D. Fields, “Optimal state-determination by mutually unbiased measurements”, *Ann. Phys.* 191(2), 363 (1989).
- [278] S. Wu, S. Yu and K. Mølmer, “Entropic uncertainty relation for mutually unbiased bases”, *Phys. Rev. A* 79, 022104 (2009).
- [279] A. M. Yao, “Angular momentum decomposition of entangled photons with an arbitrary pump”, *New J. Phys.* 13(5), 053048 (2011).
- [280] A. M. Yao and M. J. Padgett, “Orbital angular momentum: origins, behavior and applications”, *Adv. Opt. Photon.* 3(2), 161 (2011).
- [281] A. Yariv, *Quantum Electronics* (John Wiley & Sons, Inc., 1988), 3rd ed.
- [282] T. Yarnall, A. F. Abouraddy, B. E. A. Saleh and M. C. Teich, “Experimental Violation of Bell’s Inequality in Spatial-Parity Space”, *Phys. Rev. Lett.* 99, 170408 (2007).
- [283] S. Yokoyama, R. Ukai, S. C. Armstrong, C. Sornphiphatphong, T. Kaji, S. Suzuki, J.-i. Yoshikawa, H. Yonezawa, N. C. Menicucci and A. Furusawa, “Ultra-large-scale continuous-variable cluster states multiplexed in the time domain”, *Nat. Photonics* 7(12), 982 (2013).
- [284] I.-C. Yu, F.-L. Lin and C.-Y. Huang, “Quantum secret sharing with multilevel mutually (un)biased bases”, *Phys. Rev. A* 78, 012344 (2008).
- [285] L. Zhang, C. Silberhorn and I. A. Walmsley, “Secure Quantum Key Distribution using Continuous Variables of Single Photons”, *Phys. Rev. Lett.* 100, 110504 (2008).
- [286] M. Żukowski, A. Zeilinger, M. A. Horne and A. K. Ekert, ““Event-ready-detectors” Bell experiment via entanglement swapping”, *Phys. Rev. Lett.* 71, 4287 (1993).